



# Feedbacks between convection and climate: Analysis with global modeling and satellite observations

Swati Gehlot



## Hinweis

Die Berichte zur Erdsystemforschung werden vom Max-Planck-Institut für Meteorologie in Hamburg in unregelmäßiger Abfolge herausgegeben.

Sie enthalten wissenschaftliche und technische Beiträge, inklusive Dissertationen.

Die Beiträge geben nicht notwendigerweise die Auffassung des Instituts wieder.

Die "Berichte zur Erdsystemforschung" führen die vorherigen Reihen "Reports" und "Examensarbeiten" weiter.



## Notice

*The Reports on Earth System Science are published by the Max Planck Institute for Meteorology in Hamburg. They appear in irregular intervals.*

*They contain scientific and technical contributions, including Ph. D. theses.*

*The Reports do not necessarily reflect the opinion of the Institute.*

*The "Reports on Earth System Science" continue the former "Reports" and "Examensarbeiten" of the Max Planck Institute.*

## Anschrift / Address

Max-Planck-Institut für Meteorologie  
Bundesstrasse 53  
20146 Hamburg  
Deutschland

Tel.: +49-(0)40-4 11 73-0  
Fax: +49-(0)40-4 11 73-298  
Web: [www.mpimet.mpg.de](http://www.mpimet.mpg.de)

## Layout:

Bettina Diallo, PR & Grafik

Titelfotos:

vorne:

Christian Klepp - Jochem Marotzke - Christian Klepp

hinten:

Clotilde Dubois - Christian Klepp - Katsumasa Tanaka

Feedbacks between convection and climate:  
Analysis with global modeling and satellite  
observations

Swati Gehlot

aus Indore, Indien

Hamburg 2010

Swati Gehlot  
Max-Planck-Institut für Meteorologie  
Bundesstrasse 53  
20146 Hamburg  
Germany

Als Dissertation angenommen  
vom Department Geowissenschaften der Universität Hamburg

auf Grund der Gutachten von  
Prof. Dr. Martin Claußen  
und  
Dr. Johannes Quaas

Hamburg, den 13. Juli 2010  
Prof. Dr. Jürgen Oßenbrügge  
Leiter des Departments für Geowissenschaften

Feedbacks between convection and climate:  
Analysis with global modeling and satellite  
observations

---



Swati Gehlot

Hamburg 2010

Cover picture source

Anvil Cirrus Cloud (generated by deep-convection) as seen from the International Space Station (ISS). From *Remote Sensing Tutorial by Dr. Nicholas Short* - Section 14. Available on the website of National Aeronautics and Space Administration (NASA) <http://rst.gsfc.nasa.gov/>.

Image courtesy of the Image Science & Analysis Laboratory, NASA Johnson Space Center <http://eol.jsc.nasa.gov>. Unique picture number ISS016-E-27426, Expedition 16, 2008.

# Contents

<b>Acknowledgement</b>	<b>iii</b>
<b>Abstract</b>	<b>1</b>
<b>1 Introduction and motivation</b>	<b>3</b>
1.1 Clouds and their radiative effects . . . . .	4
1.2 Model uncertainties associated with cloud processes . . . . .	5
1.3 Convection and Convection-climate feedbacks . . . . .	5
1.4 Key objectives . . . . .	6
1.5 Thesis outline . . . . .	7
<b>2 Description of model and data</b>	<b>9</b>
2.1 Model description (ECHAM5 General Circulation Model) . . . . .	9
2.1.1 General characteristics . . . . .	9
2.1.2 Clouds in ECHAM5 . . . . .	10
2.1.3 Convection scheme in ECHAM5 . . . . .	11
2.1.4 Statistical cloud cover scheme . . . . .	16
2.2 ISCCP satellite data used in model evaluation . . . . .	17
2.3 ISCCP satellite simulator in ECHAM5 . . . . .	18
2.3.1 Basic ISCCP simulator . . . . .	20
2.3.2 Addition of sub-grid column generator in ISCCP simulator . . . . .	24
<b>3 Evaluation of global cloud properties in model using satellite data</b>	<b>27</b>
3.1 Experimental setup and description of sensitivity runs . . . . .	27
3.2 ISCCP simulator version sensitivity analysis . . . . .	28
3.3 Global distribution of ISCCP cloud types . . . . .	30
3.4 Comparison of global average histograms . . . . .	32
3.5 Cloud regimes and their climate change response . . . . .	34
3.5.1 Clustering technique for definition of cloud regimes . . . . .	34
3.5.2 Climate change response . . . . .	40
3.6 Summary and conclusions . . . . .	42
<b>4 Evaluation of the diurnal cycle of clouds in ECHAM5 model</b>	<b>47</b>
4.1 Diurnal cycle of convection . . . . .	47
4.2 Case studies: Diurnal cycle variations in test areas . . . . .	50

---

4.2.1	Case study-1: African region . . . . .	51
4.2.2	Case study-2: Amazon basin . . . . .	54
4.2.3	Case study-3: Indian subcontinent . . . . .	57
4.2.4	Case study-4: Indonesian convective region . . . . .	58
4.3	Summary and conclusions . . . . .	60
<b>5</b>	<b>Convection-climate Feedbacks</b>	<b>63</b>
5.1	Climate feedbacks due to convection . . . . .	63
5.1.1	Transition of convective clouds to cirrostratus and cirrus . . . . .	65
5.2	Comparison of global distribution of deep-convective, cirrostratus and cirrus clouds . . . . .	66
5.3	The Lagrangian forward trajectory method . . . . .	69
5.3.1	Cloud transitions seen in ISCCP cloud property histograms . . . . .	74
5.3.2	Variation of cirrus and cirrostratus clouds along forward trajectories . . . . .	79
5.3.3	Comparison of hourly variation of cloud transitions . . . . .	81
5.4	Detrainment and in-situ cirrus life-cycle analysis . . . . .	84
5.5	Cirrus clouds in a warmer climate . . . . .	85
5.5.1	Comparison of cloud transitions for present and perturbed climate . . . . .	87
5.6	Summary and conclusions . . . . .	93
<b>6</b>	<b>Conclusions</b>	<b>95</b>
6.1	Main findings of the research . . . . .	95
6.1.1	Comparison of global average cloud distributions . . . . .	96
6.1.2	Cloud regime definition and their climate change response . . . . .	96
6.1.3	Diurnal cycle of clouds . . . . .	97
6.1.4	Convection climate feedbacks . . . . .	97
6.2	Synergy of results . . . . .	98
6.3	Scope of future research . . . . .	99
	<b>Bibliography</b>	<b>101</b>

---

# Acknowledgement

I would like to express my gratitude to all those who, directly or indirectly, have given me their valuable support in the course of this work.

My utmost gratitude goes to my thesis supervisor Dr. Johannes Quaas for his continuous support and kindness during my PhD work. Thanks for the infinite patience, for all the help and for always having had time for me.

I would also like to thank the members of my advisory panel, Prof. Dr. Matrin Claußen and Prof. Dr. Hartmut Graßl, for their support and valuable suggestions during the course of this work. I would also like to acknowledge the help and support of Dr. Petri Räisänen from the Finnish Meteorological Institute for providing the core code for sub-column sampler.

I really appreciate being a member of the International Max Planck Research School on Earth System Modelling (IMPRS-ESM), who also financed this work. Especially the support and advise of Antje Weitz and Cornelia Kampmann helped a lot during the whole period of my PhD.

Working in the Cloud-climate feedbacks group was a great pleasure for me. My special thanks to Ákos Horváth and Irina Sandu for numerous discussions and scientific advice. Big thanks goes to my office-mate Verena Grützun for reading the parts of this thesis, her valuable comments and her forever cheerful smile. I would like to thank my colleagues: Christine Nam, Daniel Klocke, Hui Wan, Karsten Peters, Katrin Lonitz, Marco Giorgetta, Natalia Sudarchikova, Sebastian Rast, Seethala Chellappan, Suvarchal Kumar, Stefan Kinne, Thijs Heus, Torsten Weber and many others. I appreciate the administrative and logistics help by Hanna Stadelhofer, Bettina Diallo and all the friendly colleagues at the MPI Geschäftszimmer. Thank you all for your support and for providing such a fantastic work environment.

Deep gratitude goes to my brother Sidharth for “transmitting” his love and encouragement all the way from India, my parents-in-law (Shashi and Surendra Kumar Verma) and all my friends for their loving considerations and constant support. My life wouldn’t have been as exciting and happening without you people.

A heart-filled thanks to my husband Dr.-Ing. Himanshu Verma, who has been an inspirer and motivator to me for last many years. Without his trust in me, I would have not been able to reach this milestone in my life. Thank you Himanshu for being in my life and making it beautiful.

In India, the parents usually do not say “I Love You” to their kids, as they breathe, think and live for their kids: *Mummy* and *Papa* (Madhu and Suraj Bhan Singh Gehlot), you have played a huge role in bringing me up to where I am today. It would be too artificial if I have to thank you, but without your sacrifices and the

opportunities you provided me during my life's journey, I wouldn't have been able to achieve so much and come this far. I consider myself fortunate for the freedom that you provided to me in taking some of the crucial decisions in my life. Even if you were seldom physically near me through these years in Europe, your thoughts and blessings have always been a lighthouse for me, guiding me in the right direction. I cannot thank you enough but just dedicate this book to you both. Please accept it!

And finally but most importantly, I thank the Almighty for everything I have, every opportunity I have been given, all right ideas and desired support given at the right time. I thank You for your blessings for me. Without You, this journey would have been an unlived dream...

Hamburg, 17. May 2010

Swati Gehlot

---

# Abstract

Clouds are one of the most important components of the climate system, regulating the radiation budget of the Earth. In the simulation of the global climate using General Circulation Models (GCMs), cloud feedbacks contribute to a major uncertainty on account of poorly represented cloud processes. Satellite observations provide the most comprehensive view of cloud related quantities at a global scale, and are an important data source for evaluation of cloud representations in GCMs. The International Satellite Cloud Climatology Project (ISCCP) simulator is a valuable tool for analyzing GCM cloud distributions. This research focuses on diagnostic applications of the ISCCP simulator to pinpoint the ECHAM5 model deficiencies related to the cloud processes. Subgrid-scale cloud variability information using the probability density function of total water mixing ratio, is incorporated in the ISCCP simulator diagnostics to characterize the cloud property distributions. The simulator diagnostics serve as a primary tool in the model evaluation studies performed in this work.

The analysis of global average cloud distributions of ECHAM5 model reveals that high-level clouds are overestimated in the tropics, which is compensated by an underestimation of low- and mid-level clouds. The analysis suggests that convection in the model transports too much moisture to higher levels of upper troposphere, not allowing detrainment at mid-levels. High-level clouds over tropical land areas have a major contribution from this model deficiency due to large amount of convection. Evaluation of global average histograms reveal that most of these high clouds over land are optically thin clouds, which are less abundant in the observations. Land and sea diurnal cycles in the simulated cloud types are compared with ISCCP observations for four tropical test-case areas. In general, the model shows a weak diurnal behavior for deep-convective clouds and low-level clouds. In the observations, the diurnal cycle in total cloud cover is dominated by the latter in most land as well as sea areas. The diurnal peak of cloud fractions are diagnosed too early in the model compared to the ISCCP observations both for the land and sea areas.

A clustering technique for cloud regime categorization in the model output is performed in order to compare the model behavior with other model inter-comparison studies. For the tropics and the ice-free extratropics, the ECHAM5 model simulates shallow cumulus clouds as the most frequent cloud regime with qualitative agreement to the ISCCP observations, but a substantial underestimation in quantitative terms. ECHAM5 produces an excess of tropical convective and extra-tropical frontal clouds in comparison to the observations. The total climate change response of clouds to an SST perturbation, when measured by change in net cloud radiative forcing, is calculated for each cloud regime and averaged over tropics, ice-free extratropics and snow or ice-covered extratropics. The stratocumulus and stratocumulus-cumulus transition cloud regimes are responsible for 2/3 of the feedbacks, with stratocumulus alone responsible for  $\sim 50\%$ . The tropics in turn dominate the global cloud-climate feedbacks from change in net radiative cloud forcing.

The ISCCP simulator diagnostics are further used in characterizing the processes highly relevant for convection-climate feedbacks. A Lagrangian trajectory analysis is performed to track the transitions of deep-convective clouds to cirrus clouds (cirrostratus and cirrus) within the ISCCP observations and the ECHAM5 model. Forward trajectories for the ISCCP observations and model are created over which the ISCCP histograms are used for tracking the cirrus life cycle associated with deep convective events in a period of 5 days. The cloud evolutions over trajectory paths suggest that the deep-convective clouds detrain over time and gradually thin-out by the first day after the convective event. The evolution of cirrostratus and cirrus clouds begin from the convective detrainment and stay for next 3 to 4 days in relation to the convective events. We also separate the cirrus clouds formed due to convection and the ones formed in-situ due to large scale dynamics. This study reports that the detrainment cirrus in the ECHAM5 model lasts for  $20\pm 15$  hrs compared to the in-situ cirrus life time of  $17\pm 12$  hrs. Finally, the effect of these transitions in a changing/warmer climate is analyzed, in order to understand the climate feedbacks due to deep-convective cloud transitions. A perturbed model simulation with +2 K warmer SST is performed. The Lagrangian trajectory analysis suggests that more and too thick cirrostratus and cirrus clouds occur in the warmer climate compared to the present day climate. Stronger convection is noticed in the perturbed climate which leads to an increased precipitation, especially on day-2 and -3 after the convective event. The shortwave and the longwave cloud forcings increase in the warmer climate which results in an increase of net cloud radiative forcing (NCRF), leading to a positive feedback of the increased cirrostratus and cirrus clouds from a Lagrangian transition perspective.

The evaluation studies using different approaches focusing on different processes and features show consistent problems in the current model. The findings of the present day climate evaluations also persist in the simulated convection and cloud behavior in a warmer climate. This research study overall points to ways for improving the representation of convection and convection-related clouds in the GCM and thus a more reliable simulation of the climate feedbacks.

# Chapter 1

## Introduction and motivation

The different physical components of the Earth, namely the atmosphere, geosphere, cryosphere, biosphere and oceans combine to form the *climate system*. These components of the climate system interact with each other and define the overall physical behavior of the Earth system. There is a significant amount of feedbacks among these climate system elements and their processes. The hydrological cycle is one of the interesting examples showing complex interaction of oceans, atmosphere, biosphere and geosphere.

These interactions in the climate system elements can be understood by two main approaches. The first method is numerical modeling. The various processes within a climate system are represented in general circulation models (GCMs) to obtain an overall picture of how these processes interact and affect the climate. The second method for understanding the interaction processes is using observations (satellite remote sensing data, airborne and ground-based measurements). However, neither of these stand-alone methods is sufficient to achieve a complete understanding of reality. Therefore, more emphasis is required in terms of coupling models and observations in order to understand and quantify the effect of individual components of the climate system and their properties within the global climate.

Among the various important elements of the climate system, the atmosphere is a prominent component which involves several individual components in itself. Radiative transfer, cloud formation and its microphysics, aerosols and their effects, natural and long term climate variability are some of the important components and aspects of the atmosphere. Atmospheric general circulation models (AGCMs) are composed of complex dynamical interactions between the various atmospheric processes along with their physical and chemical interactions.

Clouds act as an important parameter of the Earth system as a whole. More than 60% of the Earth's surface is covered with clouds at any given point of time. Clouds are major driving force of the climate system, controlling the planetary albedo. They strongly modulate the energy balance of the Earth through convection transport, latent heat circulation, scattering of solar radiation as well as absorption and emission of terrestrial radiation. Together with influencing the global energy and generation of precipitation, clouds have a major influence on the Earth's ecosystem.

In spite of being a key element in the atmospheric circulation, the understanding of climate feedbacks to external forcings by clouds is one of the largest uncertainties in climate modeling and projection of future climate changes (IPCC, 2001, 2007). Cloud processes are poorly represented and constrained in the general circulation models. One of the prime limitations of general circulation models relates to the averaging of cloud characteristics over the model grid-mean spatial domain. In order to increase the confidence in climate change simulations, it is worth evaluating and improving the physical content of climate models and in particular the representation of clouds.

Satellite observations provide the most comprehensive view of cloud related quantities at a global scale, and are an important data source for evaluation of cloud representations in GCMs (for e.g., ISCCP or International Satellite Cloud Climatology Project (Schiffer & Rossow, 1983; Rossow et al., 1996)). The use of satellite simulators within climate models to emulate observational properties is a well known approach in model evaluation studies (Klein & Jacob, 1999; Webb et al., 2001). The ISCCP simulator is a valuable tool for obtaining detailed cloud property distributions diagnostics from a GCM, which makes the model output data to be directly comparable to the observations.

## 1.1 Clouds and their radiative effects

Clouds occur on average over 60% of the Earth's surface (Rossow & Schiffer, 1999). They cover a spatial range from less than a kilometer to thousands of kilometers in the horizontal. Cloud processes occur on temporal scales ranging from seconds to days. Clouds mainly form in the troposphere, from the surface to up to 18 km. Clouds most often form by rising air, which is thereby expanding and cooling. The cooler the air is, the less moisture it can hold so that the rising air eventually reaches its dew-point temperature where condensation starts. The reasons for the lifting of the air can be surface heating as it is the case for convective clouds, topographic barriers as is the case for orographic clouds, or the forced large-scale lifting of air by frontal air masses. Independent of the formation process, clouds form when rising air reaches its convective condensation level. Cloud droplet formation also substantially depends on the availability of cloud condensation nuclei or aerosol particles which allow water vapor to condense on their surface.

Clouds affect the energetics of the atmosphere in several ways. They influence the atmosphere's radiation budget by scattering, absorption and emission of radiation. In the shortwave spectral range, clouds are important as they backscatter the incoming solar radiation. This effect is quantified by the cloud albedo defined as the fraction of solar irradiance back scattered. The albedo of an individual cloud is dependent on cloud optical thickness which is a function of cloud properties such as cloud liquid water and ice content and cloud droplet sizes. In the long-wave, the thermal spectrum of radiation, clouds can be approximated to absorb and emit radiation like a grey body. The characteristic of clouds to re-emit thermal radiation

back to the Earth's surface and thus trapping the radiation in the troposphere often is referred to as clouds' contribution to the greenhouse effect of the atmosphere. The resultant forcing from the solar (short wave) forcing and the terrestrial (long wave) cloud forcing is termed as the net cloud radiative forcing, and it defines a net effect of clouds on radiation and the energy budget of the Earth. The overall net effect is probably negative (Ramanathan et al., 1989).

The space view of cloud observation satellites offers the ability to measure radiation budget components at the top of the atmosphere. In the recent years, several studies for evaluating the radiative effects have been carried out (Trenberth et al., 2009).

## 1.2 Model uncertainties associated with cloud processes

Although the importance of clouds within the climate system is widely recognized, their global impact on the climate system is associated with great uncertainties due to the complex space-time variation of the cloud processes (Randall et al., 2007). It has been known that the sensitivity of a climate model strongly depends on how clouds are represented in it as shown in Cess et al. (1990); Senior & Mitchell (1993); Roeckner et al. (1987), and hence different climate models simulate different cloud feedbacks as noticed by Bony et al. (2004).

One of the main reason for this uncertainty is that most of the cloud processes take place in a much smaller scale than that captured in a typical grid cell ( $\sim 30$  to  $300$  km) of a climate model. Hence, the cloud processes are *parameterized* or, are represented in terms of their effect on large scale resolved variables such as humidity, temperature and precipitation. Major problems identified in the context of convective clouds parameterization are the representation of entrainment and detrainment in convective cloud processes. Similarly, the boundary layer cloud process representations (shallow cumulus and stratocumulus clouds) also lead to a major contributor in the model uncertainty.

## 1.3 Convection and Convection-climate feedbacks

Atmospheric convection arises from buoyant or mechanical forces, and is regarded as atmosphere's way of providing efficient vertical transport of heat, mass and momentum (Rogers, 1979). Convection transports heat and moisture vertically, thereby forming a crucial link in the general circulation. Tropical convection plays a key role in the global climate. Latent heat release in organized convection drives planetary scale circulations such as the Hadley-Walker circulation and the Madden-Julian oscillation (Hendon & Woodberry, 1993). A global description of the various properties of tropical convection is thus required to fully understand the role of convection in climate.

Processes in the climate system that can either amplify or dampen the climate response to an external perturbation are referred to as climate feedbacks (Stephens,

2005; Bony et al., 2006). A change in cloud radiative effect in response to a global temperature change may produce a substantial feedback on the Earth's temperature. But the sign and the magnitude of the global mean cloud feedback depends on so many factors that it remains very uncertain (Bony et al., 2006). Climate sensitivity depends critically on radiative feedbacks associated with convection, water vapor, lapse rate, clouds, snow-, and sea ice-albedo, and global estimates of these feedbacks differ among general circulation models.

## 1.4 Key objectives

The primary objective of this PhD thesis is to analyze and evaluate some of the key processes between convective clouds and their radiative effects, in order to obtain a better understanding of the cloud processes. The key objectives of this research are listed as follows,

- Evaluation of global distribution of clouds in ECHAM5 general circulation model using satellite data (comparison of ISCCP observations with model simulated global fields of ISCCP cloud types with their distribution of cloud top height and optical thickness).
- Sensitivity of ISCCP simulator cloud diagnostics based on sub-grid scale variability of clouds.
- Evaluation of diurnal behavior of different types of clouds in different regions of the world.
- Separation of cloud regimes based on cloud properties using cluster analysis technique (Williams & Webb, 2009), and determining the total climate change response of clouds to sea surface temperature (SST) perturbation in warmer climate.
- Analysis of cloud feedbacks related to deep-convective activity. Evaluation of deep-convection transition to anvil cirrus clouds over time and the changes in cloud transition in a changing (warmer) climate.

In the current study, the ECHAM5 (Roeckner et al., 2003) atmospheric general circulation model is used together with the ISCCP simulator (Klein & Jacob, 1999; Webb et al., 2001) as a primary tool to evaluate the simulated cloud properties in comparison to satellite observations. A climate feedback study by assessing the life-cycle of convective clouds in present climate and in an idealized warming (+2 K perturbed SST) climate is performed to understand the radiative forcing of convective clouds, their formation, transition and maintenance in the upper troposphere.

## 1.5 Thesis outline

This Phd research aims at understanding the convective cloud processes within the ECHAM5 global climate model and their evaluation in comparison to satellite observations. A diagnostic application of the ISCCP (International Satellite Cloud Climatology Project) satellite simulator is adopted to make the model output directly comparable with ISCCP satellite observations. A detailed description of the ECHAM5 atmospheric GCM in terms of convective cloud parameterization scheme and the statistical cloud cover scheme is presented in Chapter 2. A section in Chapter 2 is dedicated to the description of satellite data which is used in the model evaluation studies. The basic idea of the ISCCP simulator for emulating the satellite signals within ECHAM5 GCM is explained in Chapter 2. The details of technical implementation of the ISCCP simulator version including the sub-grid scale variability information for clouds are also shown in Chapter 2.

The experimental set-up and the simulation runs used in this work are presented in Chapter 3. Cloud diagnostics sensitivity comparison using different versions of ISCCP simulators, together with a comparison of model output to satellite observations is also shown in Chapter 3. In order to characterize the model behavior relative to other model inter-comparison studies, we apply a cluster analysis (Williams & Webb, 2009) on the model simulated output, the findings of which are presented in Chapter 3. Total climate change response of clouds to +2 K SST perturbation is analyzed for all the defined cloud regimes, which is measured by change in net cloud radiative forcing. Chapter 4 presents an evaluation of the diurnal cycle of various ISCCP cloud categories as simulated in the model is done compared to the ISCCP observational diurnal cycle. The diurnal behavior of clouds is analyzed in selected tropical test regions, where the individual behavior over land and sea areas is compared for the model and the observations.

Chapter 5 explains the details of a cloud feedback study related to deep-convective clouds. The transitions from deep-convective clouds to cirrostratus and cirrus clouds over time are analyzed using a Lagrangian trajectory method based on the approach followed by Luo & Rossow (2004). The comparison of the cloud transitions in present day climate and a warmer climate with perturbed SST are also presented in Chapter 5 with some insight on the model behavior in a feedback analysis from a Lagrangian perspective.

Chapter 6 contains the main conclusions of the model evaluation studies performed in this work together with a note on synergy among findings by various evaluation techniques adopted. Some reflection on the scope for follow-up studies is also included.



## Chapter 2

# Description of model and data

*This chapter presents an overview of the ECHAM5 general circulation model which is the primary tool used in this research. The following sections explain the core physics in the current model as well as the modifications that have been implemented for testing and improving the model. A detailed description of the various versions of the ISCCP (International Satellite Cloud Climatology Project) simulator module that are used in the sensitivity runs is also presented in this chapter.*

### 2.1 Model description (ECHAM5 General Circulation Model)

For the current study ECHAM-atmospheric general circulation model is used. The climate model ECHAM5 (Roeckner et al., 2003) is the fifth generation model developed from the spectral weather prediction model of ECMWF or European Center for Medium-range Weather Forecast (therefore the first part of its name: EC) and a comprehensive parameterization package developed at the Max Planck Institute for Meteorology, Hamburg (therefore the abbreviation HAM). A detailed description of the model is presented in the subsequent sections.

#### 2.1.1 General characteristics

The ECHAM5 model consists of a spectral dynamical core based on the primitive equations and a comprehensive set of physical parameterizations. The prognostic variables i.e., temperature, vorticity, divergence, logarithm of the surface pressure, and the total water mixing ratio are represented in the horizontal by a finite series of spherical harmonics. In the vertical, the atmosphere is divided into hybrid sigma-pressure levels reaching up to the pressure level of 10 hPa (Roeckner et al., 2003). In the standard configurations, the model has 19 or 31 vertical layers. Throughout this study we will mainly use the model version with the resolution T63L31. T63 denotes the truncation of the series of spherical harmonics at the zonal and total wavenumber  $m_0=l_0=63$  ( $\sim 1.9^\circ \times 1.9^\circ$  spatial resolution on a latitude-longitude grid);

L31 refers to the usage of 31 vertical levels.

The physical parameterizations within the ECHAM5 model consider long-wave radiation, shortwave radiation, gravity wave drag (GWD), the planetary boundary layer (PBL), cumulus convection, stratiform cloud formation, and microphysics/precipitation formation.

A bulk mass flux scheme is employed for shallow, mid-level, and deep-convection based on Tiedtke (1989) with modifications for deep-convection according to Nordeng (1994). Large-scale cloud cover and large-scale condensation/evaporation can either be diagnosed by a scheme based on a threshold of relative humidity (Sundqvist, 1978), or can be predicted by a sub-grid scale variability scheme as described in Tompkins (2002). In this study, only Tompkins scheme is used. For the vertical cloud overlap considerations, maximum, random or maximum-random overlap assumption may be applied. In this study we use the maximum-random overlap assumption in the model simulation runs.

### 2.1.2 Clouds in ECHAM5

The adequate representation of clouds and cloud affecting processes in an atmospheric climate model is a challenging task. A variety of complex processes with different spatial and temporal resolutions are combined together in a climate model and hence it remains a difficult task to assess which processes are indispensable and which can be omitted for special applications without loss of accuracy.

An important limitation of the cloud parameterizations of a given climate model is the model's horizontal and vertical grid resolution. Global as well as regional climate models (with horizontal grid spacings in the range of 10 to 500 kms) parameterize the effects of convection and cloud microphysics as well as the radiative properties of clouds. Cloud processes act on scales much smaller than the order of magnitude of the model's grid scale and can not be explicitly resolved by the model. The sub-grid scale cloud processes are hence unresolved and have to be parameterized within the model.

Similar to most other climate models, the cloud simulation in ECHAM5 is divided into two parts - the stratiform and the convective clouds. The stratiform or large-scale cloud scheme within ECHAM5 includes prognostic equations for cloud liquid water and cloud ice mass mixing ratios and also the higher order moments of the total water content (only in Tompkins (2002) scheme). The large scale clouds are parameterized within the climate model to influence the radiation budget, and the convective cloud parameterizations affect the vertical transport, latent heat and the convective precipitation formation. Cloud microphysics includes rain formation by coalescence processes (autoconversion, cloud particle collection by rain and snow, aggregation of ice crystals to snow flakes, accretion of cloud droplets by falling snow), gravitational settling of ice crystals, sublimation or evaporation of falling snow/rain and also freezing and melting. Most of these processes are formulated as in Lohmann & Roeckner (1996). Fractional cloudiness is calculated from a statistical cloud cover model (Tompkins, 2002) using a probability density function (PDF) for total water

as suggested from simulations with a cloud-resolving model. Variance and skewness of the PDF are related to the sub-grid scale processes such as turbulence and convection. More details on the Tompkins scheme are explained in section 2.1.4.

The convection schemes account for clouds even if the grid scale saturation is not reached. The bulk mass-flux convection scheme by Tiedtke (1989) is employed in the ECHAM5 model. This scheme is based on steady-state equations for mass, heat, moisture, cloud water, and momentum for an ensemble of updrafts and downdrafts, including turbulent and organized entrainment and detrainment. Convective instability is determined in the Nordeng (1994) closure of the Tiedtke scheme by lifting an air parcel dry-adiabatically until it reaches the lifting condensation level. If it is still positively buoyant with respect to its surrounding, convection is activated. The result is formation of convective available potential energy (CAPE), which influences the environment by transporting heat and moisture vertically, mixing the cloud air with surrounding environmental air (entrainment and detrainment processes) and finally released by formation of precipitation. Convective precipitation in the model is diagnosed as a constant fraction of cloud water, while the remainder is detrained to serve as an input for the stratiform cloud scheme (Lohmann & Roeckner, 1996). The Tiedtke convection scheme is explained in detail in section 2.1.3.

More details including the basic physical equations of the cloud schemes in ECHAM5 are explained in the following sections. The convection scheme, the large-scale cloud scheme and their coupling are explained in a sequential order.

### 2.1.3 Convection scheme in ECHAM5

Within the ECHAM5 atmospheric model, a mass flux scheme is employed for shallow, mid-level, and deep-convection (Tiedtke, 1989) with modifications for penetrative convection according to Nordeng (1994). The Tiedtke (1989) convective parameterization scheme is based on the mass flux concept and a bulk cloud model. The scheme considers three types of convection. The first type is the penetrative or deep-convection under disturbed, conditionally unstable conditions in the presence of lower tropospheric large-scale moisture convergence. The second is shallow convection under undisturbed conditions and is mainly driven by the turbulent surface moisture flux. The third type is the so called mid-level convection that occurs mainly in conditionally unstable situations but with a cloud base well above the planetary boundary layer. Only one type of convection is allowed to take place in a grid box during each time step. An ensemble of clouds occurring in each type of convection is assumed to consist of updrafts and downdrafts. Updrafts are allowed to interact with the environment through convective entrainment and detrainment. Both the lateral entrainment/detrainment due to turbulence and the organized entrainment/detrainment due to organized inflow/outflow near the cloud base/top are considered following certain assumptions and simplifications. Downdrafts are assumed to occur at the level of free sinking (LFS), where in-cloud air mixes with environmental air and becomes unstable in relation to the surrounding environment. The mass flux at LFS is taken as 30% of the cloud-base mass flux (Tiedtke, 1989).

Cloud water detrainment in the upper part of the convective updrafts is used as a source term in the stratiform cloud water equations.

### Tiedtke scheme

The Tiedtke scheme includes a static, one dimensional cloud model, taking into account the following processes (Tiedtke, 1989):

1. Diabatic warming of the atmosphere resulting from latent heat exchange,
2. Vertical transports of heat, moisture and momentum in convective updrafts and downdrafts,
3. Interaction between up/downdrafts and the environmental air by consideration of entrainment and detrainment processes,
4. Precipitation formation.

As the Tiedtke scheme has been developed for global climate models with coarse horizontal resolutions, the cloud model aims to represent an ensemble of convective clouds located in one grid box. The properties described further are thus not representative for single convective clouds, but rather for their ensemble. Convection is further classified into three categories (as explained in Pfeifer, 2006).

- **Penetrative convection** (convection type 1): Convection type 1 is designed to cover the effects of tropical *hot towers*, that develop fast and reach high levels of the atmosphere. Penetrative convection has its basis in the near-ground boundary layer. It is mainly fed by advective transport of moisture into a grid box. Unlike as in the procedure recommended by Tiedtke (1989), the mass flux at cloud base is specified following an adjustment closure proposed by Nordeng (1994), linking the cloud base mass flux to the available convective potential energy, which should be removed by convection in a characteristic time ( $t_\tau$ ). In this way, the cloud base mass flux is inversely proportional to the adjustment time scale. This time scale strongly depends on the horizontal grid resolution of the model. In order to keep the vertical mass flux at approximately the same size as the resolved vertical velocity of the model,  $t_\tau$  must be decreased as the horizontal resolution increases (Nordeng, 1994).
- **Shallow convection** (convection type 2): Convection type 2 is designed for convection developing in undisturbed flow (no large-scale convergence). Typical convection associated with this convection type are tradewind cumuli under a subsidence inversion and daytime convection over land. Shallow convection evolves from the boundary layer. In case of shallow convection, the moisture excess in the grid box is dominated by evaporation from the surface and not dynamically by advected moisture as in the case of penetrative convection. The rates of turbulent entrainment and detrainment are by a factor of three

higher than for penetrative convection, accounting for the fact that shallow convection is usually smaller and more turbulent than penetrative convection and thus has larger exchanges with surrounding air. An important difference between penetrative and shallow convection is that there is no precipitation associated with shallow convective clouds.

- **Mid-level convection** (convection type 3): Contrary to convection type 1 and 2, mid-level convection has its roots at levels above the boundary layer. Typical examples for this type of convection are convective cells occurring in rainbands at warm fronts or in the warm sectors of extra-tropical cyclones. In such cases, convection starting from the lower levels is often inhibited by a low-level temperature inversion and convection is initiated by lifting low-level air dynamically to the level of free convection.

The Tiedtke convection scheme is unimodal, which means that only one convection type can occur in a column at a time, multi-layered convection is not allowed. Once the convection type is determined, the properties of the convective cloud ensemble are set according to the appropriate convection type. The intensity of convection and hence the maximum vertical extent of the cloud is strongly dependent on the entrainment of air into the cloud from the air masses surrounding the cloud. Entrainment and detrainment processes are separated in turbulent entrainment and detrainment, which describes the mixing of cloud air and environmental air at the cloud edges due to turbulent eddies and into organized entrainment and detrainment, which describes organized in- and outflow associated with large-scale convergence.

The convection scheme is coupled to the large-scale cloud scheme by handing over the convective cloud condensed water detrained from the updrafts to the large-scale cloud scheme. The formulation of the convection scheme restricts convective activity to one single time step. The properties of convection in one grid column of the model are assigned for every time step without reconsidering the state of convection one time-step before. Thus the model includes no explicit memory in the convection scheme, which would allow convective clouds to develop on a longer time scale.

### **Formulation of cumulus convection parameterization equations within ECHAM5**

In the ECHAM5 climate model, the contribution of cumulus convection to the large scale budgets of heat, moisture and momentum is represented by an ensemble of clouds consisting of updrafts and downdrafts in a steady state. Buoyant convection occurring on account of surface heating creates an unstable parcel of air which contributes the updraft. Entrainment is the rate at which air is included into the cloud through its sides to balance the increase of vertical mass flux in the cloud with height, and the detrainment rate is the rate at which air leaves the cloud as the cloud vertical mass flux decreases with height. Figure 2.1 shows a schematic of a cloud ensemble over a column and its development due to temperature rise  $\Delta T$ .

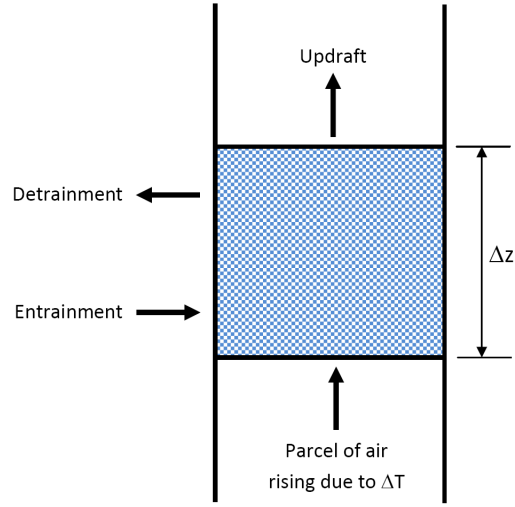


**Figure 2.1**— Schematic of cloud ensemble updraft with consideration of entrainment and detrainment

Updraft over height ( $\Delta z$ ) is shown where entrainment and detrainment are seen as the parcel further rises.

The bulk equations for mass, heat, moisture, cloud water and momentum for an ensemble of cumulus updrafts are the following,

$$\frac{\partial M_u}{\partial z} = E_u - D_u \quad (2.1)$$

$$\frac{\partial}{\partial z}(M_u s_u) = E_u \bar{s} - D_u s_u + L \bar{\rho} c_u \quad (2.2)$$

$$\frac{\partial}{\partial z}(M_u q_u) = E_u \bar{q} - D_u q_u - \bar{\rho} c_u \quad (2.3)$$

$$\frac{\partial}{\partial z}(M_u r_{l_u}) = -D_u r_{l_u} + \bar{\rho} c_u - \bar{\rho} P_u \quad (2.4)$$

$$\frac{\partial}{\partial z}(M_u u_u) = E_u \bar{u} - D_u u_u \quad (2.5)$$

$$\frac{\partial}{\partial z}(M_u v_u) = E_u \bar{v} - D_u v_u \quad (2.6)$$

where, the subscript  $u$  denotes updraft variables and the overbar denotes the variables in the surrounding environment of the updrafts (grid-box mean values). The variables in the above updraft equation are,

- $M$  = cloud base mass flux ( $kg\ m^{-2}\ s^{-1}$ ),  
 $E$  = mass entrainment rate ( $m^{-1}$ ),  
 $D$  = mass detrainment rate ( $m^{-1}$ ),  
 $s$  = dry static energy, expressed as  $(C_p T + gz)$ , where,  
 $C_p$  = specific heat capacity of air at constant pressure ( $J\ kg^{-1}\ K^{-1}$ ),  
 $T$  = absolute temperature ( $K$ ),  
 $g$  = gravitational acceleration ( $m\ s^{-2}$ ),  
 $z$  = height ( $m$ ),  
 $L$  = Latent heat of condensation/sublimation ( $J\ kg^{-1}$ ),  
 $\rho$  = density of air ( $kg\ m^{-3}$ ),  
 $q$  = specific humidity ( $kg\ kg^{-1}$ ),  
 $r_l$  = cloud water mixing ratio ( $kg\ kg^{-1}$ ),  
 $c$  = net condensation rate ( $kg\ kg^{-1}\ s^{-1}$ ),  
 $P$  = precipitation formation rate ,  
 $u$  and  $v$  = components of the horizontal wind vector ( $m\ s^{-1}$ )

Once the updraft component is calculated, the characteristics of the downdrafts are estimated. A corresponding set of equations is used for the cumulus downdrafts which are assumed to originate from mixing of cloud air with environmental air which has been cooled to its wet bulb temperature by evaporation of precipitation generated in the updrafts. The downdrafts are supposed to be initiated at the level where the buoyancy of an even mixture of cloud air and the evaporatively cool environment air becomes negative.

### Organized entrainment and detrainment

Following the updrafts and the downdrafts, the entrainment and detrainment is considered for cloud ensembles (variables  $E$  and  $D$  in equations 2.1 through 2.6). According to Tiedtke (1989), organized entrainment is consistent with the closure and is based on a moisture convergence hypothesis. As implemented in the ECHAM5 model, the Nordeng (1994) approach assumes organized entrainment to take place as inflow of air into the cloud when cloud parcels accelerate upwards, i.e. when the buoyancy is positive. Organized detrainment takes place where the air decelerates, i.e. when the buoyancy becomes negative. Organized entrainment and detrainment are therefore related to the cloud activity itself.

The organized detrainment is defined as the loss of total mass-flux due to detrainment of those clouds which are losing their buoyancy. In the ECHAM5 convective parameterization, the spectrum of clouds detraining at different levels is realized through the function based on the level where the clouds start to detrain (Roeckner et al., 2003).

### 2.1.4 Statistical cloud cover scheme

Cloud microphysical processes as well as the radiative transfer, depend crucially on the distribution of water within the model grid-cell. In a statistical cloud cover scheme, a mathematical probability density function (PDF) is assumed to represent in each large-scale model grid box the horizontal sub-grid scale PDF of the total water or  $r_t$  (vapor plus condensate). Once the particular parameters (or shape) of the PDF has been determined, cloud fraction is diagnosed as the probability that  $r_t$  exceeds relative to saturation water vapor mixing ratio  $r_s$ . The cloud condensate mean value and its PDF can also be diagnosed from the PDF of  $r_t$  relative to  $r_s$ . The components of the total water mixing ratio are expressed as  $r_t = (r_v + r_l + r_i)$  where,  $r_v$ ,  $r_l$  and  $r_i$  are mixing ratios of water vapor, cloud liquid water, and cloud ice, respectively. In ECHAM5, the sub-grid scale distribution is derived within the framework of a statistical-dynamical approach based on Tompkins (2002). This approach neglects the temperature fluctuations in the grid cell assuming that sub-grid scale cloud formation is caused solely by fluctuations in the total water content. Hence, the fractional cloud cover in the grid cell can be expressed as,

$$C = \int_{r_s}^{\infty} G(r_t) dr_t \quad (2.7)$$

where  $r_s$  denotes the saturation mixing ratio which is assumed to be constant within the respective grid-cell, and  $G(r_t)$  is the probability density function (PDF) of total water mixing ratio  $r_t$ . The subsequent task is to choose an appropriate PDF and to determine its moments for the model grid cell. For ECHAM5, the choice of the selected PDF was guided by simulations with a cloud resolving model (CRM) which was run on a horizontal domain of about 90 km×90 km and 21 km in the vertical (Tompkins, 2002). For a tropical case, a good fit to the simulated distributions of  $r_t$  can only be obtained by using the beta distribution. The beta distribution is determined by four parameters, two shape parameters,  $p$  and  $q$ , and the lower and upper bounds,  $a$  and  $b$ , respectively.

This form of the PDF was chosen by Tompkins as a pragmatic compromise; it is relatively simple and flexible, and provides, in most cases, a reasonable fit to cloud-resolving model simulations of  $r_t$ . Tompkins (2002) mainly considered the use of this approach for the diagnosis of cloud fraction, and it is used solely for this purpose in the standard version of ECHAM5.

The chosen beta distribution is an attractive candidate for the sub-grid scale distribution of total water since it has finite limits, eliminating the problem of negative or infinite total water, and can be skewed in both negative or positive directions (as in CRM data used by Klein et al., 2002). The disadvantages of this using this distribution within ECHAM5 include that the skewness range is limited to plus 2 (i.e., only positive distribution), and that transcendental functions such as the incomplete beta function must frequently be evaluated (done with look-up tables).

The difficult part of the parameterization is adequately prognosing the mean, width, and asymmetry of the total water ( $r_t$ ) PDF. The PDFs of  $r_t$  at the detrain-

ment levels of deep-convection are highly skewed. Convective towers directly detrain cloud condensate to form upper-level cirrus anvil cloud and extensive stratiform cloud coverage. Cumulus parameterization schemes already represent the transport of the mean quantities of water vapor and cloud, but it is clear that the deep-convective process also increases the variance of the water vapor by introducing localized perturbations as shown by Liao & Rind (1997). Moreover, as noticed by Tompkins (2002), clouds detrain high mixing ratios of cloud condensate and introduce a significant positive skewness into the distribution of cloud. However, other sub-grid scale processes along with convection such as turbulence and microphysics also affect the evolution of  $q$  and  $(b - a)$ . The higher order moments such as variance and skewness are uniquely determined by  $a, b, p$ , and  $q$ .

## 2.2 ISCCP satellite data used in model evaluation

In order to compare the model simulation diagnostics to the observations, we use ISCCP satellite data. ISCCP stands as an abbreviation to International Satellite Cloud Climatology Project, which is operational since year 1983 (Schiffer & Rossow, 1983). The ISCCP climatological data is created using the radiance measurements from a visible channel and an infrared channel on up to five geostationary and two polar orbiting satellites (Rossow et al., 1996). Surface soundings together with the TIROS Operational Vertical Sounder (TOVS) System for temperature and moisture sounding are used as input to the measurements. The visible channel (VIS) is used to derive cloud optical thickness ( $\tau$ ), and the infrared channel (IR) is used to derive cloud top temperature and hence the cloud top pressure ( $p_{top}$ ).

The ISCCP analysis begins by classifying each individual satellite pixel, about 4-7 km in size, as either cloudy or clear (Rossow & Garder, 1993). A pixel is defined cloudy if the IR or VIS radiance differs from the corresponding clear sky value by more than the detection threshold (change from the clear radiance required to detect a cloud, explained in Rossow & Schiffer, 1999). Clouds that produce radiance changes that are too small or of the wrong sign are not detected. Clouds are assumed to cover individual pixels completely, so fractional areal cloud cover (reported as values from 0 to 1) is determined only for larger areas (i.e., 280 km across or final regridded resolution of ISCCP D2 product) in the ISCCP datasets by the fraction of all pixels in each area containing clouds. The precision of individual cloud cover values for these areas is determined by the total number of pixels collected; for the sampled ISCCP data at one time, this number ranges from 20 to 120, about 70 on average in a 280 km<sup>2</sup> grid. If an individual pixel is defined cloudy, then comparison of the observed radiances to those predicted by a radiative transfer model (Rossow & Schiffer, 1991) determines a cloud-top temperature from the IR radiances (both day and night) and a visible optical thickness ( $\tau$ ) from the VIS radiance (daytime only). As shown in the analysis by Nakajima & King (1990), the cloud optical thickness can be determined by the reflection function at a non-absorbing visible wavelength of  $0.75\mu m$  with little dependence on the droplet radius. Hence, the visible channel

during the sunlit time of the day are used in retrieval of the cloud optical thickness in the ISCCP observations.

Cloud tops in ISCCP are derived from the thermal infrared radiance of a cloudy pixel, which is translated to a pressure using the TIROS Operational Vertical Sounder (TOVS) temperature profiles. The presence of an optically thin cloud above an optically thick one would lift the pixel infrared emission level to the middle troposphere resulting in the retrieval of a middle level cloud in the place of the two overlapping cloud layers. The use of the ISCCP simulator on the model cloud parameters accounts for this effect as it also outputs a middle level cloud top pressure in a similar situation. In addition to this effect, any systematic biases in the TOVS temperature profiles would result in systematic errors in the ISCCP cloud top pressures. More details on the ISCCP data retrieval are explained in Rossow & Schiffer (1991), Rossow et al. (1996) and Rossow & Schiffer (1999). Typical cloud types are essentially classified according to their top pressure and optical thickness as described in detail in Rossow & Schiffer (1999) and shown in figure 2.2.

Composite subgrid-scale clouds of six ranges of optical depth are defined for seven pressure ranges of cloud top height. As seen in figure 2.2, the categories of clouds are based on a two-dimensional distribution of optical thickness and top pressure of clouds. The range of cloud optical thickness (0 to 379) and cloud top pressure (1000 to 50 hPa) is further subdivided into 6 and 7 bins, respectively, which are used for defining the individual 42 cloud types of ISCCP classification. The composite of the top 3 bins of cloud top pressure over all the bins of optical thickness represent the high cloud cover or the HCC. Similarly the next 2 bins and the last 2 bins of cloud top pressure contribute to the middle and low cloud cover (MCC and LCC, respectively). This distribution is also referred as ISCCP  $p_{top} - \tau$  joint histogram.

The ISCCP data sampling is done every 3 hours (or 4 time-steps in the day-light) and the spatial resolution is 280 km $\times$ 280 km. The ISCCP data histograms are used for comparison with the model output with the ISCCP simulator. For computation of the diurnal cycle from the ISCCP data, the histograms are averaged over the respective bins of cloud types for each time step and then further averaged for each corresponding time step at 0300, 0600, 0900 hours UTC and so on.

### 2.3 ISCCP satellite simulator in ECHAM5

This section is dedicated to the explanation of the ISCCP (International Satellite Cloud Climatology Project) simulator which is employed in the model runs for this work. The details of the technical implementation of the simulator module within the model, its added advantages and limitations are presented in the following paragraphs.

The ISCCP simulator, as the name suggests, is a model based *simulator* to mimic the satellite products as seen by the ISCCP retrievals. The primary motivation for the creation of the ISCCP simulator coupled with a GCM is the possibility to compare the model output one-to-one with the ISCCP satellite data. The simulator

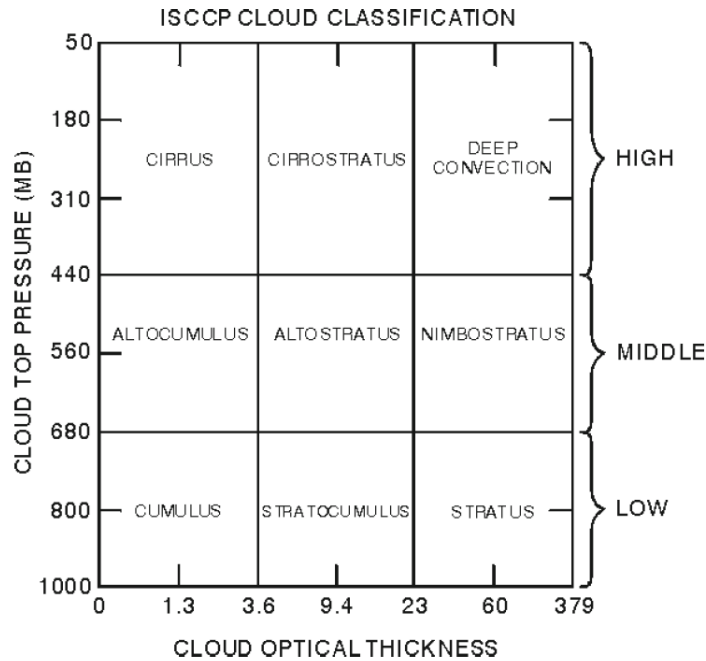


**Figure 2.2**— ISCCP cloud classification based on  $\tau$  and  $p_{top}$  joint histogram. Source: Rossow & Schiffer (1999)

itself is a run-time diagnostic tool to analyze the model output by mimicking the satellite signals as computed from three basic model variables i.e., cloud optical thickness ( $\tau$ ), cloud top pressure ( $p_{top}$ ) and cloud fraction. Hence essentially, the simulator shields the low-level clouds from above and samples only the sunlit scenes for the retrieval of the cloud optical thickness together with sub-grid scale variability. That is, at every grid point in the model, account is taken of how a satellite would view an atmospheric column with profiles of grid-box mean physical properties of the model. For example, only one cloud-top pressure  $p_{top}$ , can be assigned by ISCCP to each satellite pixel, and in the case of multi-layer clouds this is usually the  $p_{top}$  of the highest level cloud. At a coarser scale, the grid-box mean value is then the cloud property averaged over all satellite pixels within the grid-box. In sampling this sub-grid scale variability in the GCM, the model's vertical profile of cloud fraction and its overlap assumption are used to determine what fraction of the grid box is covered by clouds of a given range of  $p_{top}$  and cloud optical depth  $\tau$ .

The basic version of the ISCCP simulator and improvements in the simulator diagnostics are applied as a part of this research. The details of the technical implementation of the simulator are explained in the following subsections.

### 2.3.1 Basic ISCCP simulator

The simulator version based on the development by Klein & Jacob (1999) and Webb et al. (2001) is referred to as the basic version of the ISCCP simulator in this work. This simulator version is hereafter called as “ECHAM5-basic”. The simulator is added as a run-time diagnostic module in the ECHAM5 model. This module uses the grid-box-mean values of model generated cloud fraction to mimic the ISCCP algorithm by downscaling the grid level cloud fraction to cloudy and cloud-free sub-columns (as seen from top, similar to a satellite).

Within the core of the code, a module named SCOPS (Subgrid Cloud Overlap Profile Sampler) samples the sub-grid distribution of clouds within a model grid-box using a pseudo-random sampling process. It takes vertical profiles of (large scale) cloud amount as input and applies a cloud overlap assumption to provide a number of cloud profiles sampled from random positions within the grid-box. Each layer of these sub-columns is entirely clear or overcast with a homogeneous cloud. In the standard ECHAM5 model version a maximum-random overlap assumption in the vertical is used for generation of the sub-grid variability consistent with the model radiation code.

In the next step the process module of ICARUS (or ISCCP Clouds and Radiances Using SCOPS) emulates the ISCCP retrieval using the profiles extracted from the GCM grid-box via SCOPS (Klein & Webb, 2009). This mimics the procedure of ISCCP retrieval algorithm to assign the fractional area covered by a given cloud type as the fraction of satellite pixels in a grid-box (or, 280-km region in ECHAM5 T63 resolution) that contain clouds with a range of  $p_{\text{top}}$  and  $\tau$ . As a diagnostic, the grid-box mean cloud properties and a joint histogram of  $p_{\text{top}}$  and  $\tau$  are produced.

Table 2.1 shows the various classifications of cloud types and their definitions in the ranges of  $p_{\text{top}}$  and  $\tau$ . With the simulator two types of  $p_{\text{top}}$  are derived from the model data. The first  $p_{\text{top}}$  is the physical cloud-top pressure, i.e., the midpoint pressure of the highest model level containing clouds. The second  $p_{\text{top}}$  is an emissivity-adjusted cloud-top pressure. It accounts for the fact that in the case of thin (low emissivity) clouds overlying thick (high emissivity) clouds, the satellite is likely to overestimate  $p_{\text{top}}$  and underestimate the physical cloud-top altitude. If  $\tau$  of the column is low enough, ISCCP can use  $\tau$  to estimate the emissivity of a single-layer cloud and make a smaller error in  $p_{\text{top}}$ . However, this method does not work when  $\tau$  is large and the upper levels of the cloud have low emissivity. The method to derive an emissivity-adjusted  $p_{\text{top}}$  follows ISCCP retrieval procedures and thus accounts for these satellite limitations (Klein & Jacob, 1999).

#### Detailed algorithm for simulating ISCCP clouds from ECHAM5 model

The pseudosatellite or the simulated ISCCP cloud data is produced by accounting for two important characteristics of satellite observations of clouds. The first is that passive satellite sensors identify clouds by their tops and do not directly determine their bases or geometric thicknesses. For example, if a high-level cloud overlies a low-level cloud, it will generally be identified as only a high-level cloud by a satellite.

Cloud type category	$p_{\text{top}}$ - range (hPa)	$\tau$ - range
Low-top thin	$680 < p_{\text{top}} \leq 1000$	$0.1 < \tau \leq 3.6$
Low-top medium	$680 < p_{\text{top}} \leq 1000$	$3.6 < \tau \leq 23$
Low-top thick	$680 < p_{\text{top}} \leq 1000$	$23 < \tau \leq 379$
Middle-top thin	$440 < p_{\text{top}} \leq 680$	$0.1 < \tau \leq 3.6$
Middle-top medium	$440 < p_{\text{top}} \leq 680$	$3.6 < \tau \leq 23$
Middle-top thick	$440 < p_{\text{top}} \leq 680$	$23 < \tau \leq 379$
High-top thin	$50 < p_{\text{top}} \leq 440$	$0.1 < \tau \leq 3.6$
High-top medium	$50 < p_{\text{top}} \leq 440$	$3.6 < \tau \leq 23$
High-top thick	$50 < p_{\text{top}} \leq 440$	$23 < \tau \leq 379$

**Table 2.1**— Classification of cloud types by range in cloud-top pressure ( $p_{\text{top}}$ ) and optical depth ( $\tau$ ). Modified after Klein & Jacob (1999).

The second characteristic that affects satellite views of clouds is that satellites may underestimate the altitude of clouds with partial emissivity, especially if the partial emissivity cloud lies above an optically thick cloud.

Every vertical level of a grid column of the model has the amount of liquid, ice, and the fraction of the grid box volume that contains cloud. The vertical profile of cloud amount together with the cloud overlap assumption provides information about what portion of clouds from each level contain no clouds above them and thus are visible by a satellite, or which portion of clouds from each level are covered by clouds above and are not visible from space. To simulate the overlapping of clouds, each grid column of the model is subdivided into  $N$  sub-columns in which the cloud fraction is assigned to be zero or one at every model level. To arrive at this distribution of cloudy and clear-sky sub-columns, several assumptions were made, details of which are explained below.

First, it is assumed that clouds fill the grid box completely in the vertical; i.e., the fraction of grid box volume that contains cloud is equal to the fraction of the horizontal area of a grid box that contains cloud. Second, at each level the specification of which sub-columns contain cloud is entirely consistent with the cloud overlap assumption used for the sub-grid scale flux calculations in the radiation scheme. The overlap assumption currently used in the ECHAM5 is maximum-random overlap.

It can be described using the following equation, which specifies the total horizontal area ( $C$ ) covered by clouds in between the top of the atmosphere and the given model layer ( $k_{\text{max}}$ )

$$C = 1 - \prod_{k=1}^{k_{\text{max}}} \frac{1 - \max(a^{k-1}, a^k)}{1 - \min(a^{k-1}, 1 - \epsilon)} \quad (2.8)$$

where  $a^k$  is the cloud fraction of level  $k$ , and  $\epsilon = 10^{-6}$ . Equation 2.8 yields random overlap for clouds that do not occur in adjacent vertical levels but maximum overlap if clouds occur at adjacent levels. At each level, the number of sub-columns that

contain cloud is equal to the nearest integer value of  $100a^k$ . The use of equation 2.8 provides a total cloud fraction ( $C$ ), by applying it from the model top to the level  $k$  given the distribution of clouds layer by layer.

The amount of liquid and ice at each level must be divided among the cloudy sub-columns of each level. Currently, each cloudy sub-column is filled with the same amount of liquid and ice assuming a constant in-cloud water ( $r_{\text{cld}(l)}^k$ ) or ice content ( $r_{\text{cld}(i)}^k$ ) defined as

$$r_{\text{cld}(l)}^k = \frac{r_l^k}{a_{\text{int}(l)}^k} \quad (2.9)$$

where,  $r_l^k$  is the grid-mean liquid water content at level  $k$  and  $a_{\text{int}(l)}^k$  is a rounded cloud fraction calculated as the fraction of sub-columns at each level that contain cloud. A similar relation can be written for the cloud ice, replacing the subscript ( $l$ ) with ( $i$ ) in equation 2.9. Consideration is then given to how a satellite would detect a distribution of cloud tops and cloud optical depths from this allocation of clouds into sub-columns. The grid-box mean in-cloud optical depth  $\tau$ , which is computed within the radiation code of ECHAM5 model is used, and then distributed to the sub-columns.

To calculate the pressure of the cloud top  $p_{\text{top}}$ , two methods are used. The first method is to merely assign  $p_{\text{top}}$  as the mid-level pressure of the highest level with cloud for each sub-column. This cloud top is the true or *physical* cloud-top pressure. However, if the emissivity of the clouds' uppermost layers is not close to unity, then the satellite will have difficulty detecting the true cloud-top pressure. If the sub-column contains thin cirrus with no cloud beneath, ISCCP has a method to account for partial cloud emissivity to determine the true cloud-top pressure. However, if the partial emissivity cirrus is above an optically thick lower-level cloud or is part of a cloud whose lower layers have close to unit emissivity, then ISCCP will overestimate the cloud-top pressure (and thus underestimate its true altitude). An emissivity-adjusted cloud-top pressure is derived by crudely simulating the infrared water vapor window brightness temperature for each sub-column and then following the procedures ISCCP would use to derive cloud-top pressure. The radiance at the top of the atmosphere  $I$ , is the sum of the radiance emitted from each model level  $k$  multiplied by the transmittance  $T_r$ , from level  $k$  to the top of the atmosphere (layer 31) plus the contribution of the surface emission ( $\epsilon^{\text{sfc}}$ ), expressed as in Klein & Jacob (1999),

$$I = \sum_{k=1}^{k_{\text{max}}} T_r^k \epsilon^k f\{T^k\} + T_r^{k_{\text{max}}} \epsilon^{\text{sfc}} f\{T^{\text{sfc}}\} \quad (2.10)$$

where,  $\epsilon^k$  is the emissivity of level  $k$ ,  $T^{\text{sfc}}$  represents the transmittance at the surface, and  $f\{T^k\}$  represents a quantity linearly proportional to the radiation emitted by a blackbody at  $11\mu\text{m}$  (or, minimum brightness temperature at layer  $k$ ).  $f\{T^k\}$  can be expressed as,

$$f\{T^k\} = [\exp(1307.27 \text{ K} / T^k) - 1]^{-1} \quad (2.11)$$

where  $T^k$  is the model temperature at level  $k$ . Within the atmosphere, the emissivity of level  $k$  depends on the occurrence of cloud and is derived from the visible optical depth that is due to cloud in level  $k$  (Rossow & Schiffer, 1991), hence  $\epsilon^k$  can be written as,

$$\epsilon^k = 1 - \exp(-\tau^k/2) \quad (2.12)$$

where  $\tau^k$  is the cloud optical depth of the sub-column of level  $k$ . The factor of  $1/2$  in equation 2.12 is the factor to convert visible optical depths to infrared optical depths. For the surface, an emissivity of 0.99 is used. The transmittance ( $T_r$ ) from level  $k$  to the top of the atmosphere is given by the product of the transmissivities of each of the levels ( $j$ ) above, giving

$$T_r^k = \prod_{j=1}^{k-1} (1 - \epsilon^j) \quad (2.13)$$

with  $T_r^1 = 1$ .

After, the radiance at the top of the atmosphere  $I$  has been calculated for each sub-column, consideration is given to how ISCCP would use this radiance to derive a cloud-top pressure. Regardless of the number of cloud layers, ISCCP interprets the radiance from each pixel in terms of a single cloud and retrieves only one cloud top pressure. The emissivity of the cloud ( $\epsilon^{cld}$ ), is determined from the total optical depth of the sub-column  $\tau$ ,

$$\epsilon^{cld} = 1 - \exp(-\tau/2) \quad (2.14)$$

The radiance at the top of the atmosphere  $I$ , is assumed to be the sum of the emission from this single cloud and the portion of the emission from the surface that is transmitted through this single cloud,

$$I = \epsilon^{cld} f\{T^{cld}\} + (1 - \epsilon^{cld}) \epsilon^{sfc} f\{T^{sfc}\} \quad (2.15)$$

Subsequently,  $T^{cld}$  is varied until equation 2.15 is satisfied. The emissivity adjusted cloud-top pressure is then assigned to the pressure of the model level nearest the surface in which  $T^{cld}$  occurs. To mimic the ISCCP satellite product at every grid point of the model, the fraction of sub-columns that contain clouds within the very same ranges of cloud-top pressures and visible optical depths is computed (see Table 2.1). In this way an equivalence is made between the fractional areas covered by certain types of clouds as seen by the satellite and simulated from the model.

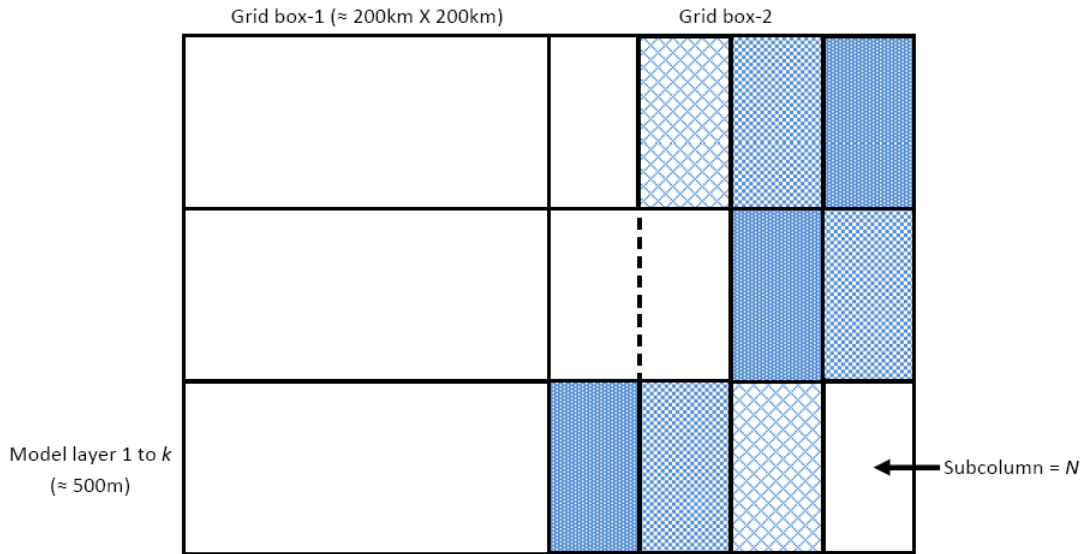


**Figure 2.3**— Schematic of stochastic cloud generator. As shown in the example model grid-box, the generated random sub-columns account for the horizontal variability at each model layer using the PDF of total water mixing ratio ( $r_t$ ) from Tompkins (2002).

### 2.3.2 Addition of sub-grid column generator in ISCCP simulator

In the basic version of the ISCCP simulator the only sub-grid scale variability considered is the vertical cloud overlap assumption. A better estimate of this sub-grid scale variability can be done by using the horizontal PDF of the total water content and hence *stochastically* generating a number of either cloudy or clear sub-columns in each model grid box. In the implementation of this sub-column generator into ECHAM5 (called as “ECHAM5-subgrid” hereafter), we use the stochastic generator based on the work by Räisänen et al. (2004). The generator is initialized with information from the GCM grid cell mean values (cloud fraction, liquid water and ice amount) and with the horizontal PDF of cloud water (Tompkins cloud scheme of beta distribution for current case; Tompkins, 2002) and vertical maximum-random overlap assumption. Figure 2.3 shows the details of the sub-columns generated within the ECHAM5-subgrid version, where the grid-cell inhomogeneity of cloud water at each model is shown for a single model grid-box with  $k$ -layers.

In the generation of sub-columns, the sub-column cloud fraction  $\alpha_j^k$  in the  $k$ th layer of  $j$ th sub-column is assumed to be either 0 or 1 (cloud free or cloud filled, similar to the standard ISCCP simulator). The atmosphere is divided into  $k$  layers ( $k=k_{\max}$ , at the top of atmosphere), and  $N$  sub-columns are generated. In the current study, the sensitivity of changing the number of sub-columns in the ECHAM5-subgrid ISCCP simulator version was tested for three cases ( $N=40$ ,  $N=100$  and  $N=1000$ ), with no substantial difference in the cloud diagnostics (not shown). The model results presented in this version of ISCCP simulator are generated by using  $N=100$  sub-columns.

As explained in section 2.1.4, the stochastic cloud scheme defined by Tompkins (2002) operates on total-water mixing ratio  $r_t$  (condensed ( $r_l$ ) + vapor ( $r_v$ )) and uses the beta probability density function  $P(r_t)$  to describe fluctuations in  $r_t$ . The sub-column generator is applied to this scheme by setting cloud fraction for sub-column cells. The subgrid-scale variability of cloud condensate amount in each layer is derived directly from the beta distribution of total water content. The total-water mixing ratios ( $r_{t,j,k}$ ) for the  $j$ th column of the  $k$ th model layer for all cells are generated by solving the equation for beta distribution PDF as follows,

$$y_{j,k} = \int_0^{r_{t,j,k}} P_k(r_t) dr_t \quad (2.16)$$

where,  $y_{j,k}$  is the cumulative frequency distribution of the total water mixing ratio  $r_t$ , and  $P_k(r_t)$  is the corresponding distribution function of  $r_t$  for the  $k$ th layer. More details on the sub-column generator are detailed in Räisänen et al. (2004).



## Chapter 3

# Evaluation of global cloud properties in model using satellite data

*An evaluation of the model simulated global fields of various cloud properties and cloud types are presented in this chapter. Sensitivity studies for comparing different versions of the ISCCP simulator are shown. The results from the ISCCP simulator model version coupled with the statistical cloud cover scheme (ECHAM5-subgrid) are compared with ISCCP satellite observations for model evaluation. A detailed analysis of global average ISCCP  $\tau - p_{\text{top}}$  joint histograms is also presented in this chapter. In the histogram comparisons, we pin point the model deficiencies in terms of cloud diagnostics using the ISCCP simulator.*

*The use of a clustering technique based on the work of Williams & Webb (2009) is performed on the ISCCP simulator output of ECHAM5-subgrid model version for defining the global cloud regimes and their respective climate change response. This analysis is performed to evaluate the performance of ECHAM5 cloud cover diagnostics in comparison with other CFMIP (Cloud Feedback Model Intercomparison Project) studies (Williams & Tselioudis, 2007; Williams & Webb, 2009).*

### 3.1 Experimental setup and description of sensitivity runs

The model runs are coupled with an additional module of ISCCP simulator based on Klein & Jacob (1999) and Webb et al. (2001) for a detailed diagnostic analysis of cloud processes in ECHAM5. The ISCCP simulator and its versions used for this study are explained in chapter 2 (section 2.3). The AMIP (Atmospheric Model Intercomparison Project) observational monthly mean sea surface temperature (SST) and sea-ice extent boundary conditions are used for the ECHAM5 model simulation input boundary data. The model output has an additional set of output stream for the ISCCP simulator which has a three-hourly output of ISCCP variables, similar

to the model standard output.

The experimental setup consists of model simulations for the summer months (June, July and August or JJA) of year 2002 with prescribed SST/sea-ice. The simulations have been carried out in the T63 horizontal resolution ( $\sim 1.8^\circ \times 1.8^\circ$  grid-box) and 31 vertical levels. All the model runs were simulated for 1 year (Year 2002) after an initial spin-up of 1 year. Within the simulations, the two different versions of the ISCCP simulator, i.e., ECHAM5-basic version (described in section 2.3.1) and ECHAM5-subgrid version (described in section 2.3.2) are employed. The next section shows the differences in cloud properties as diagnosed by these two ISCCP simulator versions.

### 3.2 ISCCP simulator version sensitivity analysis

In order to realize the differences between the implemented versions of the ISCCP simulator, we compare the global averaged cloud fraction values for two versions of ISCCP simulator. The global model data is separated into global land and global sea areas using the land-sea mask. This separation is done to facilitate the evaluation of characteristic cloud type distributions for land and sea areas within the model simulations.

Table 3.1 shows a quantitative comparison of the ISCCP simulator cloud cover diagnostics from the ECHAM5-basic and the ECHAM5-subgrid version. As listed in table 3.1, following are the main findings from the comparison of two versions of the ISCCP simulator diagnostics for different cloud categories:

- The overall total cloud covers for the land area as well as the sea area increase in the ECHAM5-subgrid version of ISCCP simulator diagnostics. The biggest contributor to this increase over land are the optically thin clouds (i.e.,  $\tau = 0$  to 3.6) with 6% more clouds in absolute cloud fraction compared to the basic version. A small decrease ( $\sim 2\%$ ) in the medium thick (i.e.,  $\tau = 3.6$  to 23) cloud diagnostics in land areas is seen together with similar increment in optically thick clouds (i.e.,  $\tau = 23$  to 379) for land areas. The cloud cover over sea shows an increase ( $\sim 2\%$ ) for thin, medium and thick clouds in the ECHAM5-subgrid ISCCP simulator compared to the ECHAM5-basic version diagnostics.
- The overall high clouds over the land increase ( $\sim 1\%$ ) together with a decrease for the sea area ( $\sim 3\%$ ) for the ECHAM5-subgrid version compared to the ECHAM5-basic version. This change in overall high clouds is due to the similar changes in the thin high clouds for land and sea areas in the ECHAM5-subgrid version. The medium and thick high clouds over land area as well as over sea area in ECHAM5-subgrid version show a decrease of  $\sim 1\%$  compared to the cloud fraction in ECHAM5-basic version.
- Mid-level cloud fraction (both, over land and over sea) show a significant overall increase in the ECHAM5-subgrid version ( $\sim 5\%$  and  $\sim 3\%$  increase in abso-

		ECHAM5- basic Land	ECHAM5- subgrid Land	ECHAM5- basic Sea	ECHAM5- subgrid Sea
TCC (%)	Thin	16.9	22.3	21.3	22.8
	Medium	15.6	13.4	26.5	28.1
	Thick	18.5	19.9	14.2	16.3
	Overall	51.1	55.7	62.3	67.3
HCC (%)	Thin	16.1	18.7	18.8	17.8
	Medium	7.6	6.3	7.7	6.4
	Thick	7.0	6.5	5.5	4.6
	Overall	30.71	31.5	32.0	28.8
MCC (%)	Thin	0.55	2.6	0.90	1.8
	Medium	3.1	3.5	4.5	5.2
	Thick	6.2	7.8	3.6	5.4
	Overall	9.8	13.9	9.1	12.4
LCC (%)	Thin	0.44	1.0	1.5	3.2
	Medium	4.8	3.6	14.5	16.5
	Thick	5.2	5.5	5.1	6.3
	Overall	10.4	10.1	21.1	26.0

**Table 3.1**— Mean cloud cover fraction of global land and global sea ISCCP cloud cover for two versions of ISCCP simulator (JJA 2002). The respective cloud fraction values for TCC, HCC, MCC and LCC in are in percentage.

lute cloud fraction for land and sea, respectively). This increase is dominated by increment in the diagnostics of thin mid-level clouds in the ECHAM5-subgrid version compared to the ECHAM5-basic version.

- The diagnostic improvement in using the ECHAM5-subgrid version is very prominent in the distribution of low-level oceanic clouds over the sea. The overall low cloud amount over sea increases in the ECHAM5-subgrid version by  $\sim 6\%$  in the absolute cloud fraction compared to the ECHAM5-basic version. This increment in cloud fraction over sea is distributed among all the optical thickness categories. Over the land areas, no substantial increase in low cloud fraction is seen in the ECHAM5-subgrid version compared to the basic version.

The use of sub-column sampler in the ECHAM5-subgrid version shows a reasonable similarity with the cloud cover average diagnostic values of ECHAM5-basic version. Based on the comparison in table 3.1, the ECHAM5-subgrid version of ISCCP simulator provides a more realistic diagnostics of the cloud types, since it uses the derived probability density function for cloud cover variation in the simulator. For the rest of the analysis shown in this thesis, the ECHAM5-subgrid version is used for the ISCCP simulator diagnostics. The sections 3.3 and 3.4 show a detailed

comparison of the ECHAM5-subgrid version model ISCCP simulator diagnostics with the ISCCP observations.

### 3.3 Global distribution of ISCCP cloud types

The model derived global distribution of simulated clouds for different ISCCP cloud categories are compared with the ISCCP satellite observations. The spatial resolution for the ISCCP observations is  $2.5^\circ \times 2.5^\circ$  whereas the ECHAM5 model resolution is  $\sim 1.8^\circ \times 1.8^\circ$ . In order to avoid the observational artifacts in the polar regions, we extract the global data for a latitude range of  $\pm 60^\circ$ . Throughout this chapter the values of the individual cloud cover types are expressed in absolute percentage of cloud fraction.

The ECHAM5-subgrid version of ISCCP simulator (explained in section 2.3.2 of chapter 2) is used in order to show the model cloud deficiencies from a diagnostics point of view. Figure 3.1 shows the time averaged (JJA 2002) ISCCP observations in comparison to the differences with ECHAM5-subgrid version model simulated ISCCP cloud cover. The cloud categorization for high, deep-convective, mid-level and low clouds is based on the ISCCP cloud classification for cloud optical thickness and cloud top pressure (defined in table 2.1 in chapter 2). Figure 3.1(a), figure 3.1(c) and figure 3.1(e) show the distribution of ISCCP observations for the high cloud cover (HCC), mid cloud cover (MCC) and low cloud cover (LCC) respectively. The color shading shows the respective cloud fraction in percentage for HCC, MCC and LCC. The observations show that the ITCZ belt ( $\pm 20^\circ$  latitude) are abundant in the high clouds (figure 3.1(a)), specially in the summer monsoon region of south Asia and tropical warm pool around Australia. The mid-level clouds occur mostly over the mid-latitudes and snow covered extra-tropics. Similarly the low clouds are observed along the global oceanic regions namely the marine shallow cumulus and stratocumulus clouds around Californian coast, north-west South America, west coast of Africa and Australia.

The model derived global cloud distributions are subtracted from the ISCCP observations for evaluating the model behavior in cloud diagnostics. Differences in ISCCP observations and model for the global distribution of high clouds, mid clouds and low clouds are shown in figure 3.1(b), 3.1(d) and 3.1(f) respectively. The color shading in these plots show the respective differences in the model ISCCP simulator compared to the ISCCP observations. Hence, the negative numbers (shades of blue) on the colorbar represent the overestimation of cloud fraction, whereas the positive numbers (shades of yellow to red) represent the underestimation of cloud fraction in comparison to the observations. The green color shade on the difference plots represent a model to observation bias of around  $\pm 10\%$ .

The overestimation of high-level clouds from ECHAM5-subgrid simulator version in the tropics ( $\pm 20^\circ$  latitude belt) and the mid-latitudes is seen in comparison to the observations (model bias values from observational cloud cover ranges up to 40% of cloud fraction overestimation in the model). Our analysis shows that substantial part ( $\sim 40\%$ ) of this overestimation is diagnosed in the form of thin cirrus clouds

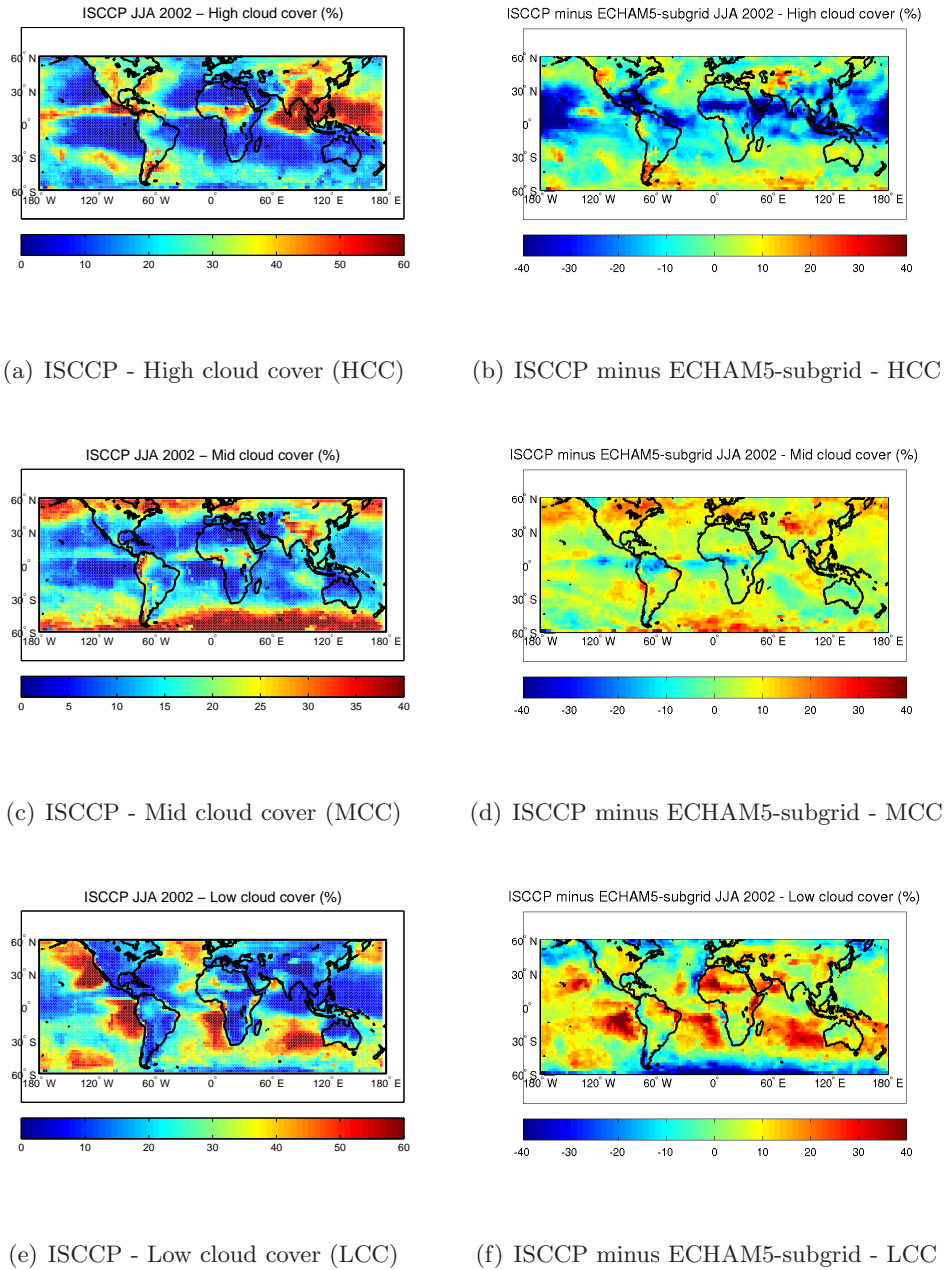


**Figure 3.1**— Comparison of ISCCP observations and model simulated cloud cover (ECHAM5-subgrid ISCCP simulator version) for JJA 2002. The subplots show ISCCP observational clouds (HCC, MCC and LCC) and their respective differences (bias) with the ECHAM5-subgrid ISCCP simulator version. The colorbar represents the respective cloud fractions in absolute percentage, and is different for HCC, MCC and LCC in observation and model bias plots.

(explained later in section 3.4). The model diagnoses a much stronger convection (on account of the convective detrainment occurring only at higher levels of the atmosphere) as compared to the observations, which leads to a larger amount of high cloud fraction (see section 5.3 for a more detailed analysis of the deep-convection transition).

Figure 3.1(d) shows the ECHAM5-subgrid version model bias from ISCCP observations for mid-level cloud cover. The extra-tropical mid-level clouds are captured relatively well in the ECHAM5-subgrid version with average bias less than  $\pm 10\%$ . However, mid-level clouds are underestimated ( $\sim 10\%$  to  $\sim 30\%$ ) by the model for the continental Greenland as well as over Southern ocean. The diagnostics of ECHAM5-subgrid also shows an overestimation ( $\sim 20\%$  to  $\sim 30\%$ ) of the mid-level clouds over equatorial Atlantic ocean, central Africa and northern coast of South America.

The model-derived (ECHAM5-subgrid version) low cloud cover distribution bias with ISCCP observations is shown in figure 3.1(f), where the distribution bias is  $\sim 20$  to  $30\%$  underestimation of low cloud cover compared to the observations. The model diagnostics show an underestimation ( $\sim 30$  to  $40\%$ ) of the marine boundary layer clouds relative to the observational data specially along the Californian coast, western coast of South America, and along west African coast. The southern pacific shallow cumulus clouds are also not well captured (underestimated by  $\sim 10\%$ ) by the model when compared to ISCCP observations for low cloud cover. The inclusion of the sub-grid scale variability in the form of probability density function of total water leads to a better diagnostic of the low cloud cover when compared to the standard ISCCP simulator (see section 3.2 for details).

### 3.4 Comparison of global average histograms

The model evaluation related to the global distribution of clouds shows that the ECHAM5 model overestimates the high clouds, and simultaneously underestimates the mid-level and low cloud cover in comparison to the ISCCP observations. However, the global distributions of high, mid and low clouds are not sufficient in determination of the model deficiencies related to the optical thickness of the clouds. The ISCCP histograms having a joint distribution of cloud top pressure and optical thickness serve as an efficient means to analyze the cloud distributions based on firstly, how high the clouds are, and secondly how thick the clouds are. These properties represent the cloud radiative characteristics, and are useful in evaluating the model cloud representations. The global average model simulated joint  $\tau$ - $p_{\text{top}}$  histograms are compared with the satellite observations for evaluating the composition of simulated ISCCP clouds on the basis of their optical thickness and hence their radiative properties.

The model evaluation is carried out by comparing the ECHAM5-subgrid version with the ISCCP satellite observations for global average  $\tau$ - $p_{\text{top}}$  joint histograms (shown in figure 3.2). The global land area shows that the model overestimates the high cloud cover for optically thin clouds (figure 3.2(c)) compared to observations

(figure 3.2(a)). The model misses the range of medium thick mid-level clouds ( $p_{\text{top}}$  between 680 and 400 hPa, and  $\tau$  between 3.6 and 23) over the land as well as over sea area. The low clouds over sea are underestimated by the model. Moreover, the ISCCP simulator diagnoses thicker low-level clouds (figure 3.2(d)) in comparison to the observations (figure 3.2(b)). The quantitative comparison of the cloud cover quantities for the ISCCP observations together with the ECHAM5-subgrid ISCCP simulator version are listed in table 3.2.

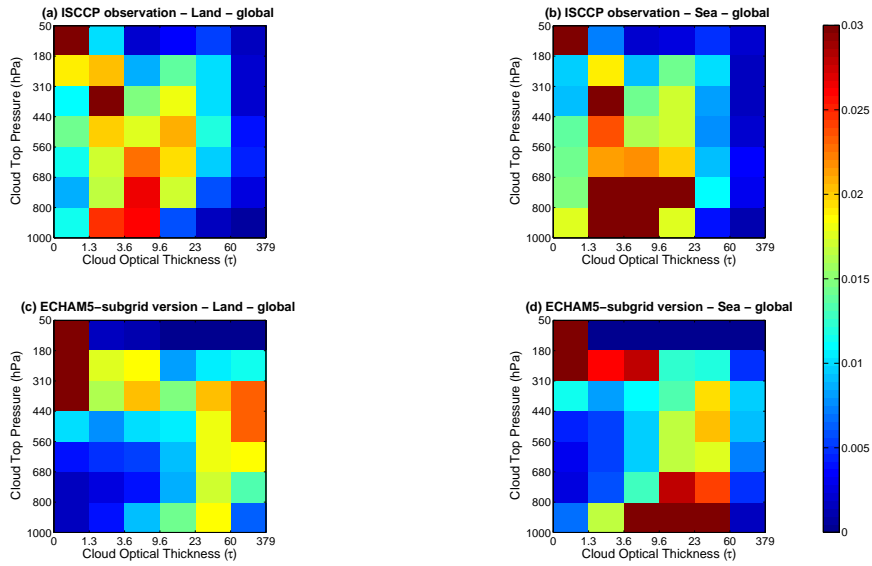


**Figure 3.2**— Comparison of average ISCCP histograms for global land and global sea area computed for ECHAM5-subgrid version model and for ISCCP observations (JJA 2002). The colorbar represents the distribution of cloud fraction in the  $\tau$ - $p_{\text{top}}$  joint histograms.

Model or observation type	ISCCP cloud fraction from histogram				
	TCC	HCC	MCC	LCC	DCC
ISCCP land	57.6	25.6	17.3	14.7	3.0
ECHAM5-subgrid land	55.7	31.5	13.9	10.5	6.5
ISCCP sea	66.6	21.4	17.1	28.0	2.8
ECHAM5-subgrid sea	67.3	28.8	12.4	26.0	4.6

**Table 3.2**— Mean cloud cover fraction of global land and global sea ISCCP cloud cover for ISCCP satellite observations and ECHAM5-subgrid ISCCP simulator version (JJA 2002). The respective cloud fraction values for TCC, HCC, MCC and LCC are shown in percent.

As shown in table 3.2, the overall difference between the total cloud cover fractions of ISCCP observations and those diagnosed by ISCCP simulator are very low ( $\sim 1$  to 2%). The land area shows an overestimation of high cloud cover ( $\sim 1.5$  times the observation cloud fraction). As shown in section 3.2, the high cloud cover over-

estimation of the high cloud cover in the model has a largest contribution from the high, optically thin clouds diagnosed in the model. The deep-convective clouds in the ECHAM5 also show overestimation with more than  $\sim 2$  times the observation cloud amount. The mid-level clouds are underestimated by the ECHAM5 model by  $\sim 3\%$ . The oceanic low clouds are relatively well simulated by the model with observational bias of  $\sim 2\%$ . However, the low clouds over ocean are underestimated by the model, which may be attributed to the boundary layer shallow convection process parameterization in the ECHAM5 model.

### 3.5 Cloud regimes and their climate change response

The radiative feedback from clouds remains the largest source of variation in climate sensitivity amongst general circulation models (Randall et al., 2007) and many model inter-comparison studies have been carried out to evaluate the simulated clouds and their changing effects in the future climate. By analyzing the GCMs in the context of cloud regimes, processes related to particular cloud types are more likely to be evaluated (Williams & Tselioudis, 2007). Using the cloud regime categorization, the model deficiencies can be attributed to parameterization related to individual cloud types and their specific behavior. As detailed in Jakob & Tselioudis (2003), various previous studies indicate that the average cloudiness observed in a given region is composed of a limited number of distinct cloud regimes, rather than consisting of a mixture of random cloud fields. Each of these distinct cloud regimes are linked to certain characteristics of the atmosphere. Analysis of the properties of the present day global cloud regimes and the cloud response to climate change in the cloud-regime framework is an interesting aspect of climate model evaluation.

Based on the work of Williams & Webb (2009), the clustering technique for defining various cloud regimes within the ECHAM5 model is applied in this work. The improved  $\tau - p_{\text{top}}$  histogram diagnostics by the sub-column generator version of ISCCP simulator (ECHAM5-subgrid) is used for assigning the model data to the ISCCP observational cloud regimes by Williams & Webb (2009). We also compute the climate change response of the regime RFO (relative frequency of occurrence) and CRF (cloud radiative forcing) in the perturbed simulations for idealized 2 degrees SST warming. The findings are compared with those of Williams & Webb (2009). A main idea following this approach is to characterize and compare the ECHAM5 model behavior to previous model inter-comparison studies. The following subsections comprise of a brief review of the clustering algorithm and the ECHAM5-ISCCP simulator output application results.

#### 3.5.1 Clustering technique for definition of cloud regimes

The clustering technique for defining cloud regimes is based on an iterative algorithm which searches for the possible *clusters* in a data set by evaluating a measure of distance between its individual data points. In this case a data point is defined by

an individual  $\tau - p_{\text{top}}$  histogram forming a vector of ISCCP cloud categories. The individual  $\tau - p_{\text{top}}$  histogram may be derived from satellite retrievals or from an ISCCP simulator within a general circulation model. Each grid-point at each time is treated as an independent data entry which form the basis of the analysis.

The clustering technique for cloud regime classification has been used in several previous studies. Jakob & Tselioudis (2003) obtain observational cloud clusters from the ISCCP retrieved  $\tau - p_{\text{top}}$  histograms for identification of cloud regimes at 3 selected sites in the Tropical Warm Pool (TWP) area. They use the ISCCP D1 data set providing joint histograms of the relative frequency of occurrence (RFO) of clouds with a certain  $\tau$  and  $p_{\text{top}}$  in grid boxes of  $\sim 280 \times 280$  km<sup>2</sup>. They apply the K-MEANS clustering algorithm (Anderberg, 1973) to the spatio-temporal set of 42 element vectors of ISCCP data histograms. These histograms represent the 2-dimensional element vectors in the form of cloud amount in 6 categories of  $\tau$  and 7 categories of  $p_{\text{top}}$  (for e.g.,  $C_{\tau_1, p_{\text{top}1}}, C_{\tau_1, p_{\text{top}2}}, \dots, C_{\tau_1, p_{\text{top}7}}, C_{\tau_2, p_{\text{top}1}}, \dots, C_{\tau_2, p_{\text{top}7}}, \dots, C_{\tau_6, p_{\text{top}1}}, \dots, C_{\tau_6, p_{\text{top}7}}$ ; where  $C$  is the cloud fraction in each bin of  $\tau$  and  $p_{\text{top}}$ ). These 42 elements are treated as being orthogonal to each other. The algorithm iteratively searches for an optimum set of a predefined number ( $K$ ) of cluster centroids. Each cluster centroid represents a specific histogram pattern. The algorithm iterates by assigning each individual  $\tau - p_{\text{top}}$  histogram to the cluster with the nearest centroid measured by an Euclidian distance (i.e., the minimum root-sum-square distance) of similarity. Hence, each histogram is assigned to the cluster whose centroid histogram pattern is most similar to it. The initial  $K$  cluster centroids are selected at random in the study by Jakob & Tselioudis (2003). After all histograms are assigned to one of the clusters, new centroids are determined and used as the new seed points for re-calculating the Euclidian distances. The method works iteratively in order to produce the optimum set of resulting cluster centroids. The optimum cluster set is obtained when the sum of all the distances between individual histograms and the centroids is minimum.

Ten iterations were found to be sufficient to ensure convergence in the optimum cluster iteration (Jakob & Tselioudis, 2003). The mean histogram for each cluster centroid (or identified cloud regime) is computed together with the number of cases within each cluster. The number of cases that occur within a particular cluster centroid are used to compute the relative frequency of occurrence (RFO) of the identified cluster. Four major cloud regimes, namely a shallow cumulus regime, a transparent isolated cirrus regime, thick cirrus with convection and a deep-convective regime are identified in the study over the TWP area by Jakob & Tselioudis (2003).

Another study based on the clustering technique for tropical belt of  $\pm 15^\circ$  latitude was by Rossow et al. (2005). Using satellite data, Rossow et al. (2005) identify 6 distinct *weather states* for the three-hourly ISCCP data for a time period of 21.5 years. These weather states were classified ranging from most convectively active to least convectively active. The changes in frequency of occurrence of these weather state patterns were used for describing the variation of the tropical climate on longer time scales ( $\sim 21$  years). The iterative algorithm needed to fulfill the criteria explained in Rossow et al. (2005). However, the clustering algorithm used by Rossow et al.

(2005) was different from that used by Jakob & Tselioudis (2003) for initial cluster selection. The most suitable number of clusters was determined objectively by repeating the analysis for an increasing number of clusters instead of selecting it at random like Jakob & Tselioudis (2003).

Following the same approach that Jakob & Tselioudis (2003) applied for ISCCP satellite observation data, Williams & Tselioudis (2007) extended the use of the clustering technique to classify cloud regimes simulated within a general circulation model. Williams & Tselioudis (2007) used the ISCCP simulator (Klein & Jacob, 1999; Webb et al., 2001) implemented in 6 GCMs for evaluating the different cloud related processes in equilibrium control (present day) climate and  $2\times\text{CO}_2$  atmosphere mixed layer ocean experiments. The daily averaged ISCCP simulator data for the 6 global models was submitted to the Cloud Feedback Model Inter-comparison Project (CFMIP). The approach is valuable for identifying the natural cloud clusters/regimes which occur in a GCM and how those evolve in a climate change simulation. However, since each GCM experiment can have a different number of clusters, Williams & Tselioudis (2007) had to combine some of the clusters into so called *principal cloud regimes* in order to compare the GCMs with each other and with the observations. This requires subjective judgement which, together with the subjective decisions remaining within the clustering procedure to define the number of clusters, makes the method difficult to automatize and for others to apply. This subjectivity is reduced by using the alternative approach presented by Williams & Webb (2009), which is also used in this work.

### **Application of cluster analysis in current work**

Williams & Webb (2009) assign the GCM simulated histograms to the observed ISCCP cloud regimes. This has the advantage for comparison purposes that there is a common number of regimes which can be directly compared and, once the observed regimes have been defined, there are no subjective decisions in the methodology. Instead of using the 42 element vector of cloud amount in each  $\tau - p_{\text{top}}$  bin, Williams & Webb (2009) use the grid-box mean values of cloud albedo or reflectivity ( $\alpha$ ), the cloud top pressure and the total cloud cover (TCC) in fraction (Gordon et al., 2005). The clusters of grid-box  $\alpha$ ,  $p_{\text{top}}$  and TCC for observations are compared with those of model and the respective frequency of occurrence for defined observational cloud regimes in a GCM are computed.

The grid-box mean  $\alpha$ ,  $p_{\text{top}}$  and TCC are normalized to be in the range 0 to 1 each (i.e., the  $p_{\text{top}}$  in hPa is divided by reference pressure of 1,000 hPa). Thus, a three element vector of  $\alpha$ ,  $p_{\text{top}}$  and TCC is created for ISCCP observations. This approach assumes that an error of 10% in  $\alpha$  is treated equally to an error of 100 hPa in  $p_{\text{top}}$  or an error of 10% in TCC, and so allows for some variation between the simulated and observed  $\tau$  and  $p_{\text{top}}$  of each regime.

The ISCCP simulator (ECHAM5-subgrid version) in the current work has output of  $p_{\text{top}}$ ,  $\alpha$  and TCC directly from the simulator diagnostics. Having a vector of 3 variables rather than 42 element histogram for the assignment also reduces

the amount of high temporal resolution data required proportionally, making the approach more attractive for application to large ensembles (e.g., Murphy et al., 2004). One prior concern regarding the method is that when a regime contains a mix of high and low top clouds, the mean  $p_{\text{top}}$  will be at mid-levels and may result in a similar vector to a regime with mid-level cloud tops. In practice,  $\alpha$  and TCC are different enough between these regimes that this does not happen (Williams & Webb, 2009).

Following Williams & Tselioudis (2007) and Williams & Webb (2009), the global data is divided into three major regions: the tropics (defined as 20° N to 20° S), the ice-free extra tropics, and regions covered by snow and ice in the equilibrium control climate simulation runs. This separation is required in order to split tropical deep-convective clouds from extra-tropical frontal clouds which both have similar  $\tau - p_{\text{top}}$  histograms but may differ in their climate change response. Another reason to separate the boundaries is to separate regions which may have a large change in surface albedo which can affect the CRF (Cess et al., 1990). The boundary between the ice-covered and ice-free extra-tropics is allowed to vary spatio-temporally. For the observational clusters, Williams & Webb (2009) obtain the ice edge from the ISCCP-IS product (Rossow et al., 1996). For ECHAM5-subgrid ISCCP simulator, the snow boundary is determined from the standard model output fields.

Daily mean model ISCCP simulator output for  $p_{\text{top}}$ ,  $\alpha$  and TCC are computed for 1 year (i.e., year 2002) from the ECHAM5 model. The clustering analysis is performed by assigning the normalized values of model  $p_{\text{top}}$ ,  $\alpha$  and TCC to the observational values of  $p_{\text{top}}$ ,  $\alpha$  and TCC (computed by Williams & Webb, 2009) with the minimum Euclidian distance of similarity. The RFO for the model clusters is computed by the number of grid-boxes nearest to the observational clusters. Individual regime RFOs are computed with respect to the global area separation of tropics, ice-free extratropics and snow/ice covered extratropics.

Table 3.3 shows the values of mean  $\alpha$ ,  $p_{\text{top}}$  and TCC for each observational regime defined by Williams & Webb (2009). This table provides the 3 element observational vectors (columns 2 to 4 in table 3.3) which the model data are assigned to. Williams & Webb (2009) computed the relative frequency of occurrence of the observational data for each region with respect to the defined regimes which are listed in column 5 of table 3.3. These observation regimes are listed in order of decreasing RFO in each region, which means that the cloud regime occurring most often in a region is listed first and the one occurring too infrequent is listed last for the observational analysis.

The cloud regime RFOs computed using the ISCCP simulator for ECHAM5 model (column 6, table 3.3) are listed for each region. For the tropics, the shallow cumulus dominate with 23.3%. This is qualitatively in agreement with the satellite observations (i.e., ISCCP clusters), despite a strong underestimation in quantitative terms. Thin cirrus are found to be next most abundant cloud type in the model (21%) which are third-most frequent tropical cloud regime in the observations (11.9%). This finding is consistent with the global histogram analysis in section 3.4,

Cloud Regime	$\alpha$ (%)	$p_{\text{top}}$ (hPa)	TCC (%)	RFO(%) ISCCP(WW09)	RFO (%)
<b>Tropics</b>					
Shallow cumulus	26.1	652	31.4	37.5	23.2
Congestus	33.9	483	81.3	19.5	5.18
Thin cirrus	21.1	356	74.0	11.9	21.1
Stratocu./cumulus transition	33.8	784	64.0	10.3	11.2
Anvil cirrus	31.3	327	94.4	9.1	18.5
Deep-convection	53.2	285	97.9	6.4	13.9
Stratocumulus	44.6	722	82.4	5.2	6.6
<b>Ice-free extra-tropics</b>					
Shallow cumulus	28.6	643	47.3	35.4	28.2
Congestus	45.7	607	93.2	17.0	12.3
Stratocu./cumulus transition	37.5	799	80.2	11.4	11.6
Cirrus	32.5	430	91.4	10.4	6.5
Stratocumulus	43.8	723	90.0	9.1	18.8
Frontal	58.1	393	97.8	8.3	13.5
Thin cirrus	22.0	389	71.3	8.3	8.4
<b>Snow or ice-covered</b>					
Shallow cumulus	43.3	582	31.4	42.3	18.6
Stratocumulus	51.0	740	31.4	19.1	19.6
Thick mid-level	57.6	620	31.4	13.9	3.3
Frontal	50.5	458	31.4	11.1	6.5
Thin mid-level	34.3	595	31.4	9.4	28.9
Thin cirrus	24.7	452	31.4	4.2	23.8

**Table 3.3**— Mean  $\alpha$ ,  $p_{\text{top}}$  and TCC for each ISCCP observation regime cluster. Relative frequency of occurrence for observational data are computed by Williams & Webb (2009) (WW09). Last column shows the RFO of observational regimes in the ECHAM5 model.

where thin high clouds prevail in the model derived histograms in the summer season. The anvil cirrus which are thicker (comparable to cirrostratus clouds in standard ISCCP cloud classification in figure 2.2) comprise almost 19% of the model data in tropical region. In the observations, congestus clouds with lower cloud tops are found  $\sim$ 19% of the time indicating that the model places clouds too high in the atmosphere (or congestus are replaced by thick cirrus clouds in the model). The model also comprises of a relatively large amount of deep-convective clouds (13.9%) compared to the observational RFO (6.4%).

The model cluster RFOs in comparison to the observation RFOs suggest that the ECHAM5 model diagnoses too little shallow cumulus clouds (23% in model compared to 37% in ISCCP observations). The congestus cloud regime for the

tropics is largely underestimated by the model (5.1%) compared to the observational data (19.5%). Moreover, the high clouds in the model (thin cirrus, anvil cirrus and deep-convective clouds) are overestimated in comparison to the observations. This behavior suggests that the model convection parameterization does not allow the clouds to detrain at the mid-levels (hence too little congestus), but rather the clouds move towards upper level to form more deep-convection and eventually detraining to form anvil cirrus clouds which gradually thin-out to form cirrus (see section 5.3 for a more detailed analysis of the anvil cirrus life-cycle). For the tropical areas, the ECHAM5 diagnoses the stratocumulus cloud regime and the transition regime of stratocumulus and cumulus clouds fairly well in comparison to the observations (differences in respective RFOs is less than 1% in both of these cloud regimes).

The ECHAM5 model behavior in the ice-free extratropics is very similar in cloud regime cluster RFOs compared to the observations, except for overestimation of the stratocumulus and the frontal cloud regime. The ice-free extratropics show an abundance of shallow cumulus clouds (28%) in the model similar to the observational cloud regime (35.4%). The extra-tropical frontal cloud regime (comparable to deep-convective clouds in the tropics) is overestimated by the model (18%) compared to observation cluster RFO of 9%. This behavior agrees with the findings of Williams & Webb (2009) where they conclude that ECHAM5 simulates the frontal regime more frequently and with a higher cloud top than ISCCP observations or any of the other CFMIP GCMs. The frontal cloud regime RFO is reported as  $\sim 45\%$  in the study by Williams & Webb (2009), whereas the present analysis shows that the RFO for extra-tropical frontal clouds is 13.5% (which is still higher compared to 8.3% in the observational clusters). This excess appears to be due to high, optically thick clouds persisting in this model after meteorological conditions associated with frontal clouds have ceased. ECHAM5 shows a higher amount of stratocumulus clouds (18.6%) when compared to observations (9.1%). The overestimation of the optically thicker stratocumulus compensates the lack of optically thinner shallow cumulus clouds in the model clusters. This overestimation of stratocumulus clouds may be related to the incorrect representation of shallow convection triggering within the convection parameterization scheme in the ECHAM5. The cloud regime categories of stratocumulus/cumulus transition, and thin cirrus are pretty well simulated in the model with a difference of less than 1% in model and ISCCP observation RFOs. Cirrus and congestus cloud regimes are relatively underestimated in the model with the lack of these clouds compensated by too many frontal clouds which are optically thicker but similar in  $p_{\text{top}}$  and total cloud fraction. It is important to note that Williams & Webb (2009) discuss about the uncertainty of the exact definition of the congestus cloud category regime in their study. Within the ice-free extra tropical regions, the behavior of the ECHAM5 model is more consistent to observations compared to the tropical regions. The influence of large scale processes are one of the factors in the cloud regimes derived in extra-tropics where individual events (for example, convection triggering) are forced by the large scale circulation processes within the model.

For the snow or ice covered region, the cluster analysis shows that the model

computed cloud regimes for thin mid-level and thin cirrus clouds dominate the RFO (28% and 24% respectively). These regimes are the ones with least RFO in the observational clusters of ISCCP by Williams & Webb (2009). Shallow cumulus clouds are less frequent in the model (18%) than in observations (42%, most abundant cloud regime in observations). Similarly, the thick mid-level clouds and frontal clouds that are also underestimated by the ECHAM5 model. The stratocumulus cloud regime RFO is 19% within the model which agrees well with the ISCCP observation cluster RFOs. Ice-covered extra-tropical regions show a weaker regime for frontal clouds in comparison to the ice-free extratropical regions, however, the thin cirrus clouds are abundant in this region (23.8% compared to 8% in ice-free extratropics). The mid-level clouds in the extratropics have a greater RFO for thin clouds (23% compared to 4% ISCCP observations), and a smaller RFO for thick clouds (3% in model compared to 13% in observations). This behavior may be attributed to the abundance of drizzling clouds in the model which reduce the cloud optical thickness and hence the clouds are detected too thin in the ISCCP simulator.

### 3.5.2 Climate change response

Cloud feedbacks in response to climate change from the ECHAM5 model is computed by using the model firstly in a control model (present day climate), and with an idealized warming effect with an SST perturbation of +2 K. The cluster analysis methodology (explained in previous section) is repeated with the model simulations forced with perturbed SST (warmer climate). The ECHAM5-subgrid version of ISCCP simulator is used for all the simulations, which were run for 1 year. Since cloud processes react fast, a relatively short integration time is sufficient. The respective cloud regime RFOs for tropical, ice-free extratropics, and ice/snow covered extratropics are computed for the perturbed climate run. The change in cloud regime RFO within the perturbed and the present day climate is termed as  $\Delta\text{RFO}$ . Hence,

$$\Delta\text{RFO} = \text{RFO}_{\text{perturbed}} - \text{RFO}_{\text{present}} \quad (3.1)$$

The regime mean CRF components for the climate change response are obtained by averaging the daily mean shortwave cloud radiative forcing (SCRF), longwave cloud radiative forcing (LCRF) and the resultant net cloud radiative forcing (NCRF) from the grid-points assigned to each regime. The change in NCRF of from present day to perturbed climate is termed as  $\Delta\text{NCRF}$ , expressed as

$$\Delta\text{NCRF} = \text{NCRF}_{\text{perturbed}} - \text{NCRF}_{\text{present}} \quad (3.2)$$

Table 3.4 shows the values of NCRF in  $\text{Wm}^{-2}$  for the ECHAM5 model present day run, NCRF for +2 K perturbed SST run,  $\Delta\text{NCRF}$  computed by equation 3.2 and  $\Delta\text{RFO}$  computed by equation 3.1 for each cloud regime for tropics, ice-free extratropics and ice/snow covered extratropics areas. For the tropical areas, the congestus clouds are found out to be the only regime with a negative  $\Delta\text{NCRF}$ . The high cloud regimes (cirrus and extratropical frontal clouds) show a negative net

Cloud Regime	NCRF(Wm <sup>-2</sup> ) Clim SST	NCRF(Wm <sup>-2</sup> ) +2 K SST	ΔNCRF (Wm <sup>-2</sup> )	ΔRFO (%)
<b>Tropics</b>				
Shallow cumulus	-2.6	-2.2	0.4	1.5
Congestus	-23.1	-24.4	-1.3	-0.6
Thin cirrus	4.3	4.7	0.4	1.6
Stratocu./cu.	-26.0	-24.9	1.1	-1.1
Transition				
Anvil cirrus	9.9	11.7	1.6	-0.6
Deep-convection	-48.5	-47.9	0.6	0.1
Stratocumulus	-72.8	-71.8	1.0	-1.2
<b>Ice-free extra-tropics</b>				
Shallow cumulus	-11.0	-10.9	0.1	0.8
Congestus	-43.5	-43.2	0.3	-0.4
Stratocu./cu.	-66.7	-66.5	0.2	-1.3
transition				
Cirrus	-37.6	-38.5	-0.9	0.1
Stratocumulus	0.1	1.8	1.7	-0.9
Frontal	-60.1	-61.2	-1.1	1.5
Thin cirrus	3.4	4.0	0.6	1.3
<b>Snow or ice-covered</b>				
Shallow cumulus	-9.3	-9.1	0.2	-0.2
Stratocumulus	-5.6	-5.2	0.4	0.2
Thick mid-level	-3.6	-2.6	1.0	1.0
Frontal	23.0	22.7	-0.3	1.8
Thin mid-level	6.4	7.2	0.8	-3.4
Thin cirrus	1.5	2.1	0.6	-0.4

**Table 3.4**— Regime mean net cloud radiative forcing for present day climatological SST and +2 K perturbed SST, Δ NCRF (perturbed minus present day) and Δ RFO (perturbed minus present day).

cloud forcing for the ice-free extratropical areas in our analysis.

Following Williams & Tselioudis (2007) and Williams & Webb (2009), the change in the mean area net cloud radiative forcing ( $\overline{\Delta\text{NCRF}}$ ) is expressed as

$$\begin{aligned}
 \overline{\Delta\text{NCRF}} &= \sum_{r=1}^{\text{nregimes}} \text{NCRF}_r \Delta\text{RFO}_r + \sum_{r=1}^{\text{nregimes}} \text{RFO}_r \Delta\text{NCRF}_r \\
 &+ \sum_{r=1}^{\text{nregimes}} \Delta\text{RFO}_r \Delta\text{NCRF}_r
 \end{aligned} \tag{3.3}$$

where the first term on the right-hand-side of equation 3.3 represents the contribution to  $\overline{\Delta\text{NCRF}}$  from the change in the RFO of the regime ( $r$ ). This term is called as the  $\Delta\text{RFO}$  driven component of the forcing. The second term represents the change in NCRF within the regime  $r$ , called the  $\overline{\Delta\text{NCRF}}$  driven component. The third term reflects a covariation of RFO and NCRF for which our results confirm that it is of second-order importance. Table 3.5 shows the quantitative values for the components of the climate change response in equation 3.3.

For the Tropics, the total response to SST perturbation is a positive  $\overline{\Delta\text{NCRF}}$  for all the cloud regimes (table 3.5, column 4). This appears to be primarily a result of a positive change in the  $\Delta\text{NCRF}$  of the cloud regimes, rather than a net change in the RFO of the regimes. ECHAM5 simulates a reduction in  $\Delta\text{NCRF}$  for the congestus cloud regime, however the radiative response tends to approximately cancel on the large scale due to negative  $\Delta\text{RFO}$  for the same. The largest contributors to the overall  $\overline{\Delta\text{NCRF}}$  is the  $\text{NCRF}*\Delta\text{RFO}$  component for the stratocumulus clouds and the stratocumulus/cumulus transitions which arise due to stronger net forcing for these clouds in the tropics and a respective negative RFO in the warmer climate. The largest component for  $\Delta\text{RFO}$  occurs in the shallow cumulus cloud regime (the most frequent cloud regime in the tropics for the observations as well as the model), but the overall  $\overline{\Delta\text{NCRF}}$  remains smaller in the climate response due to a weak  $\Delta\text{NCRF}$  for shallow clouds.

As in the tropics, most of the difference in the  $\overline{\Delta\text{NCRF}}$  for the ice-free extra-tropics arises from different changes in the radiative characteristics of the regimes. ECHAM5 shows a relatively large negative  $\Delta\text{NCRF}$  for frontal clouds leading to a large  $\text{RFO}*\Delta\text{NCRF}$  component in  $\overline{\Delta\text{NCRF}}$ . On the other hand, the stratocumulus and the stratocumulus/cumulus transition cloud regimes show a positive  $\Delta\text{NCRF}$  leading to a large positive  $\text{RFO}*\Delta\text{NCRF}$ , and hence compensating the overall net radiative forcing for the extra-tropics.

The  $\overline{\Delta\text{NCRF}}$  over snow or ice covered extra-tropical regions is largest for frontal clouds in the ECHAM5 model which is due to a large positive RFO component which leads to a larger  $\text{NCRF}*\Delta\text{RFO}$  component. The overall response is dominated by changes in the  $\text{NCRF}*\Delta\text{RFO}$  component for frontal clouds. The thin mid-level clouds show a large positive  $\text{NCRF}*\Delta\text{RFO}$  component, which is however canceled due to a large negative  $\text{RFO}*\Delta\text{NCRF}$  component for the  $\overline{\Delta\text{NCRF}}$ . Similar to the tropics and ice-free extra-tropics, the covariance term of  $\Delta\text{RFO}*\Delta\text{NCRF}$  is always small ( $\sim 1$  to  $2 \text{ \%Wm}^2$ ) for all the cloud regimes.

### 3.6 Summary and conclusions

The comparison of global average cloud quantities are evaluated in this chapter in comparison to ISCCP satellite observations. The ECHAM5 ISCCP simulator diagnostics reveal that the oceanic low clouds (shallow cumulus and stratocumulus clouds) are underestimated by  $\sim 40\%$  in comparison to the observations. Moreover these low clouds are optically too thick in comparison to the ISCCP observations for

Cloud Regime	$\text{NCRF}*\Delta\text{RFO}$ ( $\text{Wm}^{-2}$ )	$\Delta\text{NCRF}*\text{RFO}$ ( $\text{Wm}^{-2}$ )	$\Delta\text{NCRF}*\Delta\text{RFO}$ ( $\text{Wm}^{-2}$ )	$\overline{\Delta\text{NCRF}}$ ( $\text{Wm}^{-2}$ )
<b>Tropics</b>				
Shallow cumulus	-0.039	0.092	0.0060	0.059
Congestus	0.13	-0.067	0.0078	0.079
Thin cirrus	0.068	0.084	0.0064	0.15
Stratocu./Cu.	0.28	0.12	-0.012	0.39
Transition				
Anvil cirrus	-0.059	0.29	-0.0096	0.22
Deep-convection	-0.048	0.083	0.0006	0.035
Stratocumulus	0.87	0.066	-0.012	0.92
Total tropical	1.22	0.67	-0.012	1.88
<b>Ice-free extra-tropics</b>				
Shallow cumulus	-0.08	0.028	0.0008	-0.059
Congestus	0.17	0.036	-0.0012	0.20
Stratocu./cu.	0.86	0.023	-0.0026	0.88
Transition				
Cirrus	-0.037	-0.058	-0.0009	-0.097
Stratocumulus	-0.0009	0.31	-0.015	0.30
Frontal	-0.90	-0.14	-0.016	-1.06
Thin cirrus	0.044	0.050	0.0078	0.10
Total ice-free ex- tratropical	0.057	0.25	-0.027	0.28
<b>Snow or ice-covered</b>				
Shallow cumulus	0.018	0.037	-0.0004	0.055
Stratocumulus	-0.011	0.078	0.0008	0.068
Thick mid-level	-0.036	0.033	0.010	0.0070
Frontal	0.41	-0.019	-0.0054	0.38
Thin mid-level	-0.21	0.23	-0.027	-0.013
Thin cirrus	-0.0060	0.14	-0.0024	0.13
Total ice-covered extratropical	0.16	0.50	-0.024	0.64

**Table 3.5**— Components of  $\overline{\Delta\text{NCRF}}$  computed from each cloud regime. The total effect of each regime for  $\overline{\Delta\text{NCRF}}$  is computed for tropics, ice-free extratropics and snow or ice covered extratropics based on equation 3.3.

the global average sea areas. The inadequate representation of shallow convection within the convection parameterization scheme in the model is a likely reason for the underestimation of these boundary layer clouds.

The mid-level clouds are underestimated ( $\sim 10\%$  to  $20\%$ ) by the model compared

to the ISCCP observations. The clouds originating from convection in the model do not detrain at mid-levels but rather are transported further up to form more high clouds. The global cloud distribution maps reveal that the model overestimates the high cloud cover in the tropical ITCZ belt. The analysis of global ISCCP histograms show that too many of these high cloud diagnosed by the model lie in the optical thickness range of 0 to 1.3 (thin cirrus) for global average land as well as sea areas.

The sensitivity of ISCCP simulator versions for ECHAM5-basic and ECHAM5-subgrid are analyzed in order to compare the diagnostic differences. The sensitivity studies reveal that the cloud diagnostics is sensitive to the simulator version, and the ECHAM5-subgrid version provides a realistic distribution of cloud types in the ISCCP histograms in comparison to ISCCP-basic version. The generated sub-columns in the ECHAM5-subgrid version use the horizontal variability via probability density function of total water (Tompkins, 2002) and hence provides an improved statistics for simulator diagnostic.

The clustering technique based on the work of Williams & Webb (2009) for identification and evaluation of various cloud regimes as simulated by ECHAM5 model is performed. An objective identification of cloud regimes, in principle, provides a strategy for examining properties of these cloud regimes and, perhaps, the key processes that establish them (Stephens, 2005). Three principal areas namely the tropics, the ice-free extratropics and the snow-covered extratropics are distinguished in the global model output. Each grid-point of the ISCCP simulator model output is assigned to observed ISCCP cloud clusters defined by Williams & Webb (2009) for computation of the regime mean relative frequency of occurrence (RFO) and net cloud radiative forcing (NCRF).

For the tropics and the ice-free extratropics, the cluster analysis shows that the ECHAM5 model simulates the shallow cumulus clouds as the most frequent cloud regime with maximum RFO with qualitative agreement to the ISCCP observations. Similar to the findings of Williams & Tselioudis (2007) and Williams & Webb (2009), optically thick, high top cloud in the extra-tropics, typically associated with the passage of frontal systems, is simulated considerably too frequently in the ECHAM5 model compared to ISCCP observations or any of the other CFMIP GCMs. The frontal cloud regime RFO is reported as  $\sim 45\%$  in the study by Williams & Webb (2009), whereas the present analysis shows that the RFO for extra-tropical frontal clouds is 13.5% (which is still higher compared to 8.3% in the observational clusters). Williams & Webb (2009) report that the CFMIP comparison models share a difficulty in simulating the regimes with cloud tops at mid-levels, with only ECHAM5 producing a regime of tropical cumulus congestus. However, our analysis suggests that the tropical congestus regime is captured in the ECHAM5 diagnostics but its RFO is underestimated compared to the observations. In comparison to the ISCCP observations, the snow or ice free extratropics show a lack of shallow clouds in the model which is compensated by an overestimation of thin cirrus and mid-level clouds.

The total climate change response of clouds to SST perturbation is positive

---

$\overline{(\Delta\text{NCRF})}$ , when measured by means of change in net cloud radiative forcing) for all the cloud regimes in the tropics. For the ice-free as well as ice-covered extratropics, the overall response is dominated by changes in the  $\Delta\text{NCRF}$ , rather than the  $\Delta\text{RFO}$  for the cloud regimes. The stratocumulus and stratocumulus/cumulus transition cloud regimes are responsible for 2/3 of the feedbacks with stratocumulus alone responsible for  $\sim 50\%$ . The tropics in turn dominate the global cloud-climate feedbacks.



## Chapter 4

# Evaluation of the diurnal cycle of clouds in ECHAM5 model

*This chapter is dedicated to the evaluation of ECHAM5 general circulation model for diurnal variations of simulated ISCCP clouds. The primary focus here is to analyze a selected number of test areas where the model derived diurnal cycle for land and sea regions is compared with the observations. The following sections detail the physical significance of diurnal analysis within a climate model and its evaluation for the ECHAM5 model. We use the ISCCP 3-hourly satellite observations to compare the amplitude and timing of the simulated diurnal cycle for different cloud categories in our selected test areas.*

### 4.1 Diurnal cycle of convection

The diurnal cycle of convection is represented here by the time variation of cloud fraction of convective or thick high clouds during a day. The diurnal variation of different cloud types gives a fair idea about the precipitation cycle during a day. Associated with well-defined, large, and external diurnal (i.e., 24 hour) variations of solar forcing, the diurnal cycle is one of the fundamental modes of variability of the global climate system. It provides a large and well-documented source of forcing with frequent sampling (Tian et al., 2004). Thus comparisons of the diurnal cycle between observations and a GCM represent a powerful tool for evaluating the GCM performance and identifying the deficiencies of the model (Slingo et al., 1987; Randall et al., 1991; Lin et al., 2000; Yang & Slingo, 2001; Betts & Jakob, 2002; Dai & Trenberth, 2004).

Large-scale atmospheric dynamic and radiative processes strongly affect the life cycle of deep-convective systems in the tropics. The observed diurnal variation of tropical cloud systems suggest that the diurnal heating of the tropical atmosphere provide favored conditions in the afternoon for the formation of cloud systems and, as the cloud systems grow and decay with time, the diurnal cycle of cloudiness reflects the life-cycle (initiation, growth, and dissipation) of the cloud systems (Chen

& Houze-Jr., 1997). The diurnal cycle of convection (i.e., deep-convective clouds) is particularly important in a model evaluation since convectively generated clouds strongly interact with both solar and thermal infrared radiative fluxes. This interaction however, is drastically different in the solar and terrestrial spectra. At night, these high thick clouds contribute to the greenhouse effect by efficiently trapping thermal infrared radiation, so that night-time surface temperature is warmer under cloudy conditions. During the day, the reflection of insolation generally dominates over the greenhouse effect, leading to an opposite effect on surface temperature. Therefore, it is necessary to predict correctly the time of day during which these clouds are present in order to get an accurate radiative budget, both at the top of the atmosphere and at the surface (Guichard et al., 2004). Clouds also strongly modulate the magnitude of surface heat fluxes (sensible plus latent heat) through their impact on the net radiative fluxes at the surface. Similarly, the magnitude of their impact on the surface heat flux also depends on the diurnal timing of clouds, because of the large daily variation of surface heat fluxes over land. Hence, a proper simulation of the actual diurnal cycle of convection is also required in order to capture its possible fluctuations in the context of climate sensitivities.

Moreover, the nature of the problem is not the same over the land and over the ocean. Over land, the diurnal cycle of deep-convection is strongly linked to daytime boundary-layer heating, whereas over the ocean the diurnal variations of the sea surface temperature (SST) and the boundary layer are much weaker (Guichard et al., 2004). The phase of the diurnal cycle as seen in previous studies (for e.g., Yang & Slingo, 2001) suggests that the mechanisms for the observed diurnal variation in convection over land and ocean are very different. The diurnal cycle of convection over land is basically a low-level thermodynamical response to the radiative heating cycle. During the day, solar heating over land surface increases the lower-tropospheric temperature (and moisture) and thus atmospheric instability, leading to development of convective cloud systems, the resulting convective precipitation maximum tending to occur in the evening. In contrast, radiative cooling of the land surface at night enhances the stability, suppressing convection and leading to a minimum in the early morning. Hence, a typical diurnal cycle over land has a maximum around afternoon and a minimum around early morning.

For oceanic deep-convection, which typically peaks in the early morning, the situation is much more complicated than a typical land diurnal variation, and there may be several mechanisms responsible for the behavior of this ocean diurnal cycle. The first mechanism stated in the literature involves a direct radiation-convection interaction (Randall et al., 1991). At night, infrared cooling at the cloud top is greater than at cloud base resulting in destabilization of the upper troposphere, leading to cloud development with a maximum occurring in the early morning; during the day, warming at cloud top due to solar absorption increases the stability and therefore restricts convective activity. The second possible mechanism involves the cloud versus cloud-free radiation difference in the horizontal (Gray & Jacobson, 1977). The radiative cooling of the cirrostratus at upper-tropospheric levels is greater than the radiative cooling in the surrounding less cloudy or clear sky regions,

whereas during the day the situation is reversed. This day-night differential heating cycle results in a daily variation in the horizontal divergence field that may give rise to a diurnal variation in convective activity. Liu & Moncrieff (1998) used an idealized two-dimensional cloud resolving model to simulate the diurnal variation of tropical oceanic deep-convection. The model gave a pre-dawn maximum and late afternoon minimum in convection intensity for highly organized as well as less organized convection. Liu & Moncrieff (1998) concluded that this diurnal variation was primarily controlled by the direct radiation - convection interaction; the cloud versus cloud-free radiation difference was of secondary importance.

However, several recent studies have shown that it is difficult for general-circulation models to capture the diurnal cycle of deep-convection, in terms of both magnitude and phase, over the land as well as over the ocean (Dai et al., 1999; Lin et al., 2000; Yang & Slingo, 2001; Betts & Jakob, 2002). All these studies detected a time lag in the diurnal cycle of deep-convection simulated by large-scale models, with convective rainfall occurring too early during daytime compared with the observations. For example, Dai (2006) evaluated the diurnal cycle in 18 GCMs using multiple observation data sets and suggested that the simulated diurnal cycle is too early in the precipitation peak and too strong in the amplitude than those observed even in the latest generation GCMs. A poor description of the diurnal cycle in the tropics in GCMs may be a matter of concern for predicting tropical climate variability (Wang et al., 2007). Therefore, considerable improvements are necessary for realistically simulating the diurnal cycle of precipitation by GCMs, although the diurnal cycle in the tropics is a predominantly local phenomenon. Conventional GCMs generally adopt cumulus parameterization to describe subgrid scale convection and, hence, have limitations in simulating the propagation of the diurnal cycle in which the mesoscale circulations play a significant role (Sato et al., 2009).

Observation of the diurnal cycle of convection is also quite challenging as its simulation in the climate model. Due to the paucity of surface-based observing sites in the tropics, space-based observations offer the only possibility of adequately detailing convective properties throughout the global tropics (Hendon & Woodberry, 1993). The very nature of convective activity, however, makes satellite observations a challenging proposition. Convection evolves on time scales less than a day and is organized on space scales of the order of  $\sim 100$  km. Although observations from a single polar-orbiting satellite have formed the basis for most climatological studies of the global convective field (for e.g., deep-convective clouds), these asymptotic measurements cannot faithfully resolve convective activity since they fly in sun synchronous orbit and are affected by diurnal cycle. These satellites sample only once or twice per day, which causes biases in their reported statistics on convective clouds because they may be consistently observing high or low points in these diurnal cycles. Because of this problem, the International Satellite Cloud Climatology Project (ISCCP) (Schiffer & Rossow, 1983; Rossow & Schiffer, 1991, 1999) used geostationary satellites gathering eight observations per day where these satellites were available. Hence, ISCCP provides a unique opportunity to investigate various properties of the diurnal cycle of convection, on a global basis for a long time series (i.e., year 1984 to

present). Due to this advantage of ISCCP over other polar-orbiting satellites or less homogeneous cloud data sets, we use the ISCCP cloud climatology as our primary choice of model verification data for diurnal cycle.

## 4.2 Case studies: Diurnal cycle variations in test areas

The diurnal cycle of radiative forcing ultimately causes diurnal variations in the cloudiness observed over the tropics. The diurnal variations of tropical deep-convection exhibit a wide range of regionally different behavior. The nature of these variations depends on the nature of underlying surfaces. Over land and near coastlines the thermal properties of the land surface and the land-sea-breeze circulation introduced by the contrast between the land and the ocean surfaces can explain much of the diurnal cycle of clouds and precipitation. Over the open ocean the thermal properties of the ocean surface and underlying atmospheric boundary layer undergo a diurnal variation that is relatively weak compared to that of the land surfaces.

In order to address the issue of diurnal cycle variability over the tropics, four regions are selected as test case areas for this work. Each test area is a box of  $30^\circ \times 30^\circ$ . Each area is further categorized as land region and sea region based on the land-sea mask. The diurnal cycles of ISCCP cloud types are computed separately for land and sea regions. Since the areas are tropical and we analyze the northern-hemisphere summer months, we expect to capture large amount of high and convective cloud cover. Moreover, the differentiation between the land and sea region is helpful in testing the robustness of the diurnal behavior based on large scale dynamics of these individual test areas.

The model data used in this analysis is the improved ISCCP simulator version (ECHAM5-subgrid) as described in section 2.3.2. Three-hourly model output is used at a resolution of T63L31 ( $\sim 1.8^\circ \times 1.8^\circ$ ), which is then converted to a seasonal average (June-July-August, or JJA) for the year 2004. The reason for selecting the year 2004 is to facilitate the use of MODIS Terra and Aqua observations. These observations served as a redundant dataset to compare the diurnal cycle of model output together with the ISCCP daytime observations. In order to attain a full diurnal cycle for 24 hours, we omit in the model the screening for sunlit scenes (hence, including also nighttime data in the model output). The three-hourly mean values of ISCCP-classified high, middle, low and total cloud cover magnitudes are computed for the JJA months. The deep-convective cloud cover, which is a subset of high cloud cover with optical thickness ( $\tau$ ) greater than 23 is also compared for its diurnal cycle with the ISCCP observations.

The ISCCP satellite observations are post processed in the same way as model output (3-hourly JJA, year 2004). The corresponding three hourly values of ISCCP cloud types are computed by the gridded ISCCP observational joint histogram data (level D2). The diurnal variation is represented by day-time cloud fraction values of various cloud categories. These discrete values are computed by averaging the cloud

fraction amount in the appropriate  $\tau$ - $p_{top}$  joint histogram bins (refer ISCCP cloud classification in figure 2.2). The spatial resolution of the used ISCCP observations is  $2.5^\circ \times 2.5^\circ$ , and thus comparable to the GCM resolution used here.

### Details of the test areas

The geographical details of the test areas are listed as the following, and figure 4.1 shows these areas on a global composite image from GOES and Meteosat satellites.

1. **Africa -  $00^\circ\text{S}$  to  $30^\circ\text{S}$  and  $00^\circ\text{E}$  to  $30^\circ\text{E}$**

This area extends from the equatorial south Atlantic ocean to the western boundary of Tanzania. The northern boundary of the African test area ranges from the northern coast of Gabon and extends up-to the southern African coastline near Capetown region.

2. **Amazon -  $00^\circ\text{S}$  to  $30^\circ\text{S}$  and  $25^\circ\text{W}$  to  $55^\circ\text{W}$**

The Amazon test region covers the Brazilian rainforests and extends up-to northern border of Argentina in its south. The western boundary of this region starts from the Manaus area in the Amazon basin and ranges till the middle of equatorial south Atlantic ocean as open sea area in the east.

3. **India -  $00^\circ\text{N}$  to  $30^\circ\text{N}$  and  $60^\circ\text{E}$  to  $90^\circ\text{E}$**

The Indian subcontinent test region is selected from the south of Himalayan basin (in order to avoid the influence from the orographic characteristics due to Himalayan geography) and continues till the southern Indian ocean around Maldives. The western boundary for this test region is chosen starting from the Afghanistan plateau and extending to the middle of Bangladesh at its eastern boundary.

4. **Indonesia -  $10^\circ\text{N}$  to  $20^\circ\text{S}$  and  $90^\circ\text{E}$  to  $120^\circ\text{E}$**

The Indonesian test area ranges from southern Cambodia to the north-western coast of Australia. The western boundary starts from the western Indonesian coast south of the Bay of Bengal and extends up-to the western boundaries of the Philippines.

The following sections detail the obtained results for the comparison of model simulated diurnal cycles with those of observations computed for each of the above test areas.

#### 4.2.1 Case study-1: African region

Figure 4.2 shows the diurnal cycle for a variety of ISCCP cloud types from the model simulations compared to the observations. Local standard time (LST) is

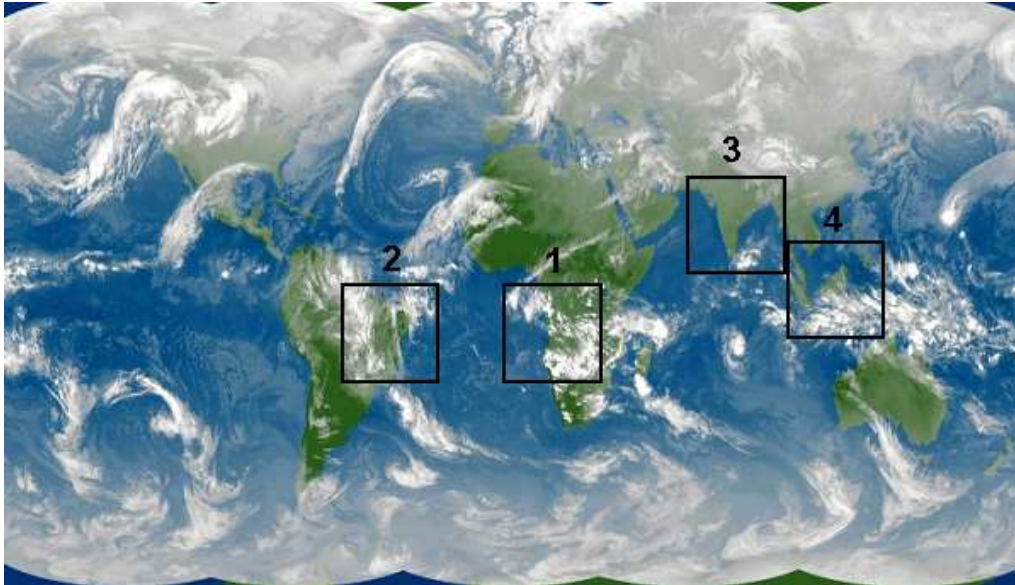


**Figure 4.1**— Geographical extents of the test study areas: 1. Africa; 2. Amazon; 3. India; 4. Indonesia. (Image source - <http://www.eumetsat.int/>).

shown on each subplot for which the average cloud fractions for ISCCP cloud types are computed. The solid lines in the subplots of figure 4.2 represent the model output whereas the dashed lines represent the ISCCP observations.

The solid black lines in figure 4.2 represent the total cloud cover (TCC) for model output in the land and sea areas, respectively. Similarly, the dashed black lines represent the ISCCP observations for TCC for the land and sea area respectively. The high cloud cover (HCC) is shown in blue and the deep-convective cloud cover (DCC) in pink colored lines. The results for the African land area are shown in figure 4.2(a), whereas figure 4.2(b) shows the same for the African sea area. Similarly figure 4.2(c) and 4.2(d) show the mid cloud cover (MCC) in red, and the low cloud cover (LCC) in green color for the African land and sea areas, respectively.

As seen from figure 4.2, the general behavior of the model compared to observations is that the model overestimates the high cloud cover and underestimates the mid and low cloud cover. Table 4.1 shows the quantitative values for the diurnally averaged ISCCP cloud types over land and over sea. This average is calculated for the model as well as the ISCCP observations. The total cloud cover for land area does not differ much from the observations ( $\sim 3\%$ ), but for the ocean area the mean values differ by  $\sim 9\%$ , with an underestimation of the total cloud amount. In case of the high cloud cover, the model overestimates the cloud amount compared to the observations for land ( $\sim 5\%$  overestimation, 1.5 times of the high cloud amount for observations) and ocean ( $\sim 6\%$  overestimation, 4 times of the observation cloud amount). An exactly opposite effect of the high cloud estimation can be seen in the model low cloud amount for the land area ( $\sim 6\%$  underestimation, 4 times less of the observation low cloud amount), and for the ocean area ( $\sim 11\%$  underestimation).

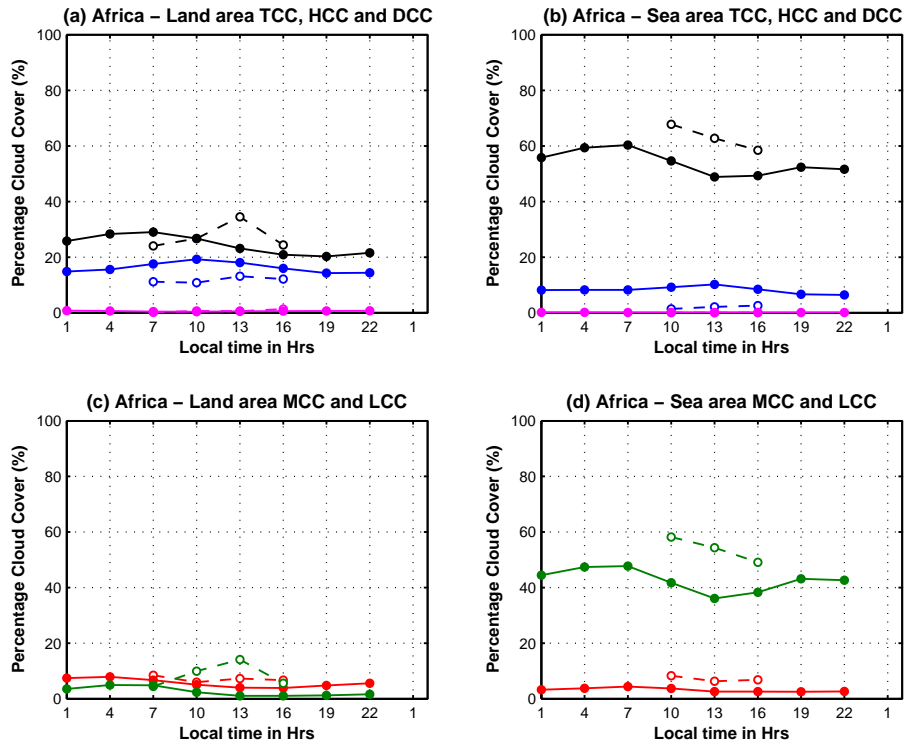


**Figure 4.2**— Diurnal cycle for land and sea: model results and ISCCP observations over the African region

--○--:ISCCP TCC; --○--:ISCCP HCC; --○--:ISCCP DCC; --○--:ISCCP MCC; --○--:ISCCP LCC;  
 ●—:Model TCC; ●—:Model HCC; ●—:Model DCC; ●—:Model MCC; ●—:Model LCC

The model mid-cloud amount is also underestimated when compared to the observations for land ( $\sim 2\%$  underestimation) and sea ( $\sim 4\%$  underestimation). Since the deep-convective cloud amount does not have a very large magnitude for the African region, the model and the observations show a similar value for land and ocean with a variation of less than  $\sim 0.1\%$ .

The amplitudes of the diurnal cycle for the land and the sea areas are listed in table 4.2. This computation is performed by subtracting the minimum value from the maximum value for the diurnal cycle for a particular cloud category. These differences are calculated separately for two conditions of timing in the model, i.e., all the time steps (24-hours), when observations exist (daylight or, 12-hours). The idea of separating these two components for diurnal cycle amplitude is to determine the behavior of the model in sunlit time or day-light time and for a 24-hour continuous period (with sunlit = 1 at all the times in the ISCCP simulator diagnostics). The ISCCP observational period is in the visible channel hence, only the sunlit time steps during the day. Compared to observations, the model amplitude for land area total cloud cover is relatively lower ( $\sim 10\%$  for observations and  $\sim 8\%$  for the model). On the other hand, the amplitude for sea area total cloud cover for the model changes

Cloud types	ISCCP cloud cover in %				
	Total cloud	High cloud	Mid cloud	Low cloud	Deep-conv. cloud
Africa model land	24.47	16.23	5.65	2.57	0.58
Africa ISCCP land	27.42	11.81	7.09	8.50	0.67
Africa model sea	54.04	8.18	3.16	42.69	0.10
Africa ISCCP sea	63.03	2.01	7.14	53.88	0.06

**Table 4.1**— Mean cloud cover values for model and ISCCP observations JJA 2004 - African region

based on the 24 hour time-steps ( $\sim 11\%$ ) or the day-light time-steps ( $\sim 6\%$ ). As listed in table 4.1, the amplitude values for the model land and sea are higher for high clouds, and relatively lower for low clouds when compared to observations.

Shown in figures 4.2(a) and (b), the model land TCC diurnal peak is too early (i.e., 07:00 LST) compared to the ISCCP observations (i.e., 13:00 LST), similar to the sea area where model TCC is maximum at 07:00 LST and the observational TCC is maximum at 10:00 LST. The diurnal peak for the high clouds in African region is earlier (i.e., 3 hours too early) for the model compared to the observations in land as well as sea region. For the mid and low cloud cover, the diurnal peak occurs 6 hours too early for the land and sea regions in the model in comparison to the ISCCP observations.

Cloud types	ISCCP cloud cover in %				
	Total cloud	High cloud	Mid cloud	Low cloud	Deep-conv. cloud
Model all time land	8.80	4.99	4.01	3.86	0.37
Model all time sea	11.48	3.80	1.84	11.66	0.05
Model obs-time land	8.14	3.28	2.80	3.74	0.23
Model obs-time sea	5.81	1.73	1.17	5.65	0.01
Observations land	10.43	2.30	2.51	9.66	1.23
Observations sea	9.31	1.17	1.94	9.05	0.02

**Table 4.2**— Cloud cover diurnal cycle amplitude for model and ISCCP observations JJA 2004 - African region

#### 4.2.2 Case study-2: Amazon basin

Figure 4.3(a) and figure 4.3(b) show the diurnal variation of total cloud cover (black), high cloud cover (blue) and the deep-convective cloud cover (pink) for the Amazonian land and sea region respectively. For this region, the total cloud amount is

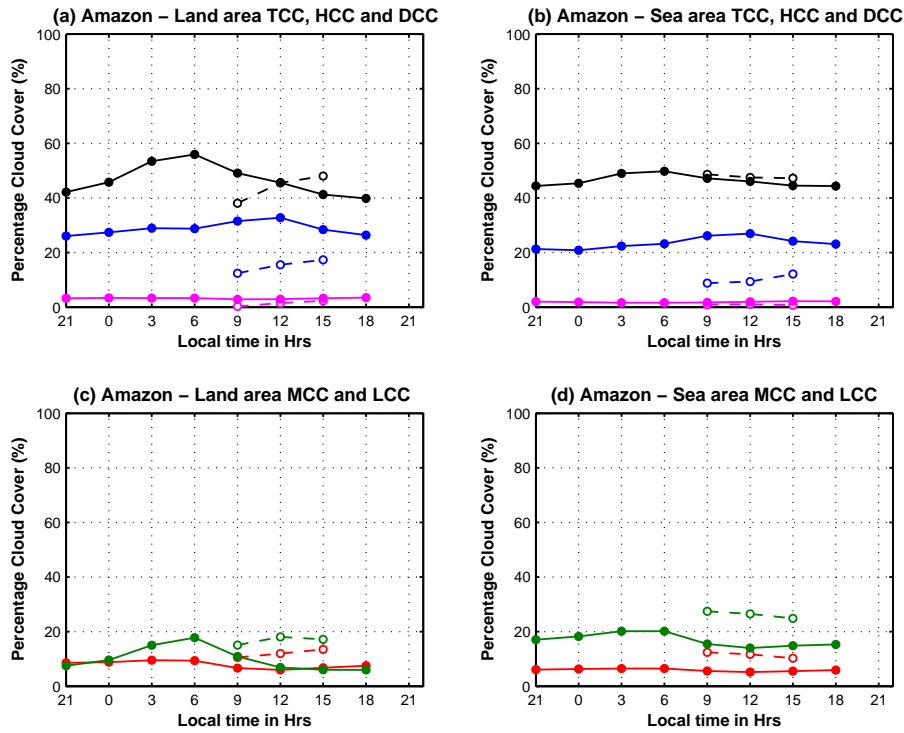


**Figure 4.3**— Diurnal cycle for land and sea: model results and ISCCP observations over the Amazon region

—○—:ISCCP TCC; - -○- :ISCCP HCC; - -○- :ISCCP DCC; - -○- :ISCCP MCC; - -○- :ISCCP LCC;  
 ●— :Model TCC; ●— :Model HCC; ●— :Model DCC; ●— :Model MCC; ●— :Model LCC

overestimated for land, but rather well simulated for sea area compared to the ISCCP observations. From these figures, one can notice the overestimation of high clouds in both the land and the sea areas. Moreover, a phase difference of 3 hours too early for the peak of high cloud cover, and 9 hours too early for the total cloud cover is observed for the land and the sea areas. Too little convective cloud is diagnosed in the Amazon area and hence the diurnal variation of convective clouds is insignificant, although the model still overestimates it compared to the ISCCP observations ( $\sim 1\%$  for both the land and the sea regions).

Figure 4.3(c) and 4.3(d) show the comparison of model and observations for the mid-level cloud (red) and the low clouds (green) for Amazonian land and sea, respectively. The model clearly underestimates the mid cloud cover (i.e.,  $\sim 5\%$  and  $\sim 6\%$  for the land and the sea respectively) and the low cloud cover (i.e.,  $\sim 7\%$  and  $\sim 10\%$  for the land and the sea respectively). The Amazon land region shows a negative phase shift of maxima (too early) for the mid and the low clouds. The sea area shows a reasonable estimate of phase (maximum and minimum) for the mid and low clouds but both the cloud types are underestimated by the model compared to observations.

Table 4.3 lists the daily average values of the cloud cover for the model and

observations. In terms of diurnal averages, the values of the model simulated ISCCP clouds, for both the land and the sea area of the Amazon region show a similar amount of total cloud cover (difference under  $\sim 3\%$ ). On the other hand, a much larger discrepancy can be noticed in the estimation of high cloud cover for both the land and the sea areas which amounts up to  $\sim 13\%$  more in the model compared to the observations. These values make the model high cloud amount almost double than that of the observations. Similarly, deep-convective cloud amount is observed more in the model (by  $\sim 1\%$  to  $2\%$ ) when compared to the ISCCP satellite data. The model underestimates the mid cloud cover by  $\sim 6\%$  and similarly, the low cloud cover is underestimated by  $\sim 5\%$  for the Amazonian land and the sea areas.

Cloud types	ISCCP cloud cover in %				
	Total cloud	High cloud	Mid cloud	Low cloud	Deep-conv. cloud
Amazon model land	46.62	28.77	7.89	9.95	3.22
Amazon ISCCP land	43.86	15.09	12.01	16.76	1.33
Amazon model sea	46.33	23.50	5.94	16.89	1.88
Amazon ISCCP sea	47.79	10.08	11.43	26.27	0.88

**Table 4.3**— Mean cloud cover values for model and ISCCP observations JJA 2004 - Amazon region

The differences in the amplitude of the diurnal cycle for the land and the sea areas are listed in table 4.4. These differences are calculated separately for all the model time steps and for time steps when observations exist. The timing of the diurnal peaks for various cloud types show that the maximum cloud amount in the model is diagnosed  $\sim 3$  to 6 hours earlier compared to the ISCCP observations.

Cloud types	ISCCP cloud cover in %				
	Total cloud	High cloud	Mid cloud	Low cloud	Deep-conv. cloud
Model all time land	16.08	6.69	3.54	11.82	0.62
Model all time sea	5.47	6.08	1.33	6.17	0.53
Model obs-time land	7.86	4.33	0.79	4.85	0.37
Model obs-time sea	2.64	2.72	0.43	1.47	0.43
Observations land	9.93	4.87	2.93	2.99	2.01
Observations sea	1.43	3.30	2.15	2.58	0.31

**Table 4.4**— Cloud cover diurnal cycle amplitude for model and ISCCP observations JJA 2004 - Amazon region

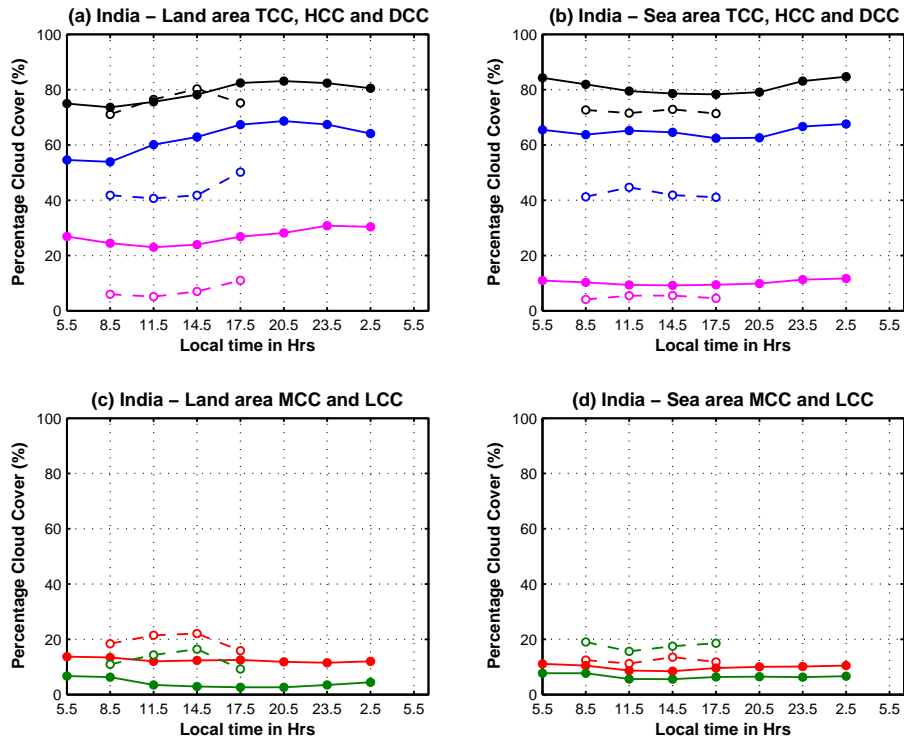


**Figure 4.4**— Diurnal cycle for land and sea: model results and ISCCP observations over the Indian region  
 -○- -:ISCCP TCC; -○- -:ISCCP HCC; -○- -:ISCCP DCC; -○- -:ISCCP MCC; -○- -:ISCCP LCC;  
 -●- :Model TCC; -●- :Model HCC; -●- :Model DCC; -●- :Model MCC; -●- :Model LCC

### 4.2.3 Case study-3: Indian subcontinent

The Indian subcontinent being a summer monsoon region shows comparatively larger values for the high and the deep-convective cloud cover in comparison to other test areas. Figure 4.4(a) and figure 4.4(b) show the diurnal variation of total cloud cover (black), high cloud cover (blue) and the convective cloud cover (pink) for the Indian land and sea region respectively. For the land area in the Indian region, the total cloud cover is simulated quite reasonably with agreement to the phase and amplitude of the diurnal variation of ISCCP observations. The model overestimates high cloud cover and the convective cloud cover being a subset of high cloud cover is also overestimated for the Indian land area. As seen in figure 4.4(b) the sea area shows an overestimation of the total cloud cover, high cloud cover, and the convective cloud cover.

The diurnal harmonic for the mid-level cloud and the low clouds for Indian land and sea are shown in figure 4.4(c) and 4.4(d) respectively for the comparison of model and the observations. The mid and the low cloud cover for continental India peak around morning or ~6 hours too early compared to the ISCCP observations. For the low cloud cover, the sea area shows a similar phase for the diurnal cycle but

lower values of cloud cover (figure 4.4(d)). However, the land area anyway shows lower amounts of shallow clouds and the phase of the diurnal cycle has insignificant variation compared to the observations (figure 4.4(c)).

A comparison of the daily averaged values of the cloud amount is listed in table 4.5 for the Indian region. The total cloud cover is comparatively well simulated for the Indian land area with less than  $\sim 3\%$  overestimation of the observation values. The sea area, on the other hand, shows a larger difference ( $\sim 10\%$  overestimation) in total cloud amount. Both the sea and the land area show an overestimation of  $\sim 20\%$  for the high cloud amount. Deep-convective cloud amount is also overestimated by the model for the Indian land area ( $\sim 20\%$ ) as well as for the ocean area ( $\sim 6\%$ ).

Underestimation of the mid cloud cover is  $\sim 7\%$  for land and  $\sim 3\%$  for the sea area. A similar behavior is seen for the model low clouds with an estimation of  $\sim 8\%$  too little for the land and  $\sim 11\%$  too little for the sea area when compared to the ISCCP observations.

Cloud types	ISCCP cloud cover in %				
	Total cloud	High cloud	Mid cloud	Low cloud	Deep-conv. cloud
India model land	78.86	62.37	12.41	4.07	26.80
India ISCCP land	75.76	43.60	19.43	12.72	7.27
India model sea	81.20	64.78	9.86	6.55	10.25
India ISCCP sea	72.12	42.21	12.23	17.67	4.89

**Table 4.5**— Mean cloud cover values for model and ISCCP observations JJA 2004 - Indian region

The differences in the amplitude of the diurnal cycle have been calculated as before for the land and the sea areas, and are listed in table 4.6. For the Indian monsoon region, the diurnal peak of the continental convective clouds is seen around 20:00 LST or  $\sim 6$  hours later than the observation peak unlike the other test areas where the maximum convective cloud fraction occurs too early compared to the observations. The role of local dynamics due to the strong monsoon fronts (strong convective clouds and heavy precipitation later) in this area may be attributed to this behavior of the diurnal cycle of convective clouds. This region experiences the greatest amount of deep-convective clouds in comparison to the other test areas.

#### 4.2.4 Case study-4: Indonesian convective region

The Indonesian region also shows a similar diurnal behavior for various clouds as the other test regions. The Indonesian region shows a reasonable estimation of total cloud cover for sea area (figure 4.5(b)) but overestimates the same for the land area (figure 4.5(a)). A much larger overestimation is seen in the high cloud cover for the land area compared to the sea area in the Indonesian region in the morning hours. This larger overestimation can be related to the corresponding larger underestimation of low clouds in the land area (figure 4.5(c)). The sea area however,

Cloud types	ISCCP cloud cover in %				
	Total cloud	High cloud	Mid cloud	Low cloud	Deep-conv. cloud
Model all time land	9.49	14.73	2.21	4.11	7.79
Model all time sea	6.39	5.18	2.67	2.14	2.46
Model obs-time land	8.85	13.41	1.42	3.67	3.84
Model obs-time sea	3.63	2.79	2.04	2.14	1.08
Observations land	9.17	9.45	6.24	7.17	5.88
Observations sea	1.53	3.63	2.31	3.37	1.41

**Table 4.6**— Cloud cover diurnal cycle amplitude for model and ISCCP observations JJA 2004 - Indian region

shows similar diurnal variation of deep-convective clouds as the ISCCP observations (figure 4.5(b)).

The average values of diurnal variation of the model simulated ISCCP cloud amounts for the Indonesian region are shown in table 4.7. The Indonesian sea area gives a well simulated diurnal average value with less than  $\sim 2\%$  overestimation discrepancy compared to the observations. However, the land area shows a substantial overestimation of total clouds with estimating  $\sim 14\%$  higher cloud cover than the observations. A considerable increase in the estimation of the high cloud cover is seen for Indonesian land region which amounts up to  $\sim 35\%$  or almost the double of what the observations show.

Comparison of mid cloud amount reveals an underestimation of  $\sim 5\%$  for land and  $\sim 8\%$  for the sea area. The low cloud cover are also seen less than those in observations with  $\sim 15\%$  too little for land and  $\sim 7\%$  too little for the sea area. The differences in the amplitude of the diurnal cycle for the land and the sea areas are shown in table 4.8.

Cloud types	ISCCP cloud cover in %				
	Total cloud	High cloud	Mid cloud	Low cloud	Deep-conv. cloud
Indonesia model land	85.78	70.74	12.70	2.32	12.73
Indonesia ISCCP land	71.76	36.35	17.93	17.48	3.62
Indonesia model sea	67.95	53.36	6.53	8.05	4.19
Indonesia ISCCP sea	64.51	34.32	14.69	15.49	4.09

**Table 4.7**— Mean cloud cover values for model and ISCCP observations JJA 2004 - Indonesian region

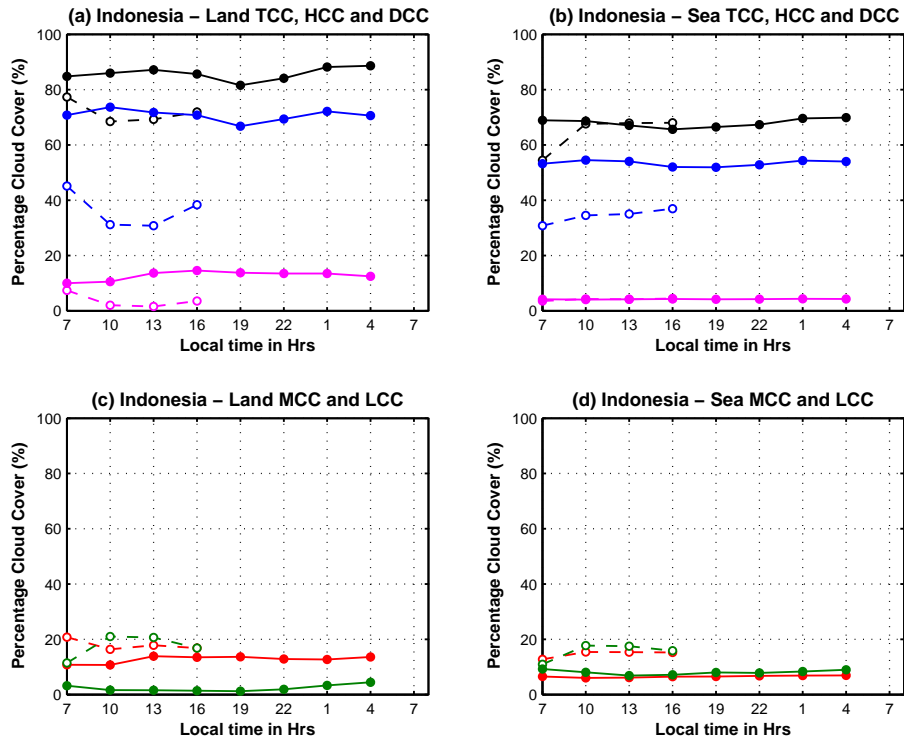


**Figure 4.5**— Diurnal cycle for land and sea: model results and ISCCP observations over the Indonesian region

—○— :ISCCP TCC; —○— :ISCCP HCC; —○— :ISCCP DCC; —○— :ISCCP MCC; —○— :ISCCP LCC;  
 —●— :Model TCC; —●— :Model HCC; —●— :Model DCC; —●— :Model MCC; —●— :Model LCC

Cloud types	ISCCP cloud cover in %				
	Total cloud	High cloud	Mid cloud	Low cloud	Deep-conv. cloud
Model all time land	7.04	6.89	3.15	3.22	4.56
Model all time sea	4.24	2.55	0.88	2.35	0.29
Model obs-time land	2.39	2.89	3.15	1.81	4.56
Model obs-time sea	3.29	2.45	0.45	2.35	0.21
Observations land	8.86	14.32	4.42	9.52	5.84
Observations sea	13.57	6.18	2.66	6.78	0.90

**Table 4.8**— Cloud cover diurnal cycle amplitude for model and ISCCP observations JJA 2004 - Indonesian region

### 4.3 Summary and conclusions

The ECHAM5 model evaluation results show that the diurnal cycle for various tropical regions with different characteristics is substantially different. The land sea

behavior in the diurnal harmonic of the ISCCP category clouds derived from the ISCCP simulator provides robust results for test case studies compared to the ISCCP observations. The diurnal cycles of high and deep-convective clouds analyzed in this study come out to be very weak for both the model as well as the observations, except for the Indian monsoon region. One difference in our analysis in comparison to previous studies is that, we compare the cloud cover and not convective precipitation (which is a more direct property of deep-convection). However, since we compare the cloud cover in the model and the observations, it is nevertheless worth to investigate the diurnal behavior of different cloud categories in different regions of the world.

The total cloud cover diurnal cycle in the model is similar to the observations (with  $\sim 10\%$  to  $\sim 20\%$  difference in average values). The total cloud cover diurnal cycle in the observations is dominated by the low clouds, whereas in the model, the low cloud diurnal cycle is relatively weak.

An overestimation of the high clouds ( $\sim 5\%$  to  $35\%$  absolute cloud cover for land areas,  $\sim 6\%$  to  $22\%$  for sea areas) together with an underestimation of low clouds ( $\sim 6\%$  to  $12\%$  absolute cloud cover for land areas,  $\sim 6\%$  to  $13\%$  for sea areas) is seen in the model as compared to the observations. Convective cloud cover being a subset of the high clouds is also overestimated by the model, however the regional study over Africa shows that other categories of high clouds (i.e., cirrostratus and cirrus) are also overestimated since the influence of deep-convective clouds is not significant in this area (less than  $5\%$  of convective cloud cover, refer figure 4.2).

The largest amplitudes of the land diurnal cycle of total cloud cover occur over the continental Amazon region with a maximum cloud cover in the morning ( $\sim 6$  hours too early compared to the ISCCP observations). For high clouds, the diurnal amplitude is larger over the land regions than over the sea areas for the test cases. The model derived high cloud cover diurnal cycle amplitude is stronger compared to ISCCP for land regions of all the test areas except for Indonesia where the model diurnal amplitude is weaker than the observations. The convective cloud cover diurnal behavior determines the diurnal behavior of high cloud cover except for the African region where the convective cloud cover is very little (less than  $3\%$  cloud cover over land). For the monsoon regions of India and Indonesia, the summer season (JJA 2004) analysis shows that the oceanic deep-convection tends to reach its maximum in the early morning, while convection over land areas typically peaks in the late evening. As reviewed in the literature the convection maximum over the land regions in late afternoon occur on account of a thermodynamic response to surface solar heating and leads to a precipitation maximum in the evening.

Despite the weak amplitude, tropical convective clouds display systematic diurnal fluctuations for the sea regions of the analyzed test areas. The diurnal peak of the high clouds as well as the convective clouds for sea areas is seen around early morning but the timing is observed few hours too early when compared to the ISCCP observations for deep-convective clouds (i.e., 3:00 to 5:00 hrs LST in model compared to 9:00 to 10:00 hrs LST in observations). The diurnal cycle of deep-convective clouds over sea has its lowest value around late afternoon. The strongest diurnal amplitude

for total cloud cover for the sea region occurs in the African region, influenced with the shallow oceanic clouds. In all the test areas, the diurnal peak for the oceanic total cloud cover occurs 6 hours too early compared to observations. Similar to the land regions, the low and mid cloud cover for the sea areas is underestimated by the model ( $\sim 20\%$  to  $\sim 40\%$  less) compared to the ISCCP satellite data.

The analysis of diurnal cycle of clouds in the observations reveals that the total cloud cover diurnal cycle is dominated by low clouds. However, the low clouds in the model show a much weaker diurnal behavior compared to observations due to shortcomings in the shallow convection and boundary layer parametrization.

## Chapter 5

# Convection-climate Feedbacks

*This chapter includes the climate feedback studies with focus to life-cycle studies of cirrus clouds in the model and observations. The chapter gives a detailed overview of climate feedbacks due to convective processes and the previous studies in this field. The methodology followed in convection transition analysis is based on Lagrangian tracking of convective clouds in the upper troposphere and associated cirrus formation in time.*

### 5.1 Climate feedbacks due to convection

Feedbacks in the climate system associated with clouds continue to be considered as a major source of uncertainty in model projections of global warming (Stephens, 2005). The tropics and the extra-tropics are associated with a large spectrum of cloud types, ranging from boundary layer clouds to deep-convective clouds and anvils. Because of their different top altitudes and optical properties, the different cloud types affect the Earth's radiation budget in various ways. Understanding cloud radiative feedbacks requires an understanding of how a change in climate may affect the distribution of the different cloud types and their radiative properties, and an estimate of the impact of such changes on the Earth's radiation budget (Bony et al., 2006).

Because of the profound influence of clouds on both the water balance of the atmosphere and the Earth's radiation budget, small cloud variations can alter the climate response associated with changes in greenhouse gases, anthropogenic aerosols, or other forcings of global change. Predictions of global warming by GCMs forced with prescribed increases of atmospheric CO<sub>2</sub> are uncertain, and the range of uncertainty has, seemingly, not changed much from initial estimates given decades ago (Stephens, 2005). The effects of potential changes in cloudiness as a key factor in the problem of climate change has been recognized since at least the 1970s (Arakawa, 1975; Schneider, 1972).

For more than a decade, the large spread of cloud feedbacks among climate models has been considered a major source of uncertainty for climate sensitivity estimates (Cess et al., 1990; Colman, 2003; Stephens, 2005). The representation

of convective and boundary-layer processes, in addition to the parameterization of cloud properties, is known to be critical for the prediction of the clouds' response to climate change (Senior & Mitchell, 1993; Yao & Genio, 1999), and it differs widely among models as seen in various model inter-comparison studies.

Several climate feedback mechanisms involving convective clouds have been examined with observations, simple climate models and with cloud resolving models in the past. A surprising property of clouds observed in tropical oceanic deep-convective regimes is that their long wave (LW) and short wave (SW) cloud radiative forcing (CRF) nearly cancel each other out (Ramanathan et al., 1989). Kiehl (1994) argued that this is coincidental, while Hartmann et al. (2001) suggest this is a property of the ensemble of cloud types that occurs in association with deep-convection in the tropics. Hartmann et al. (2001) argue that this ensemble of clouds adjusts through dynamical feedbacks in the ocean-atmosphere system so as to keep the radiation budget of convective regions close to that of adjacent non-convective regions.

Analyzing geostationary data over the western tropical Pacific, Lindzen et al. (2001) hypothesized that a warming climate might lead to decreased anvil cloud fraction owing to an increase of the precipitation efficiency of cumulonimbus clouds with temperature and decreased water detrained in the upper troposphere (the so-called *Iris hypothesis*). However, doubts about the evidence provided so far have been expressed by several studies and this has been a polemical issue (Chambers et al., 2002; Del Genio & Kovari, 2002; Fu et al., 2002; Hartmann & Michelsen, 2002; Lin et al., 2002; Lindzen et al., 2002). Nevertheless, the potential impact of an intrinsic temperature dependence of deep-convective cloud microphysics on climate sensitivity remains an open issue.

Hartmann & Larson (2002) proposed that the emission temperature of tropical anvil clouds is essentially independent of the surface temperature, and that it will thus remain unchanged during climate change (the so-called *fixed anvil temperature hypothesis*). Their reasoning, tested with a mesoscale model, is that the altitude of convective detrainment occurs where the clear-sky longwave radiative cooling rapidly declines with height, and that the temperature at which this decline occurs is constrained by the dependence of water vapor emission on temperature. Their hypothesis is consistent with CRM simulations (Bretherton et al., 2006), showing that in a warmer climate, the vertical profiles of mid- and upper-tropospheric cloud fraction, condensate, and relative humidity all tend to be displaced upward in height in lockstep with the temperature. This vertical displacement is found also in CRM simulations of Tompkins & Craig (1999); however, these show a slight increase of the cloud-top temperature with increasing surface temperature. Comparable simulations with other CRMs are thus needed to establish the robustness of these results, as well as its investigation in climate models.

Cirrus and cirrostratus clouds (also referred as cirriform clouds) have strong connection with deep-convective clouds, especially in the tropics. Deep-convective cloud detrainment is a main source of moisture for the upper troposphere, and the moisture produces cirrus clouds. The interplay of large-scale atmospheric dynamics and

the deep-convection source can influence this cirrus clouds. Other effects of large-scale circulation include the role of upper level flow in transporting detrained water mass and effects on condensation by adiabatic uplift (Pierrehumbert, 1998).

### 5.1.1 Transition of convective clouds to cirrostratus and cirrus

Upper-tropospheric ice-phase clouds in the tropics (or tropical cirrus) are characterized by their extensive lateral and vertical coverage. These clouds impose a substantial large-scale radiative effect on the Earth's climate system (Hartmann & Michelsen, 1993). Up to 20% of the global tropics are regularly covered by extensive cirrus systems (Liou, 1986), and these cloud layers reduce the solar radiation reaching the Earth's surface due to reflection. These cloud layers also absorb a portion of the upwelling Infrared (IR) radiation emitted by the surface and lower atmosphere and emit IR radiation at a much lower temperature, hence effectively reducing the outgoing longwave radiation and heating the atmosphere. The net radiative effect of tropical cirrus depends on several factors including the properties of the underlying surface and atmosphere (Stephens et al., 1990), the cloud amount, cloud height, cloud geometrical thickness, ice water content, and the ice crystal size distribution (Stephens, 2005). Tropical cirrus clouds, in particular, can have a unique tendency to produce positive heating anomalies in the troposphere (Ackerman et al., 1988).

Cirrus also play a role in the maintenance of the water vapor distribution in the tropics. In the regions of general subsidence well removed from deep-convection, cirrus moisten the upper troposphere and, thereby, regulate the heating rates and large-scale vertical motions of the tropics (Sherwood, 1996). In the vertical region bounded by the detrainment layer of deep-convection and the stratosphere known as the tropopause transition layer (TTL), tropical cirrus help regulate the water vapor concentrations entering the lower stratosphere in the tropics (Jensen et al., 1996; Hartmann, 2002; Dessler & Sherwood, 2000).

Tropical cirrus originate in outflow from deep-convective systems, producing a wide range of high-level clouds from thick anvils to thin cirrus that are sometimes all called cirrus, but other dynamic processes, such as the mesoscale circulations of larger storm systems, large-scale lifting or gravity waves, can also produce cirrus. Hence, the knowledge about the distribution of tropical cirrus, their variability, and formation-decay processes is still rudimentary (Luo & Rossow, 2004). With the advent of new satellite missions such as Calipso and Cloudsat, the knowledge about cloud vertical distribution is however increasing.

Cirrus (anvil cirrus and cirrostratus) clouds have strong connection with deep-convective clouds, especially in the tropics. Deep-convective cloud detrainment is a main source of moisture for the upper troposphere ( $\sim 200$ -500 hPa), and this moisture produces the cirrus and cirrostratus clouds (also referred to as cirriform clouds). The interplay of large-scale atmospheric dynamics and the deep-convection source can influence this cirriform cloud formation. Other effects of large-scale circulation include the role of upper level flow in transporting detrained water mass and effects on condensation by adiabatic uplift (Pierrehumbert, 1998). Many observation

studies also show that tropical cirrus clouds often result from the life cycle of tropical convective cloud systems. Machado & Rossow (1993) used satellite imagery to examine the properties of tropical convective cloud systems. They found that relatively thin high clouds constitute a large part of the area covered by such systems, especially when the system's entire life cycle is considered. During the mature stage, Machado & Rossow (1993) determined that the average tropical convective system consists of 20% deep-convective clouds, 28% transition anvil cloud, and 52% cirrus anvil cloud. During the dissipating stages, first the deep-convective clouds disappear, then the transition anvil clouds, leaving finally only scattered fragments of thin cirrus.

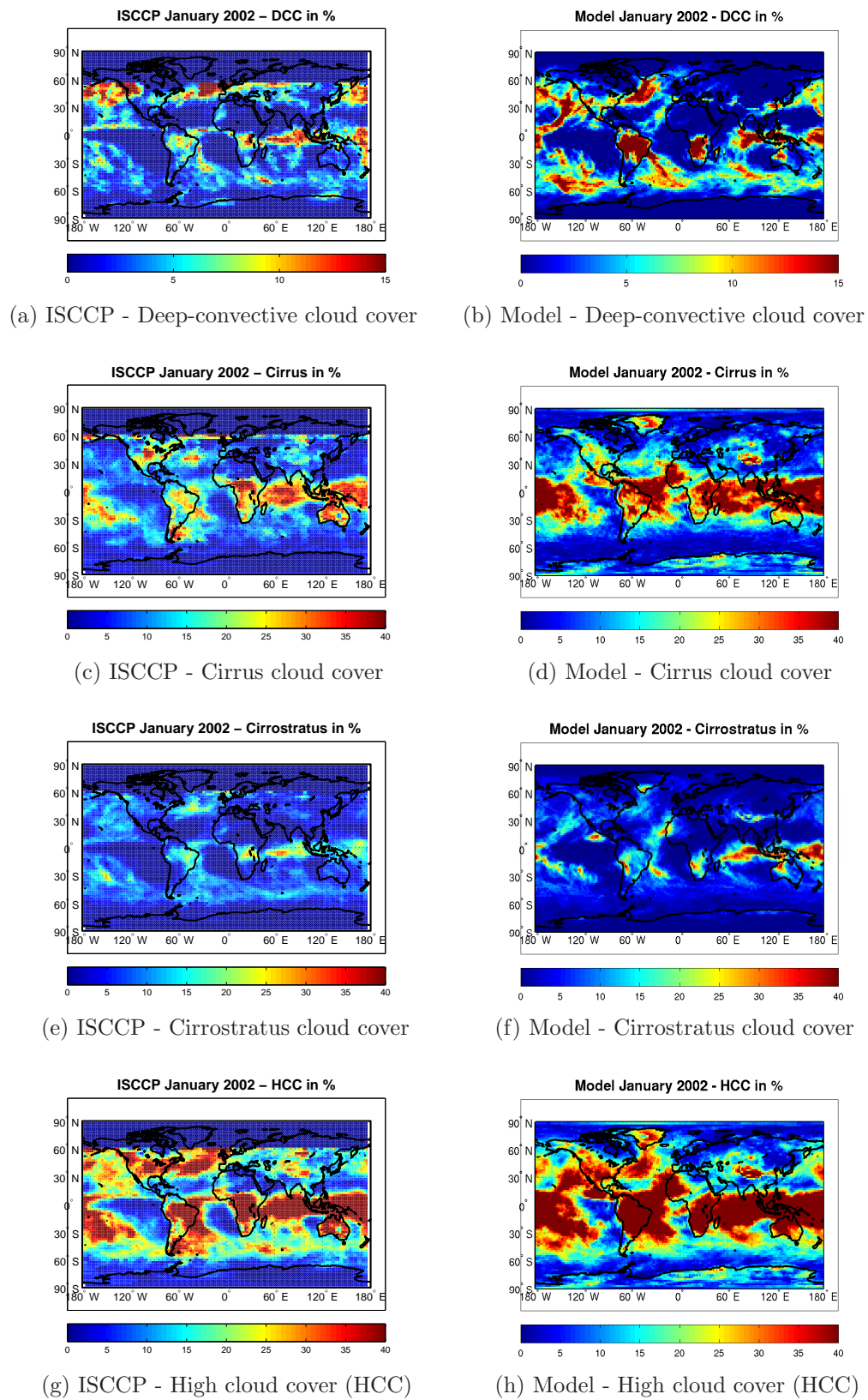
## 5.2 Comparison of global distribution of deep-convective, cirrostratus and cirrus clouds

According to the ISCCP cloud classification (refer figure 2.2), the cirrus, cirrostratus and deep-convective clouds are compared with regard to their geographical distribution within the GCM and the ISCCP observations. The categorization of clouds is based on the thresholds of cloud top pressure ( $p_{\text{top}}$ ) and cloud optical thickness ( $\tau$ ) as mentioned in Table 2.1. Additionally, the high cloud amount distribution is also compared for the observations and the model output. The latitudinal extent of the global distributions is restricted to  $\pm 50^\circ$ , in order to characterize the tropical behavior of cloud transitions.

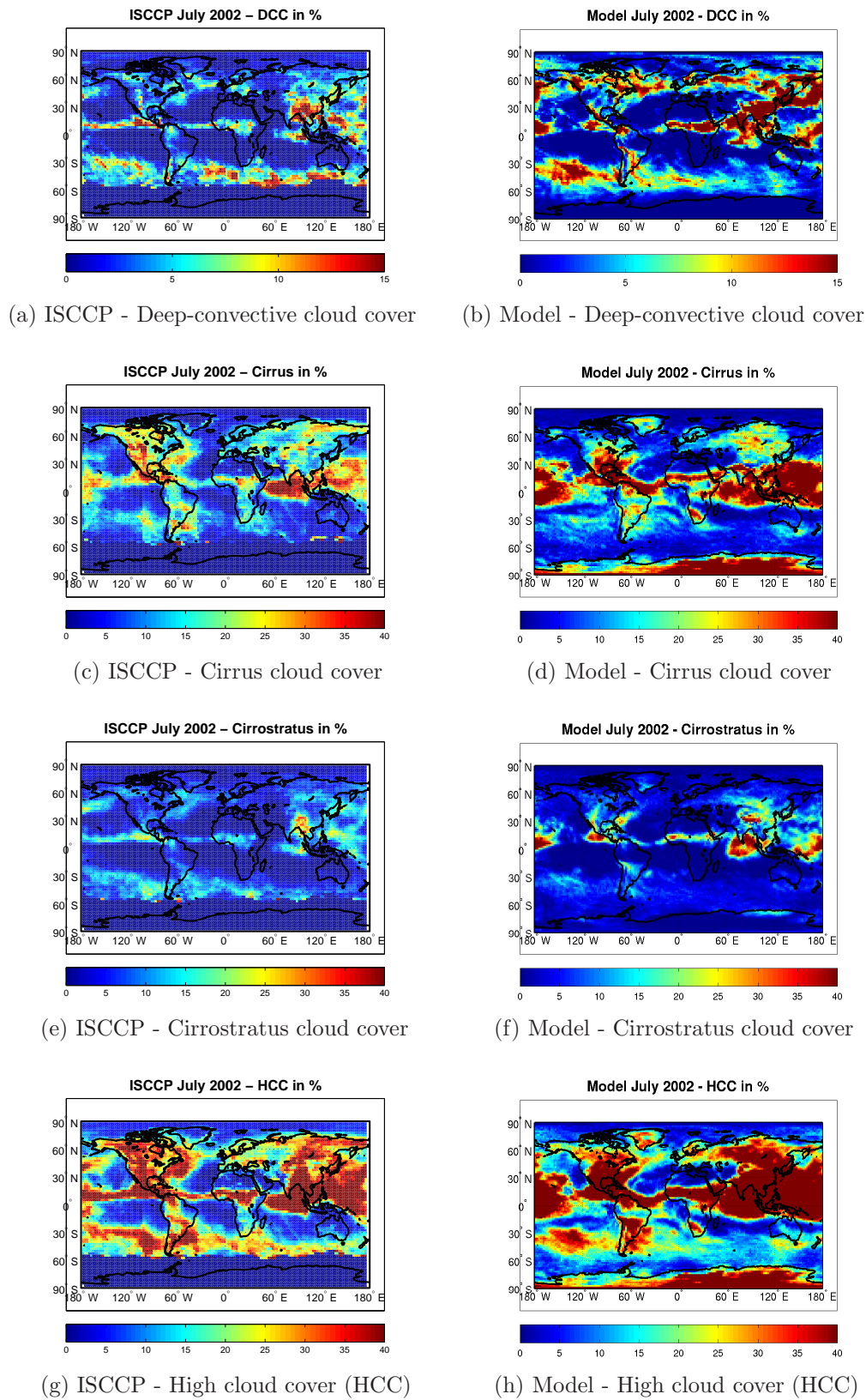
ISCCP satellite observations and the model simulations for the year 2002 are used in the current study. The northern hemisphere winter month (January) as well as summer month (July) are chosen for the analysis, although we do not expect major differences since we focus on the tropical belt of  $\pm 50^\circ$  latitude. The ISCCP observations are derived from the histograms of ISCCP-D2 product ( $1.5^\circ \times 1.5^\circ$  spatial resolution, 3-hourly data), and then converted to average quantities of deep-convective clouds, cirrus, cirrostratus, and combined high cloud cover. The model simulations are performed by using the ECHAM5 general circulation model with ISCCP simulator including the sub-column generator. The model runs are performed at T63L31 spectral grid ( $1.8^\circ \times 1.8^\circ$  spatial resolution, 31 vertical levels, 3-hourly data). More details about the model and the ISCCP simulator implementation are provided in Chapter 2.

Figure 5.1 and 5.2 show the different cloud cover distributions for the monthly average of January 2002 and July 2002 respectively. The subplots 5.1(a) and 5.1(b) show the distribution of deep-convective clouds for the observations and the model respectively. In the first glance it becomes clear that the model over-estimates the deep-convective clouds compared to the observations ( $\sim 2$  times more than observations in figures 5.1 and 5.2). Similarly, the subplots 5.1(g) and 5.1(h) show the comparison for high cloud amount. The model diagnoses a greater amount of high clouds compared to the observations.

Based on the geographical distributions, the cirrus clouds primarily populate the



**Figure 5.1**— Comparison of ISCCP observations and model simulated cloud cover for January 2002. The subplots show different ISCCP cloud categories and the colorbar represents the respective cloud fractions in percentage.



**Figure 5.2**— Comparison of ISCCP observations and model simulated cloud cover for July 2002. The subplots show different ISCCP cloud categories and the colorbar represents the respective cloud fractions in percentage.

tropics as seen in figures 5.2(c) and 5.2(d). Generally, tropical cirrus are located in the regions where convective activity is frequent and moisture is abundant, i.e., the tropical warm pool, tropical Africa, the Amazon, the Intertropical Convergence Zone (ITCZ), and the South Pacific Convergence Zone (SPCZ). The cirrus geographical distribution is similar in the observations and the model, however the cloud amount in the ECHAM5 model is slightly higher as seen in figures 5.1(d) & figure 5.1(e) and figures 5.2(d) & figure 5.2(e). The cirrostratus clouds on the other hand extend along the sub tropics as seen in the model diagnostics in figure 5.2(f) with a value ranging upto  $\sim 25\%$  in absolute cloud fraction amount. For the ISCCP observations, the cirrostratus clouds range upto a maximum of  $\sim 15\%$  (figure 5.2(e)).

For the northern hemisphere summer month (July 2002 in figure 5.2), the model and the ISCCP observations show a similar distribution as in the winter month. The tropical areas around the Indian subcontinent and continental United States show a higher amount of high and deep-convective clouds when compared to the northern hemisphere winter month (January 2002 in figure 5.1).

### 5.3 The Lagrangian forward trajectory method

In order to analyze the transition of deep-convective clouds to cirrus clouds, we use the Lagrangian trajectories to track the deep-convective air parcels in the observations and in the model output. The extracted cloud properties over the trajectory path are analyzed to compute the daily average transition histograms for 5 days following a deep-convective event. The main assumption here is that cirrus clouds, like other tracers (e.g., water vapor), drift with the upper-tropospheric wind, while at the same time, going from formation to maturation to decay.

Trajectories of air parcels are constructed using upper-tropospheric winds obtained from the wind fields provided by reanalysis of past observations (for ISCCP observations) and model wind fields (for ISCCP simulator model output). Thus, the cirrus cloud evolution is tracked by keeping a record of its various stages along these trajectories. A similar method has been employed to study marine stratus clouds (Bretherton & Pincus, 1995; Pincus et al., 1997) and upper-tropospheric humidity (Salathe & Hartmann, 1997, 2000) regionally. Luo & Rossow (2004) extended this trajectory analysis to global 6-hourly ISCCP observations using NCEP-NCAR reanalysis wind data. Another study for the deep-convection transition was by Horváth & Soden (2008) where they determined cirrus life cycle and  $e$ -folding times (time to grow or decay  $e$  (or  $\sim 2.7$ ) times) and their relation to upper-tropospheric humidity using satellite observations. In this study, we extend the analysis done by Luo & Rossow (2004) to ISCCP D1 day-time observations and ISCCP simulator model diagnostics. The transition analysis of deep-convection to cirrus for a GCM output has not been investigated before. The ECHAM5 GCM at a spectral resolution of T63L31 is analyzed for cloud transitions in this study.

In this study, we compute the global trajectories originating from convective target locations and following their path for next 5 consecutive days. The analysis is

performed consistently in model and observations for the selected period of winter and summer months, i.e., January and July for the year 2002. The horizontal trajectories (time evolution of air parcels originating at a defined height) are computed with the HYbrid Single-Particle Lagrangian Integrated Trajectory Model (HYSPLIT) (Draxler, 1997) using gridded meteorological fields from the ERA40 reanalysis data of the European Center for Medium-range Weather Forecasts (ECMWF). The reason for selecting the year 2002 for this analysis is also based on the fact that the ERA-40 reanalysis data is available only up to year 2002. ERA-40 data has a spatial resolution of  $1.5^\circ \times 1.5^\circ$  and a temporal resolution of 6 hours. From this data set, we use the three-dimensional vertical distribution of wind, temperature and relative humidity together with the two-dimensional wind fields at 10 meter height, temperature fields at 2 meter height and the surface geopotential to compute the observational trajectories of air parcels with the HYSPLIT program.

The average of the wind field over the whole air column between 500 and 200 hPa in the reanalysis data is used to represent the upper-tropospheric wind. Vertical movement of air masses is not examined explicitly because the quality of the vertical wind from the reanalysis is not known. Hence, the two-dimensional movement of the air columns within the 500 to 200 hPa layer is considered in this study. A similar approach was taken by Pincus et al. (1997) and Salathe & Hartmann (1997). Because of this limitation, a forward air trajectory is followed for a maximum of 5 days because after 5 days, the air column between 500 and 200 hPa may well have subsided into a lower level (Luo & Rossow, 2004).

In case of the model simulated ISCCP output, the ECHAM5 three-dimensional vertical distribution of wind, temperature and relative humidity is used together with the two-dimensional model wind fields at 10 meter height, temperature fields at 2 meter height and the surface geopotential to compute the model trajectories of air parcels with the HYSPLIT program. The trajectories are originated at a height of 7 km to represent the upper-tropospheric deep-convective origins of trajectories within the HYSPLIT model.

The cirrus cloud amount, as well as average cirrus properties ( $p_{\text{top}}$  and  $\tau$ ) within each observation or model grid box are calculated for every time step. As the HYSPLIT program provides desired temporal (3 hours in our case) locations of the air parcels along the trajectories, every time an observation/model field is available, we can extract the cloud properties supplied by this field at the corresponding location of the air parcel. The cloud properties of the air parcels along each trajectory are computed via the nearest available grid-box cloud information for the respective parcel location and the observation/model output time. Following the study of Luo & Rossow (2004), the cirrus amount is used as an indicator of its life cycle. For example, cirrus lifetime can be measured as the duration along a trajectory (or part of a trajectory) that exhibits a sequence from zero cirrus to some amount of cirrus to zero cirrus again. For cirrus formed by convective detrainment, cirrus amount monotonically decreases (after a start-growth phase) until it vanishes.

The forward air trajectory analysis in this study depends on selecting the tra-

jectory origins based on deep-convection events. These deep-convective events are defined as the last grid box in a time sequence that has more than 10% of deep-convective cloud cover. In order to assure that this deep-convective cloud amount at an instant is the start of an event, an additional condition is imposed that the downstream grid-boxes of this convective core have less deep-convective cloud amount than the starting location. This additional condition ensures that the last convective event ended and the rest of the deep-convection seen over the trajectory path is an individual convective core independent of previous events. The trajectories are considered valid only when they fulfill the criteria mentioned above, else they are discarded in the analysis. The rationale for starting the trajectories close to the convective core is to sample the whole transition from deep-convection to thick anvil to cirrostratus and finally to cirrus. Starting the trajectories from convective systems does not imply that all cirrus are assumed to be derived from convection, as cirrus are also allowed to re-form along the trajectories. Initiating trajectories from where convection dies out provides a convenient way of comparing cirrus formed from convective detrainment to cirrus formed in-situ (more details in section 5.4).

Moving along a forward trajectory, convective activity can sometimes last for several hours (Machado et al., 1998). In this case, the last time step is considered to be the decay stage of the convective system and our search for cirrus starts from there. If a forward trajectory encounters another convective system along the way, this trajectory is terminated and new one starts from there. In principle, the 6-hour sampling time for individual trajectory starting locations is considered good enough to capture the next convective event over time.

Figures 5.3 and 5.4 show examples of the forward air trajectories from a winter month (January) of the year 2002 for the ISCCP observations and the GCM output, respectively. Similarly, the summer month (July) trajectories of year 2002 are shown for the observations (figure 5.5) and the model (figure 5.6). The red circles on the trajectory plots represent the starting locations for the trajectories (selected convective targets). The usual centers of convective activity are evident in the figure: tropical western Pacific, tropical Africa, and the Amazon. A clear shift of the tropical ITCZ for winter (figure 5.3) and summer month (figure 5.4) are observed both in the model and the observations. Upper-tropospheric air parcels start from these convective centers and make their way into the subtropics or tropical dry regions (such as the eastern Pacific). It is also interesting to see that some of the air parcels, mostly in the winter hemisphere, are picked up by subtropical jet streams and travel a longer distance over the 5-day period. On an average, the model has more convective targets than the ISCCP observations. This is consistent with the findings of chapter 4, where the diurnal cycle analysis shows an overestimation of deep-convective clouds in the model.

On an average, when the model data is sampled every 6 hours for the determination of deep-convective targets, there are  $\sim 1600$  to 2000 trajectories initialized for each sampling time step. Hence for an overall sampling of one month in the model data is comes out to be in range of 200,000 trajectories, which gives the analysis a fairly robust statistics. On the other hand, the observations

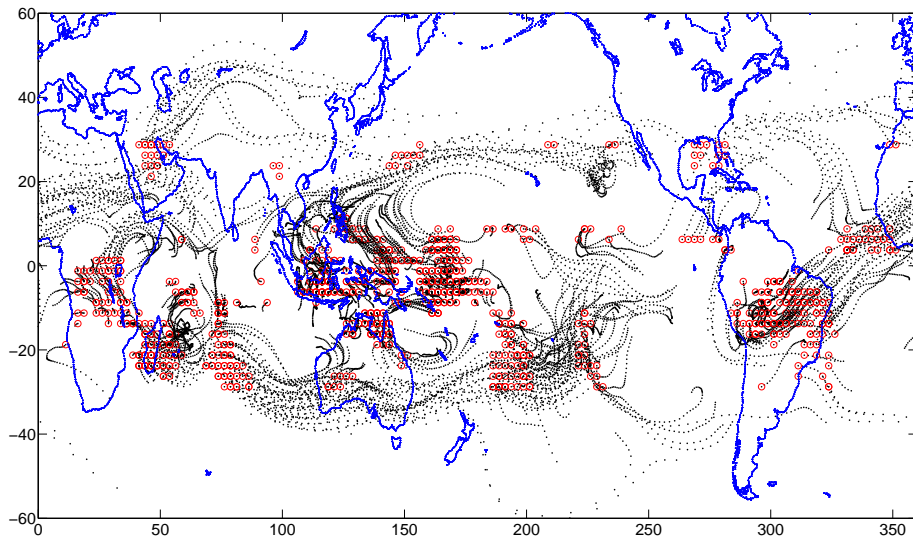


**Figure 5.3**— Example of tropical forward trajectories for ISCCP observations - January 2002. The shown trajectories evolve from one particular sampling instance.

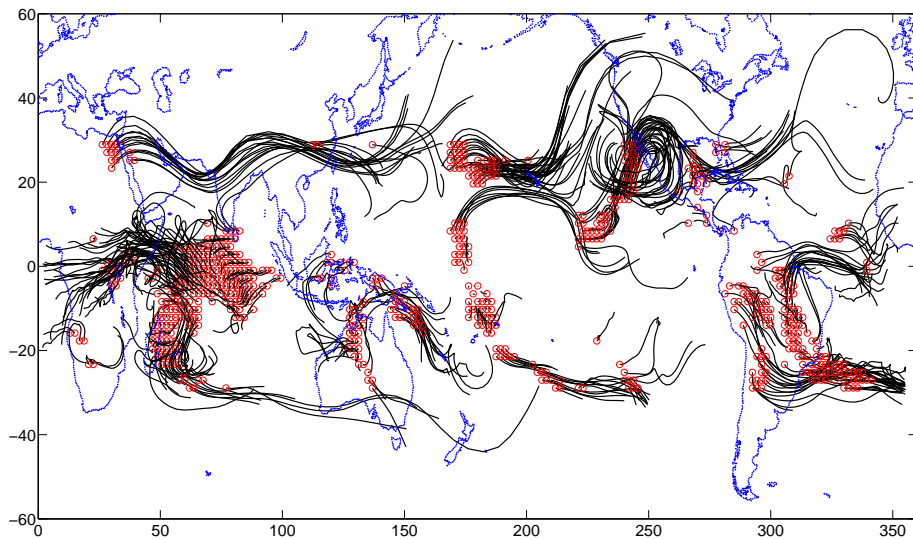


**Figure 5.4**— Example of tropical forward trajectories for ECHAM5 model output - January 2002. The shown trajectories evolve from one particular sampling instance.

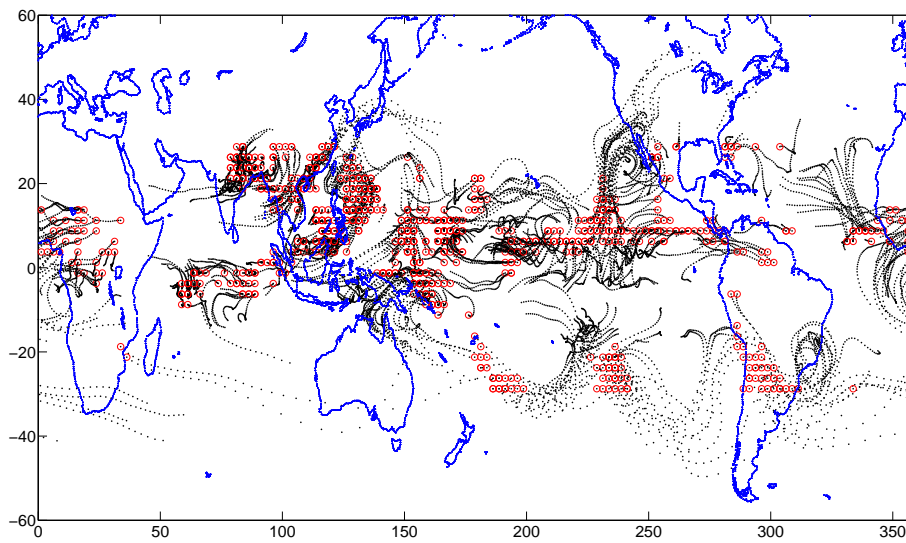


**Figure 5.5**— Example of tropical forward trajectories for ISCCP observations - July 2002. The shown trajectories evolve from one particular sampling instance.

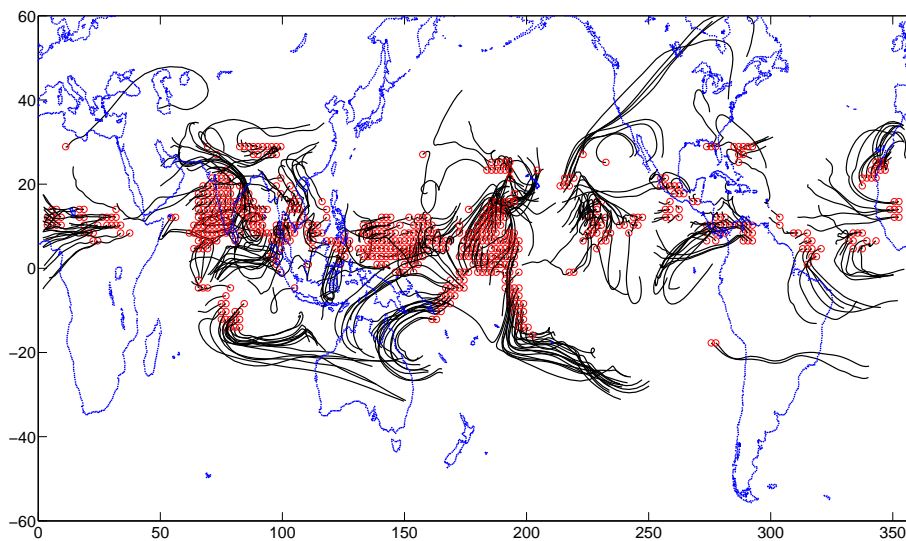


**Figure 5.6**— Example of tropical forward trajectories for ECHAM5 model output - July 2002. The shown trajectories evolve from one particular sampling instance.

trajectories are in the range of  $\sim 300$  to 450 trajectories per sampling time, making an overall composite of 48,000 trajectories for one month. The over-estimation of deep-convection in the ECHAM5 model leads to this difference in number of trajectory initialization locations, however, in both the model and observations, the samples are sufficiently large to produce unbiased results for Lagrangian analysis.

Figures 5.3, 5.4, 5.5, and 5.6 show the trajectory path and their starting locations in an instantaneous sense as an example. However, to have an idea about the frequency of occurrence of deep-convective targets, figure 5.7 shows that how often a particular location is selected in a 6-hour sampling time for a monthly model output. Figure 5.7(a) shows the convective targets frequency of occurrence for northern hemisphere winter month (January) and figure 5.7(b) shows the same for northern hemisphere summer month (July). The frequency occurrence values are normalized by the maximum value. In principle, the variation in percentage for the frequency of occurrence of convective target locations is similar to the monthly average distribution of deep-convective cloud amount as seen in figure 5.1(b) and figure 5.2(b) for the months of January and July respectively.

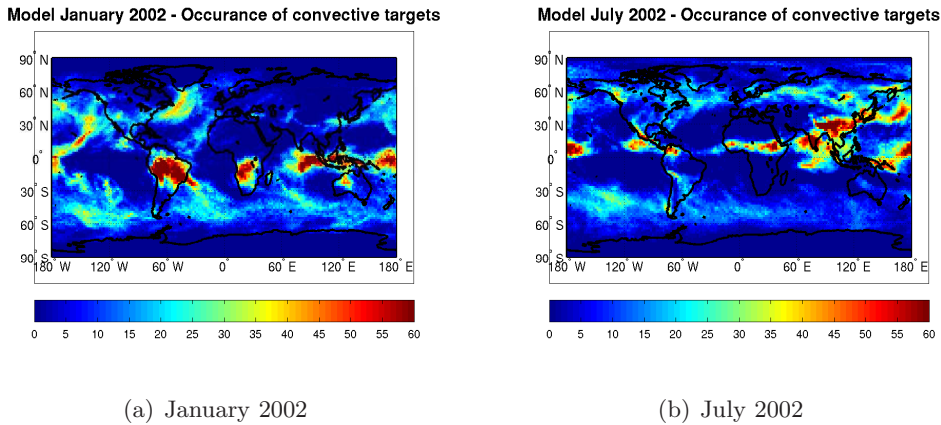


**Figure 5.7**— Normalized frequency of occurrence of convective target locations in model data for NH winter (left) and NH summer (right) from year 2002.

The northern hemisphere winter and summer analysis of the cloud distributions (figure 5.1 and figure 5.2), as well as the trajectory origin locations (figures 5.3, 5.4, 5.5 and 5.6) show no substantial seasonal difference. Considering that the tropical belt of  $\pm 50^\circ$  latitude is studied, further analysis of the cloud transitions is carried out only for the winter month of the year 2002.

### 5.3.1 Cloud transitions seen in ISCCP cloud property histograms

The sequential daily average histograms are analyzed for the model and the observations. These histograms essentially show a Lagrangian view of tropical circulation of

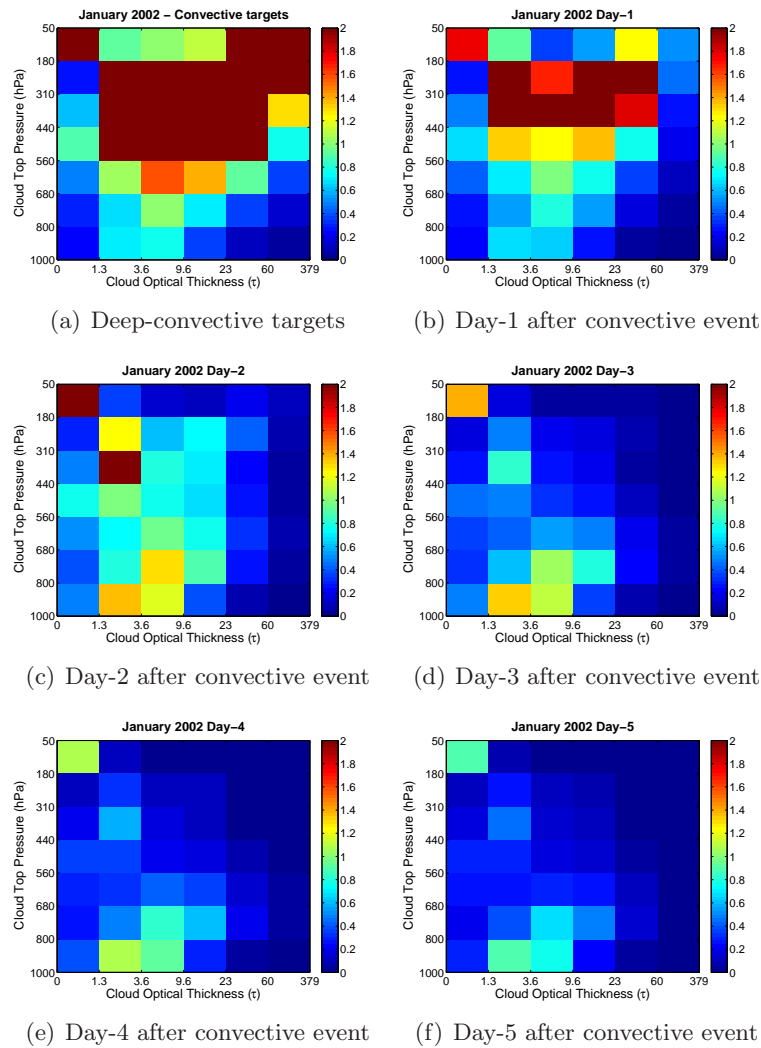


**Figure 5.8**— ISCCP observation lagrangian transition histograms for January 2002. ISCCP histograms for each day are computed over averaged trajectories starting from deep-convective targets and traveling for next 5 days after the convective event.

deep-convection formation, its transition to anvil cirrus via detrainment and lastly its decay after 5 days. The daily average histograms for the ISCCP observations as well as the model ISCCP simulator output are created by averaging over all the trajectories that are considered valid (i.e., ensure that they originate from a new convective event).

Time from last convective event	ISCCP cloud types				
	Total cloud	High cloud	Deep-conv. cloud	Cirrostratus cloud	Cirrus cloud
Deep-conv. targets	97.0	73.3	32.3	27.5	13.4
Day-1	40.1	27.0	7.3	10.6	9.0
Day-2	24.6	10.6	1.0	3.0	6.4
Day-3	14.5	4.4	0.1	0.9	3.3
Day-4	10.9	3.0	0.1	0.5	2.3
Day-5	8.9	2.5	0.1	0.4	1.9

**Table 5.1**— Mean values of cloud amount from ISCCP observations - January 2002

### ISCCP observation histograms

Following the forward air trajectories, cloud properties (or cloud types) undergo a systematic change. Figure 5.8 shows the cloud property distribution derived from the ISCCP observations in terms of cloud top pressure ( $p_{\text{top}}$ ) and optical thickness ( $\tau$ ) joint histograms. The details of various cloud categories associated with the joint  $p_{\text{top}} - \tau$  histograms are explained in chapter 2. The histogram distribution plots are shown for the convective source regions and for the consecutive 5 days following the last convection. The convective source regions are defined by deep-convective cloud amount in the ISCCP simulator model output. The sequential plots in figure 5.8 show the transition of deep-convective clouds (figure 5.8(a)) to cirrostratus clouds after 1 day (figure 5.8(b)) and finally detraining to form thin cirrus afterwards as seen in figures 5.8(c) to 5.8(f). Note that obscuration of low clouds by high clouds is not likely a serious issue, since our study focusses on high deep-convective and cirrus clouds.

The ISCCP day-time observation cloud amounts of various categories in the average 5 day transitions over all the trajectories are listed in Table 5.1 for January 2002. For the winter month, the ISCCP observational total cloud cover drops from 97.0% in the convective source regions to 8.9% on the 5th day. The high cloud cover drops down from 73.3% for the convective target locations to 27.0% on day-1 and finally reduces to 2.5% on the 5th day of trajectory. The deep-convective cloud cover, being a subset of high cloud dominate on day-1 and then reduces to  $\sim 0.1\%$  from day-2 onwards. The cirrus cloud cover reaches its maximum (13.4%) on day-1 following the decrease in deep-convective clouds and then decreases monotonically on the rest of the days (6.4% on day-2 to 1.9% on day-5). The behavior of cirrostratus follows the deep-convective clouds with maximum value on the convective target locations (27.5%), and gradual decrease afterwards with 10.6% on day-1 to 0.4% on day-5. The relation between cirrus and cirrostratus growth is consistent with the findings of Luo & Rossow (2004) which is discussed in detail in 5.3.2.

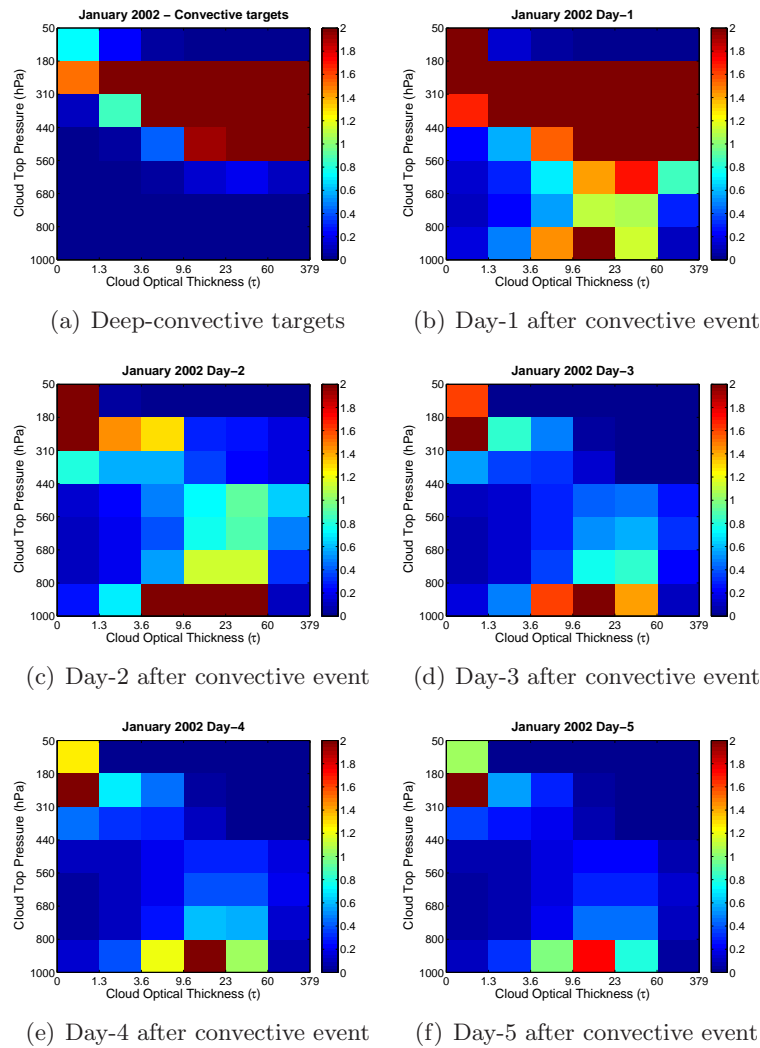


**Figure 5.9**— Model Lagrangian transition histograms for January 2002. Simulated ISCCP histograms for each day are computed over averaged trajectories starting from deep-convective targets and traveling for next 5 days after the convective event.

### Model output histograms

To compare the observation analysis to model simulations, the histogram transition plots for the ECHAM5 model output are shown in figure 5.9. As in the observations, the model histograms are created by averaging over all the trajectories for the winter month of year 2002.

Figure 5.9 shows the cloud property distribution from model output in terms of  $p_{\text{top}} - \tau$  joint histograms for the convective source regions and for 5 days following the last convection. The sequential plots show the transition of deep-convective

Time from last convective event	ISCCP cloud types				
	Total cloud	High cloud	Deep-conv. cloud	Cirrostratus cloud	Cirrus cloud
Deep-conv. targets	99.9	90.4	52.2	31.4	6.8
Day-1	91.3	65.3	23.8	25.0	16.4
Day-2	32.0	13.1	0.8	2.5	9.7
Day-3	20.2	7.5	0.06	0.9	6.4
Day-4	15.5	6.1	0.03	0.8	5.2
Day-5	12.0	4.8	0.02	0.6	4.1

**Table 5.2**— Mean values of cloud amount from model - January 2002.

cloud targets (figure 5.9(a)) to cirrostratus clouds after 1 day (figure 5.9(b)) and finally detraining to form thin cirrus afterwards as seen in figures 5.9(c) to 5.9(f). Hence, as air makes its way from convective regions to dry regions, it travels from a place where high, thick clouds prevail, to a place where cirrus and low-level clouds dominate. An example where this happens in an organized manner is the traditional picture of the Hadley-Walker circulation concerning how the large-scale circulation influences clouds, except that Figure 5.9 shows the influence from a Lagrangian trajectory perspective. Rather than treating convective centers (such as the ITCZ) only in the time average, the intermittent convective systems with scales of a few hundred kilometers are considered, which are separated by relatively clear and dry regions. Cirrostratus and thicker cirrus, which are prevalent close to the convective regions (lasting only about 1 day), become less and less frequent as air moves into dry regions. On the other hand, low-level clouds become important several days after air leaves the convective regions and continue to grow more and more prevalent.

The model simulated cloud amounts of various categories in the average 5-day transitions over all the trajectories for the winter month for year 2002 are listed in Table 5.2. For the winter month, the total cloud cover drops from 99.9% in the convective source regions to 12.0% on the 5th day for the winter month. The high cloud cover drops down from 90.4% for the convective target locations to 65.3% on day-1 and finally reduces to 4.8% on the 5th day of trajectory. The deep-convective cloud cover, being a subset of high cloud dominate on day-1 and then reduces to  $\sim 0.1\%$  from day-2 onwards. The cirrus cloud cover reaches its maximum (16.4%) on day-1 following the decrease in deep-convective clouds and then decreases monotonically on the rest of the days (9.7% on day-2 to 4.1% on day-5). The behavior of cirrostratus follows the deep-convective clouds with maximum value on the convective target locations (31.4%), and gradual decrease afterwards with 25.0% on day-1 to 0.6% on day-5. The relation between cirrus and cirrostratus growth is consistent with the findings of Luo & Rossow (2004) which are discussed in detail in section 5.3.2.

### 5.3.2 Variation of cirrus and cirrostratus clouds along forward trajectories

The histogram transition analysis presented in section 5.3.1 shows the cloud distribution properties of the deep-convection to cirrus transition behavior. In order to characterize this behavior in terms of individual cloud amounts for the trajectory path, the average variation of cloud properties for the observations and the model output are compared.

In this study, the evolution of cirrus is assessed by following the movement of the air leaving the vicinity of convective systems and computing the variation of cirrus along the forward air trajectories. Assuming the cloud amount to be a good indicator of the life cycle of clouds, the different cloud types as a function of time over forward trajectories are averaged.

The Lagrangian trajectory analysis for the model output as well as the ISCCP observations show that the decay of deep-convection is immediately followed by the growth of cirrostratus and cirrus, and then the decay of cirrostratus is followed by the continued growth of cirrus. Cirrus properties continuously evolve along the trajectories as they gradually thin-out and move to the lower levels. Note that since the model output is set to retrieve all the time steps in the ISCCP simulator, the cloud amount is cumulative and free of day-light effect.

Figure 5.10 shows the averaged day-time cloud properties for deep-convective, cirrostratus and cirrus clouds as a function of time from last convection along forward trajectories from the winter month (January 2002). These properties are compared for the model derived ISCCP simulator output and the ISCCP observations. The cirrostratus cloud amount together with the deep-convective cloud amount in model and observations is shown in figure 5.10(a), and similarly, the cirrus cloud variation relative to deep-convective clouds in time is shown in figure 5.10(b). The steep curve for deep-convective clouds for observations (dashed red line) and in the model (solid red line) in figures 5.10(a),(b) show the early decay of thick convective clouds within 1 day from the convective event. The detrainment from the deep-convective clouds contribute to the formation of cirrus clouds which also gradually decay to lower levels from day-1 onwards as seen in figure 5.10(b). The detailed 3-hourly variation of cirrus cloud amount shows that the deep-convection decay is immediately followed by the growth of cirrus (explained later in subsection 5.3.3). The cirrostratus decay follows the deep-convection but remain constant ( $\sim 2\%$ ) after the 2nd day onwards for the ISCCP observations (figure 5.10(a)). In the model output, similar behavior of cirrostratus is seen together with the deep-convection decay, however the growth of cirrostratus (figure 5.10(a)) is not as clear as cirrus in figure 5.10(a). The 3-hourly variation of model output for deep-convective, cirrus and cirrostratus clouds is explained in detail in subsection 5.3.3, where the initial peaks of cirrus and cirrostratus clouds within day-1 (originated via immediate convective detrainment) are shown. The analysis for ISCCP observations do not agree completely with those processed by Luo & Rossow (2004), since Luo & Rossow (2004) used the special dataset for IR retrieved ISCCP radiance measurements at 11 and 12  $\mu\text{m}$  (making the day-night data time series for ISCCP clouds). More details on these differences are presented in subsection 5.3.3.

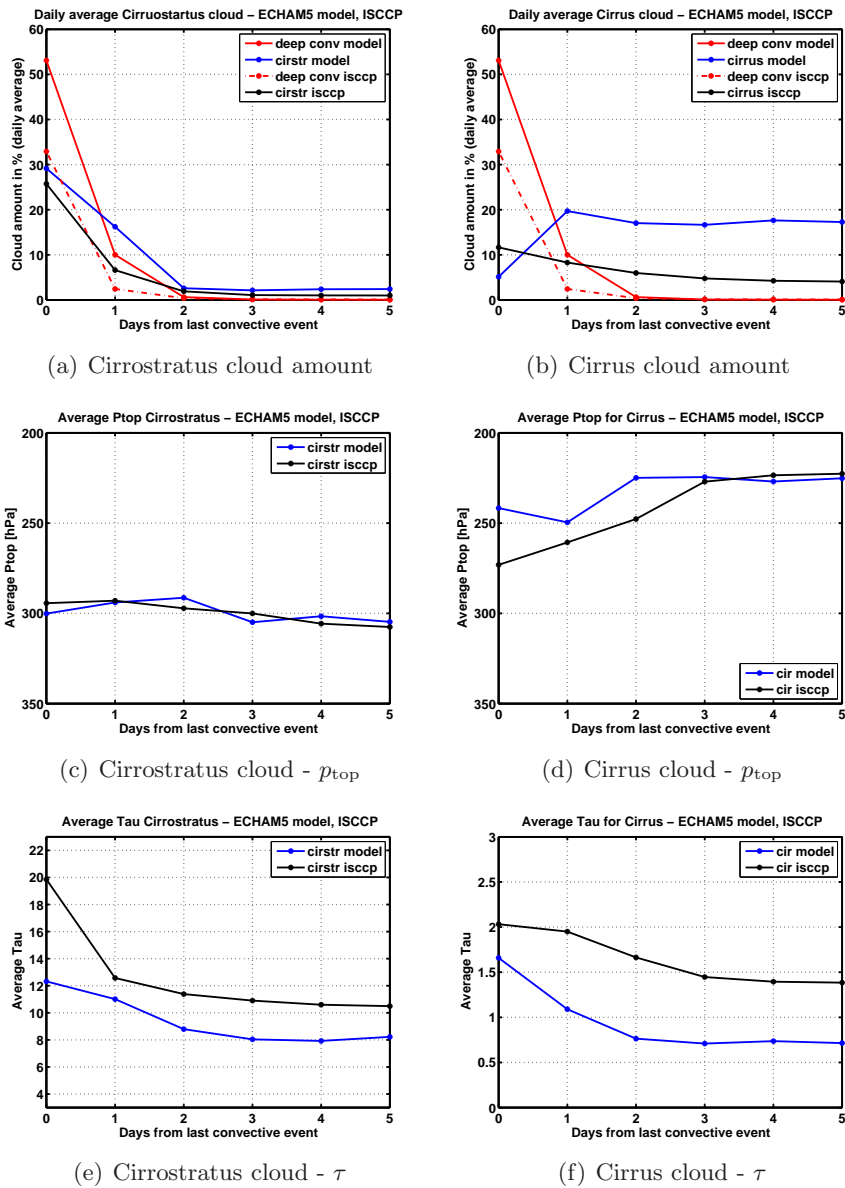


**Figure 5.10**— Average cloud properties for ECHAM5 model output compared to ISCCP observations for January 2002. The individual cirrostratus and cirrus cloud amounts are shown in reference to the deep-convective clouds for model and ISCCP observations in the top panel of subfigures. The daily average cloud top pressure and optical thickness values for cirrostratus and cirrus clouds are shown for model and ISCCP observations. The respective legend indicates the cloud types for model and observations.

Also evident from figure 5.10(a) and figure 5.10(b) is that the cirrus cloud amount decreases more slowly as compared to cirrostratus cloud amount, which means that the  $e$ -folding time (Luo & Rossow, 2004) is longer than 5 days for cirrus, and it is

about 1-2 days for cirrostratus clouds. This finding is consistent with the findings of Jin (1998), who argues that cirrus and cirrostratus are most likely produced and maintained by different processes. That means that convective detrainment is probably not the only source for maintaining cirrus, other dynamic processes (for e.g., vertical transport of water vapor by waves or large-scale uplifting) also exist that could be responsible for their formation and maintenance (Jin, 1998).

The daily averaged distribution for observational as well as model cloud top pressure ( $p_{\text{top}}$ ) for cirrostratus clouds with respect to time from the convective event for all the trajectories is shown in figure 5.10(c) for January 2002. The winter month observational cirrostratus clouds very slightly increases in  $p_{\text{top}}$  from 295 hPa on day-1 to 307 hPa on day-5. However, the cirrostratus behavior is quite different from cirrus clouds even when both of these clouds occur at similar cloud top pressure ranges. The observational cirrus top pressure (shown in figure 5.10(d)) drops (from 271 hPa to 264 hPa) during day-1, further reduces to 225 hPa on day-3 and becomes 221 hPa towards day-5. Hence with time, the cirrus clouds move to higher levels in height whereas cirrostratus move towards lower height levels in the ISCCP observations.

The model derived daily averaged  $p_{\text{top}}$  distributions show a similar transition behavior as seen in the observations. As seen in figure 5.10(c), the winter month cirrostratus clouds drop in  $p_{\text{top}}$  from 300 hPa on convective targets to 285 hPa on day-1 towards 281 hPa on day-2, and then increases further on with time with 300 hPa on the last day of trajectory path. For the model, the cirrus top pressure on convective targets increase from 244 hPa to 253 hPa, then drops sharply (from 253 hPa to 220 hPa) during day-1 and then increases towards day-4 (223 hPa), and finally reducing to 219 hPa on day-5 (as seen in figure 5.10(d)). Hence, similar to the observational behavior, the cirrus clouds tend to move upwards and the cirrostratus clouds move downwards with time.

The evolution for the cloud optical thickness ( $\tau$ ) for cirrostratus and cirrus clouds for the observationa and the model are shown in figure 5.10(e) and figure 5.10(f), respectively. As seen in the respective figures, the cloud optical thickness gradually decreases over time both for cirrus and cirrostratus clouds in the observations as well as in the model output. This trend is consistent with the general circulation cloud formation and dissipation. The clouds remain thick and high on day-1 of trajectory path and then cloud  $\tau$  decreases as the clouds thin-out and move to lower levels over the next days.

### 5.3.3 Comparison of hourly variation of cloud transitions

In this work, the standard visible spectrum (day-time) ISCCP-D2 satellite data was used to compare the model simulated deep-convection and cirrus transitions over time. The Lagrangian trajectory analysis is performed on a cumulative time variation basis to capture the advection of deep-convective clouds as they detrain to thin cirrus and cirrostratus over time. The ISCCP day-time data does not suit to fulfill the criteria of continuous observations over the trajectory path as it moves along time. The comparison of the daily average cloud amounts of the ISCCP

observations over the trajectory paths to the model do not represent the detailed growth-decay cycle of cirrus and cirrostratus clouds. Moreover, the time details which show the relationship between cirrus and cirrostratus are not evident from the ISCCP day-time data (figure 5.10(a) and figure 5.10(b)).

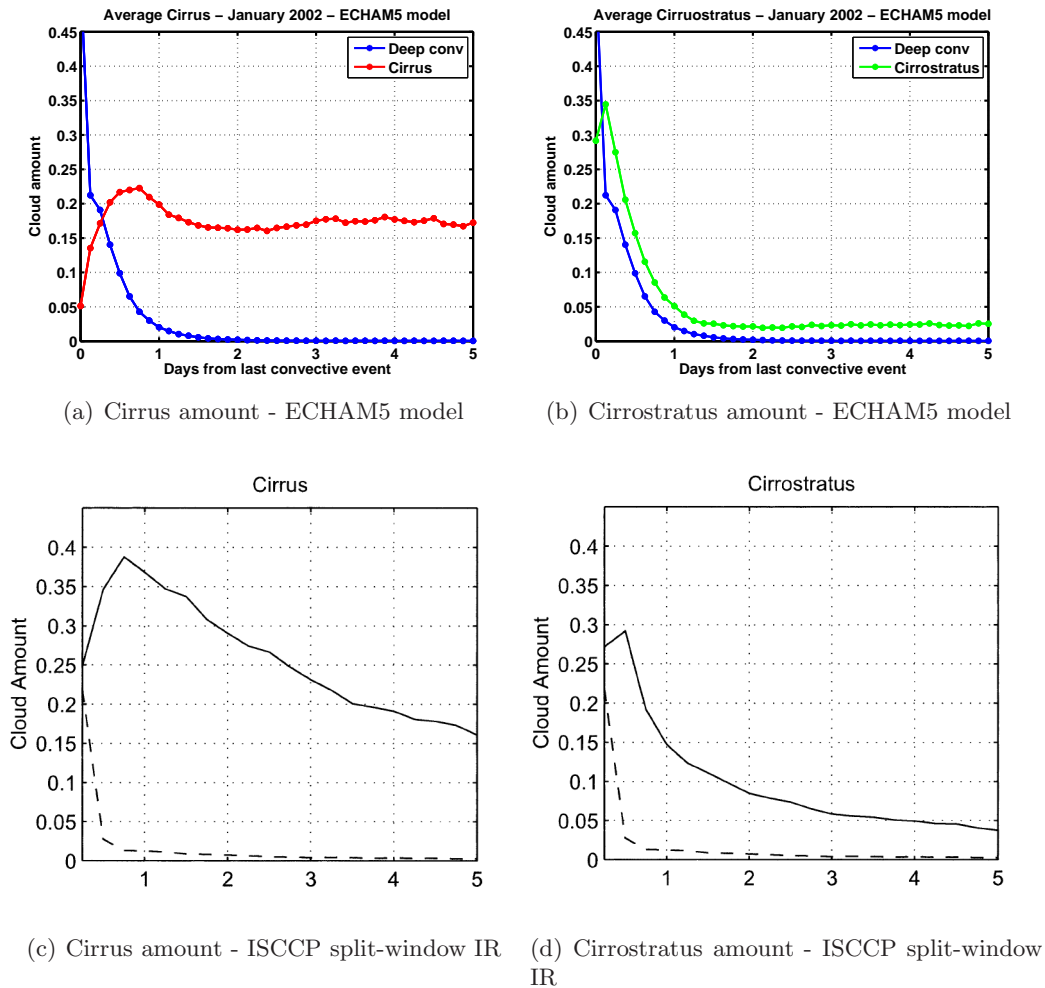


**Figure 5.11**— Average cirrus and cirrostratus cloud properties as function of time (days) after after the convective event for ECHAM5 model and ISCCP split-window IR retrieved data from Luo & Rossow (2004). The dashed line in (c) and (d) represent the deep-convective cloud amount in the ISCCP split-window IR data (Luo & Rossow, 2004).

Luo & Rossow (2004) show the Lagrangian trajectory analysis over ISCCP satellite cirrus data set derived from only infrared observations by building upon the existing ISCCP-DX data and TIROS-N Operational Vertical Sounder (TOVS) products. This cirrus data set provided continuous coverage throughout each day by using two radiances from the infrared window spectrum at 11 and 12  $\mu\text{m}$  (split-window method). The main reason for using the refined ISCCP data was to augment the

ISCCP analysis of cirrus during night, when the visible channel becomes unavailable for retrieving cloud optical thickness. More details about the ISCCP split-window day-night data can be found in Luo & Rossow (2004)

The model version used in this study is set up so that the simulated cloud cover diagnostics also include the nighttime data. This helps in achieving the continuously simulated ISCCP cloud types. Hence, the model simulated cloud properties are directly comparable to the day-night infrared ISCCP split-window observations used by Luo & Rossow (2004). The details of this comparison are shown in figure 5.11, where 3-hourly average cloud amounts for deep-convection, cirrus and cirrostratus over the Lagrangian trajectories are shown as a function of time. The model simulated cirrus and cirrostratus clouds together with deep-convective clouds are shown in figure 5.11(a) and figure 5.11(b) respectively. The results of cumulative day-night average cloud cover derived by Luo & Rossow (2004) are shown in figure 5.11(c) and figure 5.11(d) for cirrus and cirrostratus clouds respectively.

The simulated cloud cover from the ECHAM5 model agrees reasonably with the infrared ISCCP day-night data by Luo & Rossow (2004). The cirrus clouds maximum is attained at day-1 from where the cirrus cloud cover decreases over time (figure 5.11(a)). On the other hand, the cirrostratus clouds are at maximum on the convective target locations (same as the deep-convective clouds), and gradually reduce to almost  $\sim 0.1\%$  from day-2 onwards as seen in figure 5.11(b).

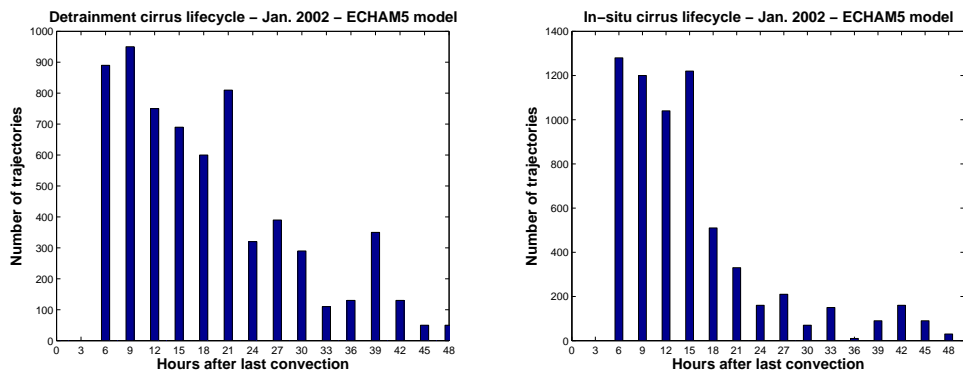
As illustrated in figure 5.11(a) and figure 5.11(b), the decay of deep-convection is rapid (6 - 12 h) and is associated with the growth of both cirrostratus and cirrus. The time and spatial scales of the transition from convection to cirrostratus (probably as convective detrainment) are about 6 h and 200 km (based on average wind speed (Luo & Rossow, 2004)) respectively. The cirrostratus amount peaks in the first 3 to 6 hours on day-1 before it starts to detrain over next days (see figure 5.11(b)). The decay of cirrostratus is then accompanied by the continued growth of cirrus, indicating a decay of cirrostratus into cirrus. From the decay of cirrostratus, it takes another  $\sim 6-12$  hours for the cirrus amount to reach its peak, shown in the figure 5.11(a). This behavior is consistent in the winter as well as the summer month of analysis (not shown), and agrees well to the findings of Luo & Rossow (2004).

The relatively rapid decay of cirrostratus over about 12 hours to 1 day downstream of convection suggests a loss of cloud water mass. As shown in Luo & Rossow (2004), the cirrostratus most likely form by the convective detrainment and/or as part of an associated mesoscale circulation and contain a much larger water mass (and larger particles than cirrus) and consequently have much larger sedimentation mass flux (Luo & Rossow, 2004).

Cirrostratus being at a lower pressure (higher level) than cirrus suggests that the transition from cirrostratus to cirrus is accompanied by a gradual decrease in cloud-top height. The evolution of cirrus properties also indicates that cirrus tend to thin-out and move to the lower levels, as air moves away from convective regions.

## 5.4 Detrainment and in-situ cirrus life-cycle analysis

Figure 5.11 and its subplots provide us a general sense of average tropical cirrus evolution along forward trajectories in time. Nevertheless, they are not enough to characterize the cirrus life cycle because compositing over many trajectories smears out the detailed life cycle of each individual trajectory. Although the composite picture shows that it takes a little more than 5 days for cirrus amount to  $e$ -fold (figure 5.11(a)), an individual cirrus system may have a much shorter life cycle. Therefore, in this section a different approach is adopted toward characterizing tropical cirrus life-time by collecting statistics from each individual trajectory. This is done only for the model output, since the ISCCP observations are not continuous and are available for day-time only.



(a) Detrainment cirrus lifecycle - ECHAM5 model (b) In-situ cirrus lifecycle - ECHAM5 model

**Figure 5.12**— Detrainment and In-situ cirrus life cycle for present day ECHAM5 model with climatological SST - January 2002. The plots show the histograms for number of trajectories which encounter detrainment and in-situ cirrus for their duration over the trajectories.

It is assumed here that the cirrus life-cycle (formation followed by decay) is characterized along a particular trajectory by the systematic variation of cirrus cloud amount over time. Two types of tropical cirrus are considered based on their relationship to convective systems, namely the detrainment cirrus and in-situ cirrus. Detrainment cirrus are the ones derived directly from detrainment of deep-convective clouds, whereas in-situ cirrus clouds are those generated by other large-scale dynamic processes (for e.g., vertical transport of water vapor by waves, large-scale uplifting etc.). The primary distinction criteria for defining detrainment and in-situ cirrus is to categorize their life-cycle based on when the cirrus cloud amount is maximum within a particular trajectory path. The life-cycle for detrainment cirrus is defined by a monotonic decrease of cirrus amount along a forward trajectory. Hence, last convection becoming some cirrus, further becoming maximum cirrus and then decreasing to minimum cirrus over time. The length of this sequence defines the

detrainment cirrus life-cycle. It is considered that the cloud amount is minimum when it reaches to 20% of the maximum cirrus cloud amount over an individual trajectory (Luo & Rossow, 2004). For defining the in-situ cirrus, the sequence of appearance of cirrus cloud amount is seen at least after 1st day of convective event. The cirrus observed at this time, should increase to maximum cirrus and then decrease to minimum cirrus amount over time. The requirement that the trajectory air parcel encounter clear skies after convection (1 day or more) ensures the separate evolution of the in-situ cirrus.

All the trajectories are checked for the occurrence of detrainment cirrus (cirrus cloud amount maximum on day-1 and decreases further on) and for in-situ cirrus (cirrus cloud amount increasing after day-1, reaching maximum and decreases further on). Figure 5.12(a) shows the histogram of cirrus lifetimes for detrainment and figure 5.12(b) shows the in-situ cirrus. The histogram distribution defines the life-cycle for the respective cirrus cloud type. The life-cycle of detrainment cirrus is about  $20 \pm 15$  hours (compared to the results of Luo & Rossow (2004) where they derive the detrainment cirrus life cycle as  $30 \pm 16$  hours). For in situ cirrus, the lifetime is about  $17 \pm 13$  hours (compared to the results of Luo & Rossow (2004) where they derive the in-situ cirrus life cycle as  $19 \pm 17$  hours).

Because relatively large areas (2.5 by 2.5 degree) are considered, the definition of *zero cirrus* needs to be relaxed from absolute zero; otherwise, very few samples of distinct cirrus life cycle sequences occur. In practice, zero cirrus is defined as 1/5 of the maximum cirrus cloud amount along the life-cycle sequence. For example, when a trajectory initially overcast with cirrus clouds decays below 20%, this is considered as the end of the life cycle. But if the maximum cirrus amount along a selected trajectory is only 20%, then it has to drop below 4% to end the life cycle.

## 5.5 Cirrus clouds in a warmer climate

In order to evaluate the model sensitivity in terms of cloud transitions, an idealized climate change simulation with SST increased by a uniform 2 K (Cess et al., 1990) is performed. The other model conditions remain similar to the present day model run with climatological SST.

The Lagrangian trajectories for the perturbed model runs are created using the model wind fields within the HYSPLIT model (procedure explained in detail in section 5.3). Cloud transition histograms for the perturbed model runs are shown in figure 5.13. The sequential plots show the transition of deep-convective clouds (figure 5.13(a)) to cirrostratus clouds after day-1 (figure 5.13(b)) and finally to thin cirrus on the following days as seen in figures 5.13(c) to 5.13(f).

Table 5.3 lists the average histogram values starting from the convective targets and following to next 5 consecutive days. For the monthly analysis performed, the total cloud cover for trajectories in the perturbed climate run drops from 99.9% in the convective source regions to 10.3% on the 5th day in the tropics. Hence very little total cloud remains in tropics since the trajectories move towards the extra-tropics

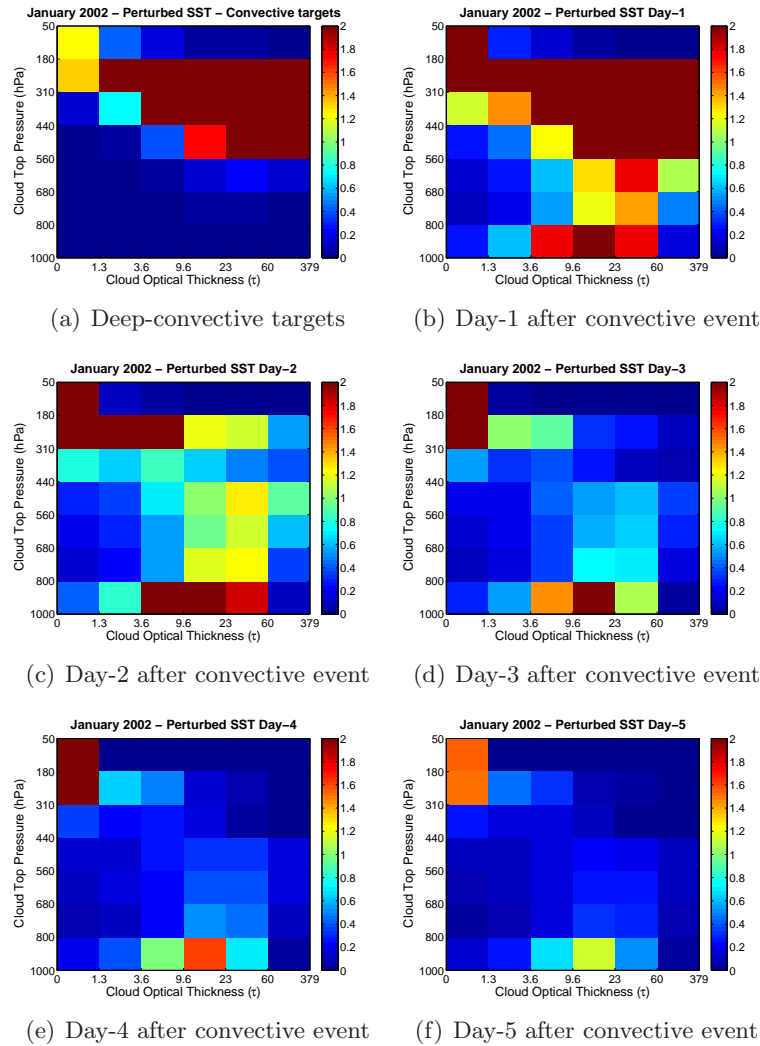


**Figure 5.13**— Lagrangian transition histograms for +2 K perturbed SST model run - January 2002. Simulated ISCCP histograms for each day are computed over averaged trajectories starting from deep-convective targets and traveling for next 5 days after the convective event.

(shown in trajectory path snapshots in figures 5.3, 5.4, 5.5 and 5.6). The high cloud cover drops down from 90.7% for the convective target locations to 60.5% on day-1 and finally reduces to 4.6% on the 5th day of trajectory. The deep-convective cloud cover, being a subset of high cloud dominate on day-1 and then reduces to  $\sim 0.1\%$  from day-2 onwards. The cirrus cloud cover reaches its maximum (16.9%) on day-1 following the decrease in deep-convective clouds and then decreases monotonically on the rest of the days (12.3% on day-2 to 3.9% on day-5). The behavior of cirrostratus follows the deep-convective clouds with maximum value on the convective target locations (30.5%), and gradual decrease afterwards with 21.4% on day-1 to 0.6% on

day-5.

Time from last convective event	ISCCP cloud types				
	Total cloud	High cloud	Deep-conv. cloud	Cirrostratus cloud	Cirrus cloud
Deep-conv. targets	99.8	90.7	53.1	30.5	7.0
Day-1	88.4	60.5	22.1	21.4	16.9
Day-2	41.4	20.2	2.5	5.3	12.3
Day-3	22.8	10.2	0.5	1.8	7.7
Day-4	14.8	6.5	0.1	1.0	5.3
Day-5	10.3	4.6	0.0	0.6	3.9

**Table 5.3**— Mean values of cloud amount from perturbed SST model run - January 2002

The ISCCP histograms of the cloud transitions in perturbed climate model run show a slight increment in the cirrus cloud amount on day-2 and -3 (figure 5.13(c) and figure 5.13(d), respectively) in comparison to the present day model runs with climatological SST (figure 5.9(c) and figure 5.9(d), respectively). However, more detailed comparison of Lagrangian transitions for different ISCCP cloud categories of the simulated ISCCP clouds for the present day climate (climatological SST) and for the warmer climate (+2 K perturbed SST) runs is discussed in the following section.

### 5.5.1 Comparison of cloud transitions for present and perturbed climate

Similar to the cloud amount variation for the present day model, the perturbed runs also show a consistent transition behavior for deep-convective detrainment followed by evolution of cirrostratus and cirrus clouds in time. In all the comparison plots shown in the section, the present day climate runs are shown with blue, whereas the perturbed +2 K warmer SST runs are shown in red color. The cloud amount variation is shown in absolute cloud cover fraction values.

Figure 5.14 shows the daily average cloud properties for the total cloud cover and the high cloud cover over the Lagrangian trajectories. The total cloud cover (TCC) amount variation for the two model versions shows that the daily average total cloud amount for warmer climate decreases on 1st day after the convective event (figure 5.14(a)). The total cloud fraction for the perturbed climate increases later on day-2 (by  $\sim 8\%$  in absolute cloud fraction) and day-3 (by  $\sim 3\%$  in absolute cloud fraction). The high clouds (HCC) show a similar variation behavior as the total clouds in the warmer climate. As seen in figure 5.14(b), the high clouds decrease on day-1, and then increase on day-2 and -3 by  $\sim 7\%$  and  $\sim 3\%$ , respectively in the warmer climate compared to the control climate.

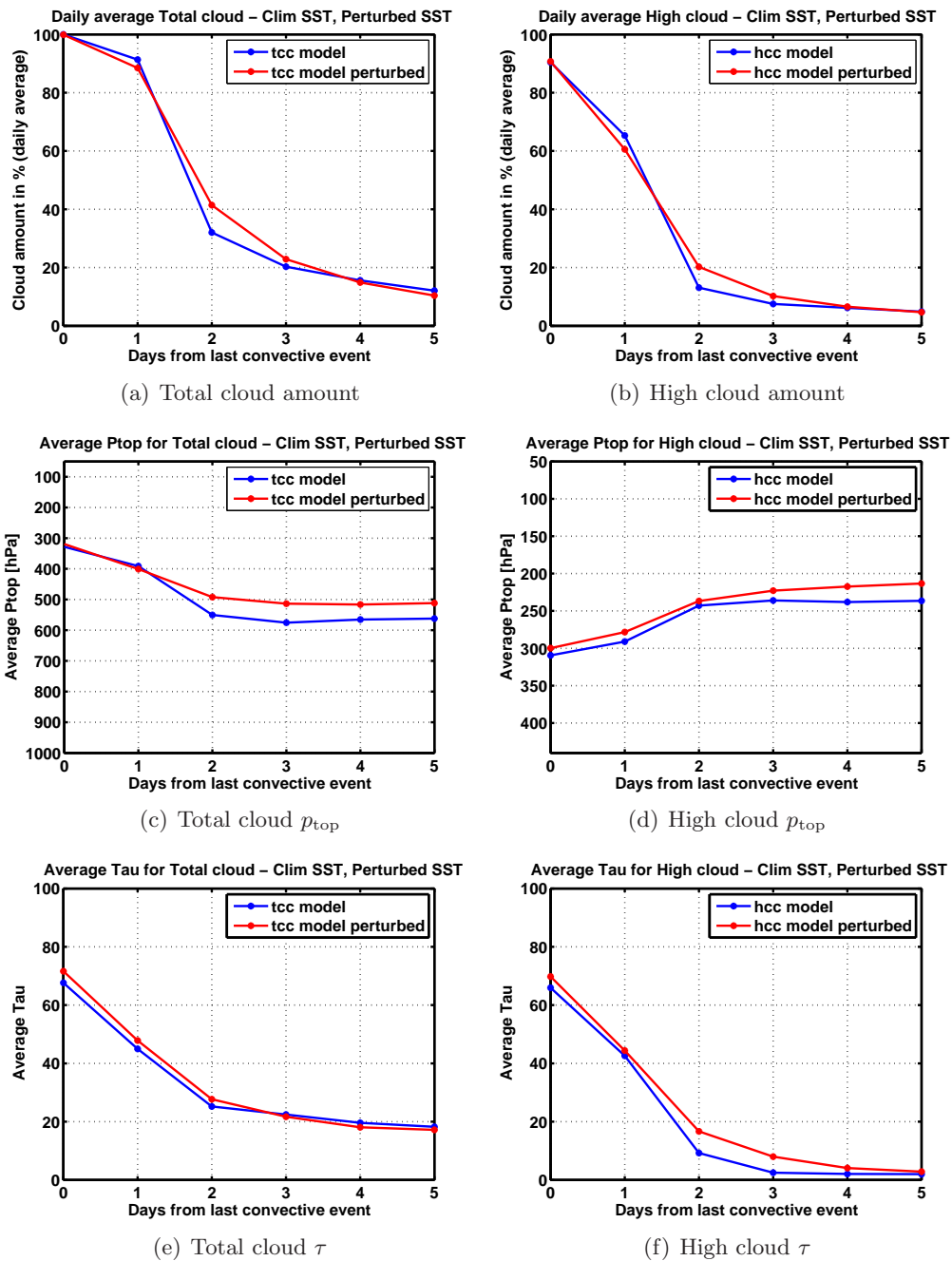


**Figure 5.14**— Comparison of average cloud properties for Total cloud cover (TCC) and High cloud cover (HCC) for the present day ECHAM5 model output compared to the warmer climate run (perturbed SST) - January 2002. The present day model is shown in blue, perturbed climate in red in all the sub-figures.

The total cloud cover tends to be higher in the warmer climate in comparison to the present day climate, as seen in figure 5.14(c), where the daily average cloud top pressure for TCC reduces by  $\sim 50$  hPa on day-2 onwards after the convective event. The optical thickness of the total cloud cover increases slightly on the convective targets ( $\tau$  for TCC becomes 56 in warmer climate from 54 in the present day) as well as day-1. However, from day-2 onwards the TCC optical thickness does not show a significant change in the present and the perturbed climate model runs figure 5.14(e).

Similar to the TCC, the perturbed model HCC also show a decrease in the cloud top pressure (figure 5.14(d)), showing that the high clouds move higher from day-2 onwards after the convection in the atmosphere in the warmer climate. Moreover, these high clouds also tend to be thicker as seen in figure 5.14(f), where the cloud optical thickness is considerably increased for high clouds on day-2 ( $\sim 2$  times of the optical thickness in the present day climate) onwards.

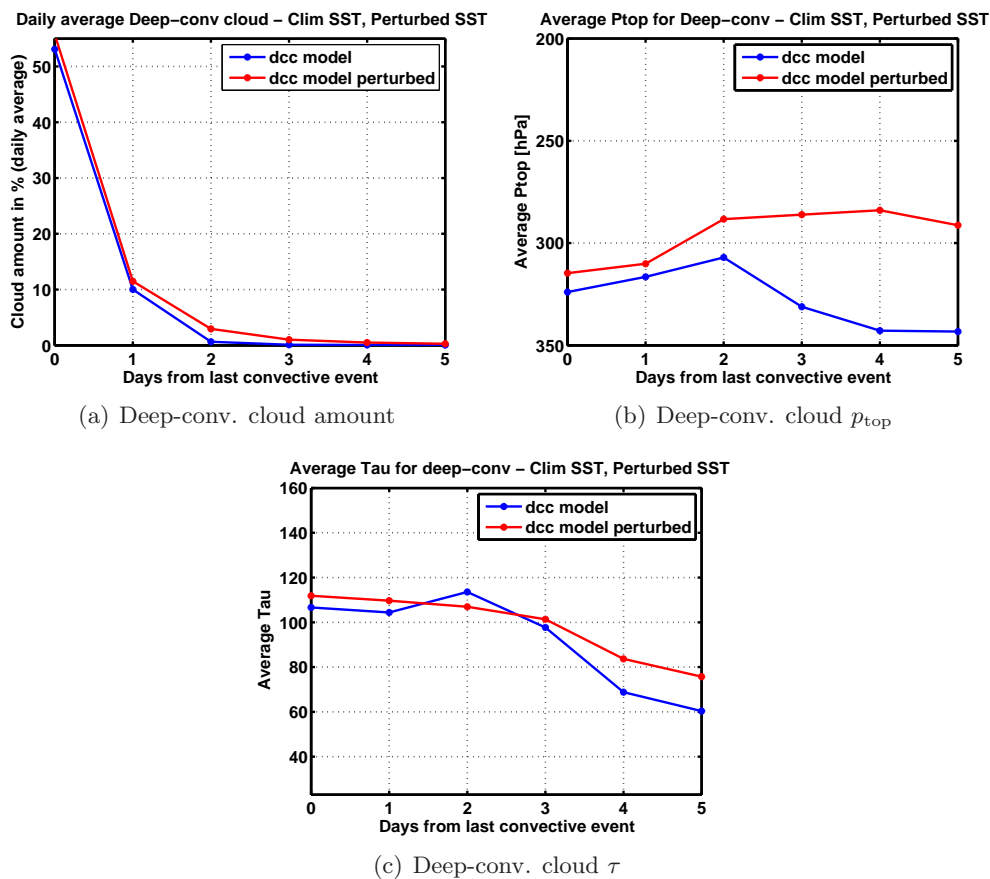


**Figure 5.15**— Comparison of average cloud properties for Deep-convective cloud cover for the present day ECHAM5 model output compared to the warmer climate run (perturbed SST) - January 2002. The present day model is shown in blue, perturbed climate in red in all the sub-figures.

The cloud transitions for the deep-convective clouds are shown in figure 5.15. An increase of  $\sim 2\%$  in the convective cloud amount in the perturbed climate run for day-2 after the convective event can be observed in figure 5.15(a). The comparison of the present day and perturbed climate runs show that the deep-convective clouds are higher in the atmosphere, as well as thicker for the warmer climate (except for day-2, see figure 5.15(c)).

Since the high clouds show an increase in the optical thickness in the perturbed climate on day-2 (figure 5.14(f)) and the deep-convective show a rather decrease on the same day, it implies that other clouds in the high cloud category (i.e., cirrostratus and cirrus) cause this change in the increased optical thickness of high clouds.

The cloud top pressure for cirrostratus as well as cirrus clouds show an increase in the warmer climate from day-2 onwards (figure 5.17). The cirrostratus cloud variation shows that the cirrostratus in the warmer clouds are thicker specially on day-2 and onwards after the deep-convective event as seen in figure 5.18(a). The cirrus clouds on the other hand show a same behavior in the present day and warmer climate run, with a slight decrease on day-4 and -5 in the warmer climate (figure 5.18(b)).

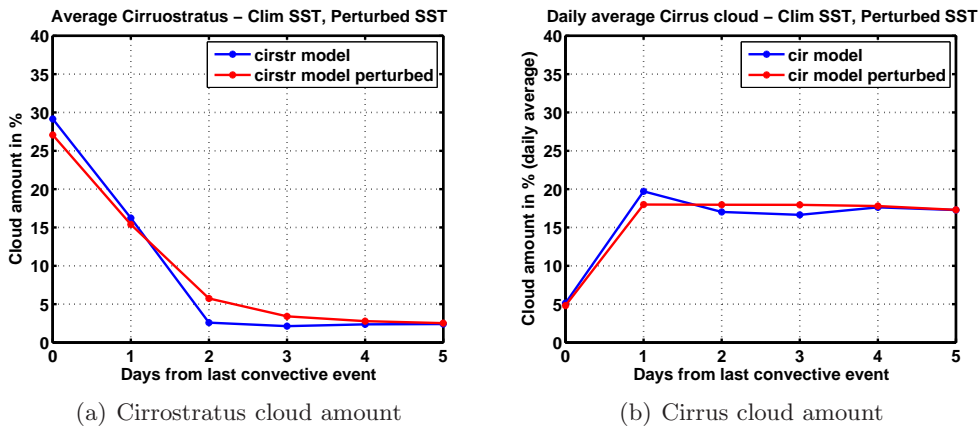


**Figure 5.16**— Comparison of daily average cloud amount for cirrostratus and cirrus clouds in the present day ECHAM5 model output compared to the warmer climate run (perturbed SST) - January 2002. The present day model is shown in blue, perturbed climate in red in all the sub-figures.

The perturbed climate model runs show a stronger convection and hence a stronger hydrological cycle with an increased large-scale precipitation as well as convective precipitation. As seen in figure 5.19(a), the large-scale precipitation in the perturbed model increases on day-1 and -2 after the convective event, then remains similar to the precipitation in the present day model. Similar behavior for convective precipitation can be seen in figure 5.19(b). The relative humidity averaged over a range of 200 to 500 hPa is compared for the present and the perturbed climate and shown in figure 5.19(f). The increased precipitation on day-1 and -2 after convection leads to the reduction of the relative humidity in the upper troposphere in the

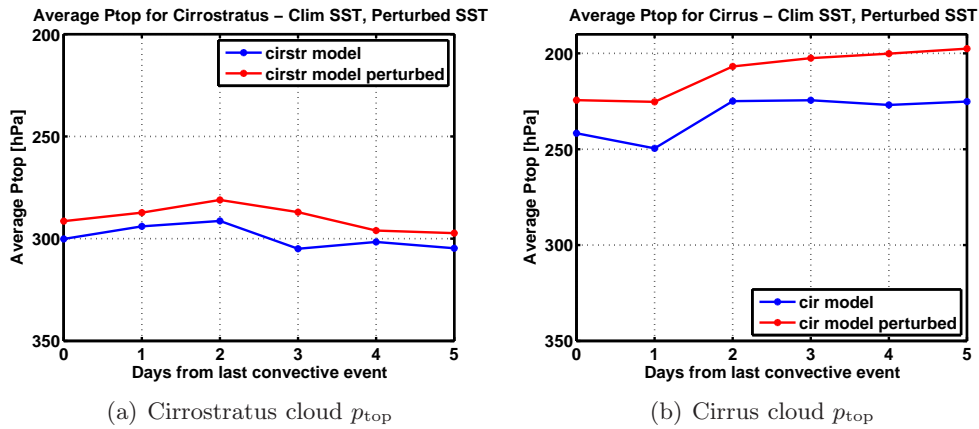


**Figure 5.17**— Comparison of daily average cloud top pressure ( $p_{top}$ ) for cirrostratus and cirrus clouds in the present day ECHAM5 model output compared to the warmer climate run (perturbed SST) - January 2002. The present day model is shown in blue, perturbed climate in red in all the sub-figures.

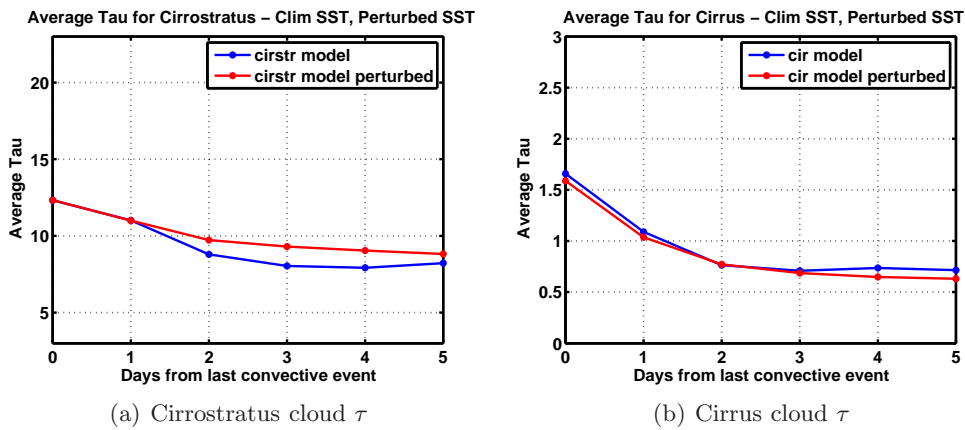


**Figure 5.18**— Comparison of daily average cloud optical thickness ( $\tau$ ) for cirrostratus and cirrus clouds in the present day ECHAM5 model output compared to the warmer climate run (perturbed SST) - January 2002. The present day model is shown in blue, perturbed climate in red in all the sub-figures.

perturbed climate runs in comparison to the present day climate.

The Lagrangian transitions of the cloud forcings in the model show an increase in the short wave forcing (solar spectra, figure 5.19(c)) as well as in long wave (terrestrial spectra, figure 5.19(d)) in the perturbed model runs compared to the present day climate, specially on day-2 after the convective event. The global average cloud radiative forcing values are indicated in the respective figures for the present day as well as the perturbed climate. Since the cirrostratus cloud amount increases

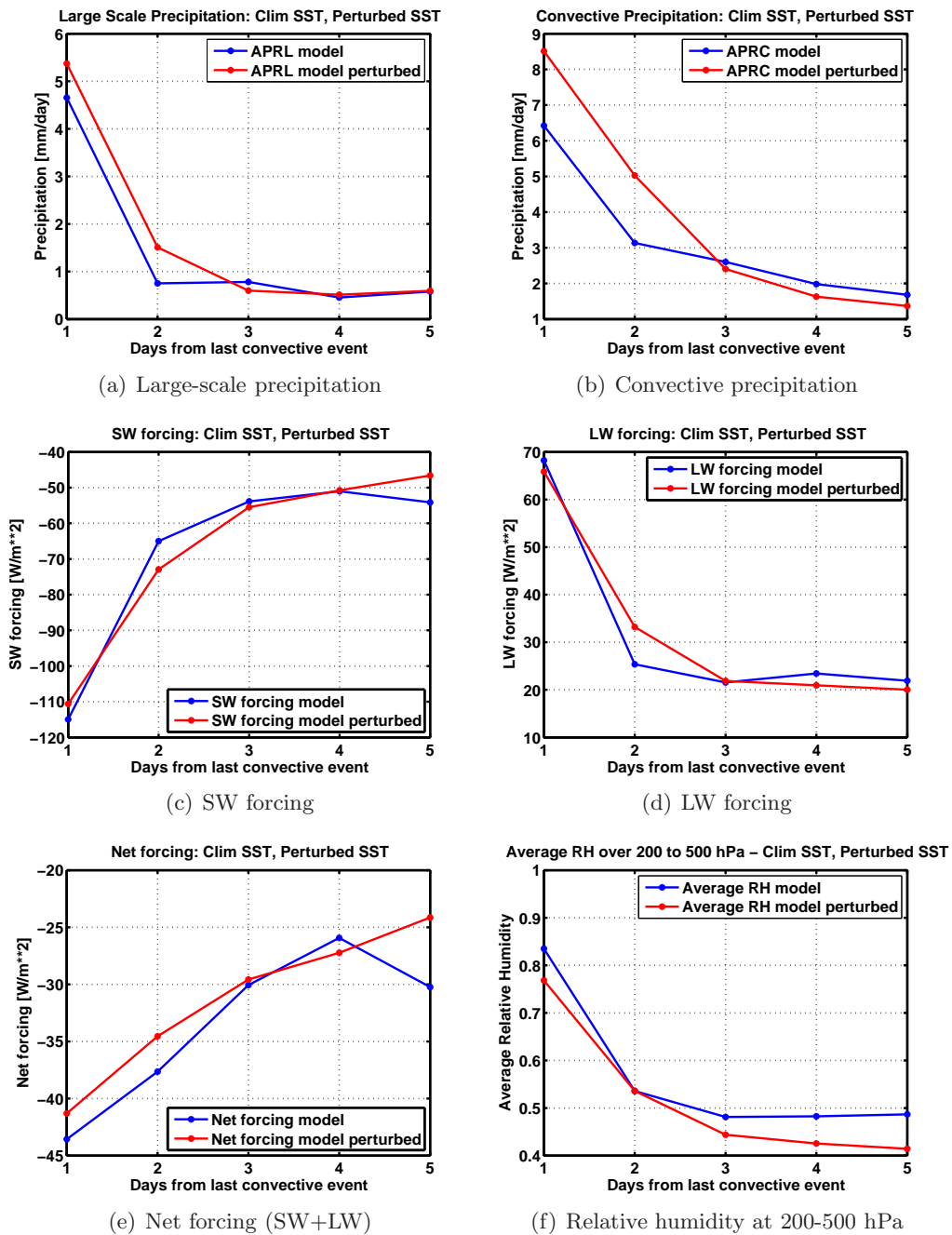


**Figure 5.19**— Model variables (large-scale precipitation (APRL), convective precipitation (APRC), cloud forcings and relative humidity) for present day ECHAM5 model (climatological SST) compared to the warmer climate run (perturbed SST) for January 2002. The present day variables are shown in blue and the perturbed climate variables are shown in red color.

and hence the green house effect, the net forcing comes out to have a positive feedback on the climate i.e., less cooling due to convection in the warmer climate.

## 5.6 Summary and conclusions

The life cycle and evolution of tropical cloud systems are examined by analyzing ISCCP satellite-derived cloud data and ECHAM5 ISCCP simulator model output in a Lagrangian framework. In order to compare the cloud transition differences in a warmer climate, the ECHAM5 climate model is used with an idealized warming of +2 K perturbed SST to compare with simulations with present day climatological SST.

Despite similar geographical patterns of cirrus and deep-convection in the monthly mean maps (Figures 5.1 for January and 5.2 for July), they may not be as closely related in an instantaneous sense when tracking the origin and evolution of these two types of clouds. The Lagrangian trajectory analysis over 5 consecutive days after deep-convective events shows that the decay of deep-convection is followed by the growth of cirrostratus and cirrus and then the decay of cirrostratus is followed by the continued growth of cirrus. Cirrus properties continue to evolve along their trajectories as they gradually thin-out and move to the lower levels. These detrainment cirrus systems last for  $20 \pm 15$  hours.

An estimate of cirrus particle lifetimes, however, gives a range from 0.8 to 8 hours, depending on particle terminal fall velocity (Heymsfield, 2003). The difference suggests that there are at least transient upward motions that oppose particle sedimentation to maintain tropical cirrus and to keep them from dissipating for much longer than the particle lifetime. Consequently, cirrus can advect over large distances, about 600-1000 km, during their lifetimes. For most GCMs, this distance spans many grid boxes requiring that the water vapor and cloud water budgets include an advection term. These results concerning cirrus evolution and life cycle variation provide the observational basis for evaluating and improving modeling of convection, detrainment and cirrus life cycle in GCMs. Comparison of the geographical patterns of cirrus between a model and observations is not a very informative test of the model because it cannot distinguish between the causes for disagreements, which might involve other factors, such as the model treatment of deep-convective anvils and the large-scale circulation (Salathe & Hartmann, 2000). Comparison of cirrus evolution and life cycle in a Lagrangian framework, on the other hand, provides a way of focusing on the formation-decay processes that control the cirrus properties.

The model cloud transition histograms for 5 days after the convection in comparison to the ISCCP observations show that the model convection is stronger. High thick clouds (deep-convective clouds in the ISCCP classification, figure 2.2) continue to persist after 1 day (remains 50% of the deep-convective cloud amount on convective targets). Thus, more water vapor is detrained in the upper troposphere to form too many, too thick and too high cirrostratus clouds. The ISCCP observations show a rapid decay of deep-convective clouds, where day-1 after the convective event shows

only 20% of the deep-convective clouds. Hence, the convective clouds have a larger cloud amount and have a larger life time in the ECHAM5 model compared to the ISCCP observations in a Lagrangian framework.

Detrainment cirrus are distinguished from in situ cirrus in this study. The latter have been identified in the trajectory analysis by defining the cirrus which are created independent of the convective detrainment. These in-situ cirrus last for  $17 \pm 13$  hours. The different generating mechanisms for these two types of cirrus suggest the possibility that they may not respond in the same way to a changing climate, producing different feedbacks. Detrainment cirrus have a strong connection to deep-convection, being produced as the decay products of the convective anvil clouds. A change of this type of cirrus with climate should be understood as part of the study of how convection changes with climate. But in-situ cirrus are not directly connected with convection and can be produced by other dynamical processes, such as small-scale turbulent motions, gravity waves, large-scale waves or episodes of large-scale uplift; their response to a changing climate therefore depends on how these other dynamic processes change.

The changes in the convective cloud transitions for the warmer climate model runs show that the amount of cirrostratus clouds increases in the warmer climate. The model cloud diagnostics from the ISCCP simulator suggest that the cirrostratus clouds tend to be thicker and higher in the atmosphere in the perturbed SST model run. The cirrus clouds also increase in the height and cloud amount (on day-2 and 3) whereas their optical thickness remains similar to the present day (climatological SST) simulation. Since the high cloud amount increases and goes higher in the atmosphere in the perturbed or warmer climate, it implies an increased longwave cloud radiative effect that is more prominent than the increased shortwave effect (due to slight changes in cloud optical thickness). This leads to less cooling or a positive feedback from convective detrainment in the warmer climate.

The transition behavior of the standard model variables such as precipitation and cloud forcings over the Lagrangian trajectories are examined to understand the changes in the warmer climate runs compared to the present day climate. The stronger convection in the warmer climate leads to an increase in large-scale and convective precipitation in the perturbed climate, especially on day-1 and -2. This increment in precipitation leads to drying of upper tropospheric average relative humidity from day-3 onwards for the warmer climate runs.

The shortwave and the longwave cloud forcings increase in the warmer climate leading to an increase in the net cloud radiative forcing (NCRF), leading to a positive feedback of the increased cirrostratus and cirrus clouds from a Lagrangian transition perspective.

## Chapter 6

# Conclusions

Cloud-climate feedbacks have long been identified as the largest source of uncertainty in climate change predictions (IPCC, 2007). Recent comparisons of feedbacks produced by climate models under climate change show that the current generation of models still exhibits a large spread in cloud feedbacks (Bony et al., 2006). Clouds strongly modulate the Earth's radiation budget, and a change in their radiative effect in response to a global temperature change may produce a substantial feedback on the Earth's temperature. The important role of clouds in the climate system is undisputed and many efforts are being undertaken to improve their representation in general circulation models (GCMs). In order to improve models it is first necessary to assess where they fail. A large number of approaches to make such assessments exist, ranging from the analysis of long-term climate simulations to the use of models of specific cloud processes (Jakob & Tselioudis, 2003). In order to have confidence in climate change projections, the importance of evaluating cloud parameterizations and improving the cloud representations in climate models is widely recognized.

It has become quite evident in the last years that one of the key issues in cloud parameterization improvement in the GCMs is to bring together cloud modelers and the cloud observing community. Satellite observations provide the possibility of global observations of cloud properties and hence are useful in model validation. Satellite simulators are a valuable tool in evaluating the model characteristics and hence pin-pointing its deficiencies in direct comparison to the satellite observations.

### 6.1 Main findings of the research

An evaluation of the ECHAM5 general circulation model is performed in the current study by application of the ISCCP (International Satellite Cloud Climatology Project) satellite simulator for detailed cloud diagnostics. The simulator diagnostic sensitivity is tested with two versions of ISCCP simulator within the ECHAM5. The ISCCP simulator version that uses the sub-grid scale variability information in the form of probability density function of total water is compared with ISCCP satellite observations for distribution of various cloud categories. The model evaluation is

performed using different approaches, the short description and major findings of which are shown in next paragraphs.

### 6.1.1 Comparison of global average cloud distributions

The comparison of geographical distributions of ISCCP cloud categories (i.e., total cloud cover, high cloud cover, mid cloud cover, low cloud cover and deep-convective cloud cover) are performed for the model with the observations. The global model output is separated into land and sea areas in order to facilitate the evaluation of characteristic cloud type distributions for land and sea areas. The global average histograms for land and sea areas are analyzed for evaluating the cloud types based on their optical thickness. The main findings show that,

- The ECHAM5 model underestimates the oceanic low clouds in tropics as well as in mid-latitudes.
- The analysis of global sea area histograms reveals that the low oceanic clouds are diagnosed as optically too thick in the model (i.e., more stratocumulus and less shallow cumulus clouds).
- The high and deep-convective clouds are overestimated in the model, particularly in the tropics. Most of the high clouds in the model diagnostics are optically too thin over land as well the sea.
- The mid cloud cover is underestimated by ECHAM5, which implies that the convective clouds in the model do not detrain at mid-levels but rather transport moisture further to form high clouds.

### 6.1.2 Cloud regime definition and their climate change response

A clustering technique for cloud regime separation is adopted to characterize the model behavior in independent cloud regimes based on the approach by Williams & Webb (2009). The Tropics and the extratropics are associated with a large spectrum of cloud types, ranging from low-level boundary layer clouds to deep-convective clouds and anvils. Because of their different top altitudes and optical properties, the different cloud types affect the Earth's radiation budget in various ways. The cloud regimes are hence separated for tropics, ice-free extratropics and snow or ice covered extratropics. Each grid-point of the ISCCP simulator model output is assigned to observed ISCCP cloud clusters defined by Williams & Webb (2009) for computation of the regime mean relative frequency of occurrence (RFO) and net cloud radiative forcing (NCRF) for present day and perturbed climate. The results for the cluster analysis show that,

- For the tropics and the ice-free extratropics, the ECHAM5 model simulates the shallow cumulus clouds as the most frequent cloud regime with qualitative

agreement to the ISCCP observations. Quantitatively, the low clouds are underestimated by the model.

- Optically thick, high-level cloud regime in the extra-tropics, typically associated with the passage of frontal systems, is simulated too frequently in the ECHAM5 model (in agreement with the findings by Williams & Tselioudis (2007) and Williams & Webb (2009)).
- The tropical congestus regime is captured in the ECHAM5 diagnostics but its RFO is underestimated compared to the observations.
- Snow or ice free extratropics show a lack of shallow clouds in the model which is compensated by an overestimation of thin cirrus and mid-level clouds.
- All the tropical cloud regimes show a net positive climate change response to +2 K perturbed sea surface temperature (SST).
- The total climate change response of clouds to SST perturbation, when measured by change in net cloud radiative forcing is dependent on change in net forcing as well as change in RFO.
- The stratocumulus and the stratocumulus/cumulus transition cloud regimes are major contributors for the climate change response due to very strong net forcing for these clouds in the tropics and a respective negative RFO in the warmer climate.

### 6.1.3 Diurnal cycle of clouds

The diurnal cycle of cloud cover for ISCCP category clouds is evaluated for ECHAM5 in comparison to the ISCCP observations. Four tropical areas are selected, each of which comprises of land and sea area. The results show that,

- The total cloud cover diurnal cycle in the observations is dominated by shallow clouds and the model shows a very weak cycle for the low clouds.
- The diurnal cycle evaluation in the ECHAM5 model shows that the deep-convective cloud cover had a very weak cycle except for Indian monsoon region both for model as well as in ISCCP observations.
- The timing of diurnal peak in the model is diagnosed too early ( $\sim 3$  to 6 hours) in comparison to the observations.

### 6.1.4 Convection climate feedbacks

Understanding cloud radiative feedbacks requires an understanding of how a change in climate may affect the distribution of the different cloud types and their radiative properties, and an estimate of the impact of such changes on the Earth's radiation

budget. For evaluating the transition of deep-convection to anvil cirrus clouds, a life cycle analysis is performed in a Lagrangian tracking framework for present day and perturbed climate with +2 K SST. The observations and the model Lagrangian trajectories are tracked for 5 days after the convective event, evaluating the growth and decay behavior of cirrus with respect to convective activity. The main findings are listed as follows,

- The decay of deep-convective clouds is rapid (within 1 day), which is followed by cirrostratus growth which finally thin-out to form cirrus clouds.
- The Lagrangian evolution and life cycle of cirrostratus and cirrus clouds show that the model diagnoses a stronger convection with relatively longer life time compared to the observations.
- Tropical cirrus clouds diagnosed in ECHAM5 are categorized into detraining cirrus which last for  $20\pm 15$  hours, and in situ cirrus (generated by other dynamical forces, such as small scale turbulent motions, gravity- and large scale-waves or large scale uplift) which last for  $17\pm 13$  hours.
- Similar to the present day climate, the cloud transitions of deep-convection detraining to cirrostratus and further becoming cirrus is found to be consistent in the perturbed climate.
- The cirrostratus and cirrus clouds increase in height as well as cloud amount in the warmer climate, especially on day 2 and 3 after the deep-convection.
- The convection is stronger in the perturbed climate compared to the present day climate implying larger values for precipitation on day 2 and 3, leading to a subsequent drying of the upper tropospheric relative humidity (200-500 hPa).
- The overall net forcing in the warmer climate increases (becoming less negative) due to stronger longwave cloud radiative effect (dependent on cloud height) than the shortwave effect (dependent on cloud optical thickness). This leads to a positive climate feedback in the perturbed climate from a Lagrangian perspective.

## 6.2 Synergy of results

The overall finding in this study which is consistent in all the evaluation approaches summarized above is the model weakness in simulating high and low clouds. The high-level clouds are overestimated in the tropics, which is compensated by an underestimation of low- and mid-level clouds. Tropical areas lead to a major contribution in this model deficiency on account of higher amount of convection over land. Individual events cause the biases in the cloud categories, but on a global scale these biases are balanced due to regions with opposite behavior. For example,

deep-convection in the tropics versus the marine shallow and stratocumulus clouds in extratropics.

As revealed in global histograms, the tropical regions in ECHAM5 show an over-estimation of thin cirrus and deep-convective clouds. Hence, the moisture is transported to higher levels in the atmosphere and is not allowed to detrain at low- and mid-levels in the ECHAM5 convection scheme. The ECHAM5 analysis does not show a prominent diurnal cycle for deep-convective and high-level clouds except for the Indian monsoon region. In our analysis, the diurnal cycle of cloud cover fraction is evaluated for model and observations and not convective precipitation (which is a more direct property of deep-convection).

The low-level clouds in ECHAM5 show a very weak diurnal cycle, which leads to a too weak diurnal cycle for the total clouds in the model. The inadequate representation of the boundary layer processes within the convection schemes of the GCMs is a likely reason for the larger variation in individual shallow convection regions compared to the observations.

The cluster analysis reveals that the cloud regimes for ECHAM5 model in extratropics show better diagnostics in comparison to the tropics, since the model is forced by large scale circulation and there are less individual (convective) events than the tropics. The widespread occurrence of thick, high cloud in the tropics results in a warm bias for the ECHAM5 model similar to the findings of Williams & Tselioudis (2007).

The Lagrangian transition of deep-convection to cirrus clouds in the model shows an important aspect of model in terms of life cycle of convective clouds. Similar studies are performed on observations (for e.g., Luo & Rossow (2004) among others) but the cloud transition studies over GCM have not been attempted before. Present analysis provides a new insight in the model evaluation stating how long the clouds stay in the system from a Lagrangian perspective and hence is useful in evaluating the radiative feedbacks of the clouds. The trajectory analyses over the present day and perturbed climate scenarios reveal that the reason for too many and too thick high clouds found in the other evaluation approaches is indeed due to too intense convective detrainment of moisture in the upper troposphere, and due to longer life-time of convective and anvil cirrus clouds.

### 6.3 Scope of future research

The model deficiencies which are evaluated in the current study pin-point the shortcomings of cloud parameterizations implemented in ECHAM5. Sensitivity studies for tunable parameters of the convection parameterization scheme is one of the possible extensions in evaluating the cloud representations in ECHAM5. As seen in the findings of the current study, the ECHAM5 convection is too strong compared to the observations. The sensitivity of entrainment parameter in the model should be considered for creating more clouds at low- and mid-levels. Since the climate change response analysis using cloud regime clusters as well as deep-convection transitions

show that the strength of convection increases in the warmer climate, it is important to evaluate the same with sensitivity studies of varying entrainment rate parameter.

With an established knowledge that marine shallow clouds provide the largest uncertainty in determining cloud feedbacks (Bony et al., 2006), improvement in boundary layer parameterizations for representing shallow cumulus and stratocumulus clouds in ECHAM5 are much needed in order to have confidence in the future climate projections. Improvement in convective parameterization and coupling it with statistical cloud cover schemes will provide a more realistic representation of convective clouds in the ECHAM5 model. Model cloud evaluation with new and advanced satellite data (for e.g., active sensors providing vertical profile of clouds) is recommended as follow on tasks.

Relating the cirrus evolution to the upper-tropospheric humidity (UTH) in a Lagrangian framework is an interesting extension of the cloud transition study. The interaction between cirrus and UTH over composite of clear and over cirrus overcast trajectories may help in the understanding the contribution of cirrus in moistening of upper troposphere. The cirrus influence over UTH could be a useful model evaluation study in order to increase confidence in correctly simulating upper troposphere water vapor feedback in the GCMs. Tracking the trajectory path in terms of cloud transport to sub-tropics i.e., to latitudes where the trajectories generally move and disperse will provide an idea of spatial scales of advection of convective detrainment.

The climate feedback analysis for detrainment and in situ cirrus may serve as a next step to the convection-cirrus life cycle analysis. Generated in entirely different processes (detrainment cirrus generated by convective detrainment and the in situ cirrus by large scale dynamic processes) both cirrus types have different climate feedbacks effects Luo & Rossow (2004).

---

# Bibliography

- ACKERMAN, T. P., LIOU, K. N., VALERO, F. P. J., AND PFISTER, L. (1988). Heating rates in tropical anvils. *Journal of Atmospheric Sciences* **45**, 1606 – 1623.
- ANDERBERG, M. R. (1973). Cluster analysis for applications. *Academic New York*, 359.
- ARAKAWA, A. (1975). Modelling clouds and cloud processes for use in climate models. The Physical Basis of Climate and Climate Modelling. *GARP Publications Series* **16**, ICSU/WMO, 181–197.
- BETTS, A. K. AND JAKOB, C. (2002). Evaluation of the diurnal cycle of precipitation, surface thermodynamics and surface fluxes in the ECMWF model using LBA data. *Journal of Geophysical Research* **107(D20)**, 8045, doi: [10.1029/2001JD000427](https://doi.org/10.1029/2001JD000427).
- BONY, S., COLMAN, R., KATSOV, V. M., ALLAN, R. P., BRETHERTON, C. S., DUFRESNE, J.-L., HALL, A., HALLEGATTE, S., HOLLAND, M. M., INGRAM, W., RANDALL, D. A., SODEN, B. J., TSELILOUDIS, G., AND WEBB, M. J. (2006). How Well Do We Understand and Evaluate Climate Change Feedback Processes? *Journal of Climate* **19**, 3445 – 3482.
- BONY, S., DUFRESNE, J.-L., TREUT, H. L., MORCRETTE, J.-J., AND SENIOR, C. (2004). On dynamic and thermodynamic components of cloud changes. *Climate Dynamics* **22(2/3)**, 71–76.
- BRETHERTON, C., BLOSSEY, P. N., AND PETERS, M. E. (2006). Comparison of simple and cloud-resolving models of moist convection-radiation interaction with a mock-Walker circulation. *Theoretical Computational Fluid Dynamics* doi:[10.1007/s00162-006-0029-7](https://doi.org/10.1007/s00162-006-0029-7).
- BRETHERTON, C. S. AND PINCUS, R. (1995). Cloudiness and marine boundary layer dynamics in the ASTEX Lagrangian experiments. Part I: Synoptic setting and vertical structure. *Journal of Atmospheric Sciences* **52**, 2707 – 2723.
- CESS, R. D., POTTER, G. L., BLANCHET, J. P., BOER, G. J., GENIO, A. D. D., DÉQUÉ, M., DYMNIKOV, V., GALIN, V., GATES, W. L., GHAN, S. J., KIEHL, J. T., LACIS, A. A., TREUT, H. L., LI, Z.-X., LIANG, X.-Z., MCAVANEY, B. J., MELESHKO, V. P., MITCHELL, J. F. B., MORCRETTE, J.-J., RANDALL,

- D. A., RIKUS, L., ROECKNER, E., ROYER, J. F., SCHLESE, U., SHEININ, D. A., SLINGO, A., SOKOLOV, A. P., TAYLOR, K. E., WASHINGTON, W. M., WETHERALD, R. T., YAGAI, I., AND ZHANG, M.-H. (1990). Intercomparison and interpretation of climate feedback processes in 19 atmospheric general circulation models. *Journal of Geophysical Research* **95**, No. D10, 16,601–16,615.
- CHAMBERS, L. H., LIN, B., AND YOUNG, D. F. (2002). Examination of new CERES data for evidence of tropical iris feedback. *Journal of Climate* **15**, 3719 – 3726.
- CHEN, S. S. AND HOUZE-JR., R. A. (1997). Diurnal variation and life-cycle of deep convective systems over the tropical Pasific warm pool. *Quarterly Journal of the Royal Meteorological Society* **123**, 357–388.
- COLMAN, R. (2003). A comparison of climate feedbacks in general circulation models. *Climate Dynamics* **20**, 865–873.
- DAI, A. (2006). Precipitation characteristics in eighteen coupled climate models. *Journal of Climate* **19**, 4605–4630.
- DAI, A., GIORGI, F., AND TRENBERTH, K. E. (1999). Observed and model simulated precipitation diurnal cycle over the contiguous United States. *Journal of Geophysical Research* **104**, 6377 – 6402.
- DAI, A. AND TRENBERTH, K. E. (2004). The diurnal cycle and its depiction in the Community Climate System Model. *Journal of Climate* **17**, 930 – 951.
- DEL GENIO, A. D. AND KOVARI, W. (2002). Climatic properties of tropical precipitating convection under varying environmental conditions. *Journal of Climate* **15**, 2597 – 2615.
- DESSLER, A. E. AND SHERWOOD, S. C. (2000). Simulation of tropical upper tropospheric humidity. *Journal of Geophysical Research* **106**, 20155 – 20163.
- DRAXLER, R. R. (1997). HYSPLIT4 (Hybrid single-particle Lagrangian integrated trajectory) model. Web address: <http://www.arl.noaa.gov/data/ready/hysplit4.html>. *NOAA Air Resources Laboratory, Silver Spring, MD*.
- FU, Q., BAKER, M., AND HARTMANN, D. L. (2002). Tropical cirrus and water vapour: An effective Earth infrared iris? *Atmospheric Chemistry and Physics* **2**, 31 – 37.
- GORDON, N. D., NORRIS, J. R., WEAVER, C. P., AND KLEIN, S. A. (2005). Cluster analysis of cloud regimes and characteristic dynamics of midlatitude synoptic systems in observations and a model. *Journal of Geophysical Research* **110**, D15S17, doi:10.1029/2004JD005027.

- GRAY, W. M. AND JACOBSON, R. W. (1977). Diurnal variation of deep cumulus convection. *Monthly Weather Review* **105**, 1171 – 1188.
- GUICHARD, F., PETCH, J. C., REDELSPERGER, J.-L., BECHTOLD, P., CHABOUREAU, J.-P., CHEINET, S., GRABOWSKI, W., GRENIER, H., JONES, C. G., KÖHLER, M., PIRIOU, J.-M., TAILLEUX, R., AND TOMASINI, M. (2004). Modelling the diurnal cycle of deep precipitating convection over land with cloud-resolving models and single column models. *Quarterly Journal of the Royal Meteorological Society* **130**, 3139 – 3172.
- HARTMANN, D. L. (2002). Tropical surprise (climate change causes). *Science* **295**, 811 – 812.
- HARTMANN, D. L. AND LARSON, K. (2002). An important constraint on tropical cloud-climate feedback. *Geophysical Research Letters* **29**, 1951–1954.
- HARTMANN, D. L. AND MICHELSEN, M. L. (1993). Large-scale effects on the regulation of tropical sea surface temperature. *Journal of Climate* **6**, 2049 – 2062.
- HARTMANN, D. L. AND MICHELSEN, M. L. (2002). No evidence for Iris. *Bulletin American Meteorological Society* **83**, 249–454.
- HARTMANN, D. L., MOY, L. A., AND FU, Q. (2001). Tropical convection and the energy balance at the top of the atmosphere. *Journal of Climate* **14**, 4495–4511.
- HENDON, H. H. AND WOODBERRY, K. (1993). The Diurnal Cycle of Tropical Convection . *Journal of Geophysical Research* **98**, No. **D9**, 16,623 – 16,637.
- HEYMSFIELD, A. J. (2003). Properties of tropical and midlatitude ice cloud particle ensembles: Part I: Median mass diameters and terminal velocities. *Journal of Atmospheric Sciences* **60**, 2573 – 2591.
- HORVÁTH, A. AND SODEN, B. J. (2008). Lagrangian diagnostics of tropical deep convection and its effect upon upper-tropospheric humidity. *Journal of Climate* **21**, DOI: [10.1175/2007JCLI1786.1](https://doi.org/10.1175/2007JCLI1786.1), 1013 – 1028.
- IPCC (2001). Climate Change 2001: The scientific basis. In: Houghton J. T., Ding Y., Griggs D. J., Noguer M., Van der Linden P. J. and Xiaosu D. (eds) Contribution of Working Group I to the third L. *Cambridge University Press, Cambridge, UK* .
- IPCC (2007). Climate change 2007: the physical science basis. In: Solomon S., Qin D., Manning M., Chen Z., Marquis M., Averyt K.B., Tignor M., Miller H.L. (eds) Contribution of Working Group I to the fourth assessment report of the intergovernmental panel on climate change. *Cambridge University Press, Cambridge, UK* .
- JAKOB, C. AND TSELIODIS, G. (2003). Objective identification of cloud regimes in the Tropical Western Pacific. *Geophysical Research Letters* **30(21)**.

- JENSEN, E. J., TOON, O. B., SELKIRK, H. B., SPINHIRNE, J. D., AND SCHOE-  
BERL, M. R. (1996). On the formation and persistence of subvisible cirrus clouds  
near the tropical tropopause. *Journal of Geophysical Research* **101**, 21361 – 21375.
- JIN, Y. (1998). Investigation of cirrus by satellite remote sensing. *Ph.D. dissertation,*  
*Columbia University* p. 104.
- KIEHL, J. T. (1994). On the observed near cancellation between longwave and  
shortwave cloud forcing in tropical regions. *Journal of Climate* **7**, 559–565.
- KLEIN, S. AND JACOB, C. (1999). Validation and sensitivities of frontal clouds  
simulated by the ECMWF model. *Monthly Weather Review* **127**, 2514–2531.
- KLEIN, S. AND WEBB, M. (2009). ISCCP simulator implementation instructions:  
Readme. <http://cfmip.metoffice.com/README>.
- KLEIN, S. A., PINCUS, R., AND XU, K.-M. (2002). Using cloud-resolving model  
simulations of deep convection to inform cloud parameterizations in large-scale  
models. *Abstract in Proceedings: Twelfth ARM Science Team Meeting, St. Pe-  
tersburg, Florida.* .
- LIAO, X. AND RIND, D. (1997). Local upper tropospheric/lower stratospheric clear-  
sky water vapor and tropospheric deep convection. *Journal of Geophysical Re-  
search* **102**, No. D16, 19543–19557.
- LIN, B. B. A. W., CHAMBERS, L. H., HU, Y., AND XU, K.-M. (2002). The Iris  
hypothesis: A negative or positive cloud feedback? *Journal of Climate* **15**, 3–7.
- LIN, X., RANDALL, D. A., AND FOWLER, L. D. (2000). Diurnal variability of the  
hydrologic cycle and radiative fluxes: Comparisons between observations and a  
GCM. *Journal of Climate* **13**, 4159 – 4179.
- LINDZEN, R. S., CHOU, M. D., AND HOU, A. Y. (2001). Does the Earth have an  
adaptative infrared Iris? *Bulletin American Meteorological Society* **82**, 417–432.
- LINDZEN, R. S., CHOU, M. D., AND HOU, A. Y. (2002). Comments on “no  
evidence for Iris.”. *Bulletin American Meteorological Society* **83**, 1345–1349.
- LIU, K.-N. (1986). Influence of cirrus clouds on weather and climate processes: a  
global perspective. *Monthly Weather Review* **115**, 1167 – 1199.
- LIU, C. AND MONCRIEFF, M. W. (1998). 1998 A numerical study of the diurnal  
cycle of tropical oceanic convection. *Journal of Atmospheric Sciences* **55**, 2329 –  
2344.
- LOHMANN, U. AND ROECKNER, E. (1996). Design and performance of a new  
cloud microphysics scheme developed for the ECHAM4 general circulation model.  
*Climate Dynamics* **12**, 557–572.

- LUO, Z. AND ROSSOW, W. B. (2004). Characterizing tropical cirrus life cycle, evolution, and interaction with upper-tropospheric water vapor using Lagrangian trajectory analysis of satellite observations. *Journal of Climate* **17**, 4541 – 4563.
- MACHADO, L. A. T. AND ROSSOW, W. B. (1993). Structural characteristics and radiative properties of tropical cloud clusters. *Monthly Weather Review* **121**, 3234–3260.
- MACHADO, L. A. T., ROSSOW, W. B., GUEDES, R. L., AND WALKER, A. W. (1998). Life cycle variations of mesoscale convective systems over Americas. *Monthly Weather Review* **125**, 1630–1654.
- MURPHY, J. M., SEXTON, D. M. H., BARNETT, D., JONES, G., WEBB, M. J., COLLINS, M., AND STAINFORTH, D. A. (2004). Quantification of modelling uncertainties in a large ensemble of climate change simulations. *Nature* **430**, 768 – 772.
- NAKAJIMA, T. AND KING, M. D. (1990). Determination of the optical thickness and effective particle radius of clouds from reflected solar radiation measurements. Part I: Theory. *Journal of Atmospheric Sciences* **47**, 1878 – 1893.
- NORDENG, T. E. (1994). Extended versions of the convective parameterization scheme at ECMWF and their impact on the mean and transient activity of the model in the tropics. *Tech. Memo., European Centre for Medium-Range Weather Forecasts, Reading, U. K.* **206**.
- PFEIFER, S. (2006). *Modeling cold cloud processes with the regional climate model REMO*. vol. Max-Planck Institute for Meteorology, Hamburg.
- PIERREHUMBERT, R. T. (1998). Lateral mixing as a source of subtropical water vapor. *Geophysical Research Letters* **25**, 151 – 154.
- PINCUS, R., BAKER, M. B., AND BRETHERTON, C. S. (1997). What controls stratocumulus radiative properties? Lagrangian observations of cloud evolution. *Journal of Atmospheric Sciences* **54**, 2215 – 2236.
- RÄISÄNEN, P., BARKER, H. W., KHAIROUTDINOV, M. F., AND RANDALL, D. A. (2004). Stochastic generation of subgrid-scale cloudy columns for large-scale models. *Quarterly Journal of the Royal Meteorological Society* **130**, 2047–2067.
- RAMANATHAN, V., CESS, R. D., HARRISON, E. F., MINNIS, P., BARKSTROM, B. R., AND HARTMANN, D. L. (1989). Cloud-radiative forcing and climate: Results from the Earth Radiation Budget Experiment. *Science* **243**, 57–63.
- RANDALL, D. A., HARSHVARDHAN, AND DAZLICH, D. A. (1991). Diurnal variability of the hydrologic cycle in a general circulation model. *Journal of Atmospheric Sciences* **48**, 40 – 62.

- RANDALL, D. A., WOOD, R. A., BONY, S., COLMAN, R., FICHEFET, T., FYFE, J., KATTSOV, V., PITMAN, A., SHUKLA, J., SRINIVASAN, J., STOUFFER, R. J., SUMI, A., AND TAYLOR, K. E. (2007). Climate Models and Their Evaluation, Edited by: S. Solomon, D. Qin, M. Manning, Z. Chen, M. Marquis, K. B. Averyt, M. Tignor and H. L. Miller. Climate Change 2007: The Physical Science Basis, Contribution of Working Group I to the Fourth Assessment Report of the IPCC. *Cambridge University Press, Cambridge, UK and New York, NY, USA* .
- ROECKNER, E., BAUML, G., BONAVENTURA, L., BROKOPF, R., ESCH, M., GIORGETTA, M., HAGEMANN, S., KIRCHNER, I., KORNBLUEH, L., MANZINI, E., RHODIN, A., SCHLESE, U., SCHULZWEIDA, U., AND TOMPKINS, A. (2003). The atmospheric general circulation model ECHAM5: Part I: Model description. *MPI Report, Max Planck Institute for Meteorology, Hamburg* **349**.
- ROECKNER, E., SCHLESE, U., BIERCAMP, J., AND LOEWE, P. (1987). Cloud optical depth feedbacks and climate modeling. *Nature* **329**, 138–140.
- ROGERS, R. R. (1979). A Short Course in Cloud Physics. *Pergamon Press* .
- ROSSOW, W. B. AND GARDER, L. (1993). Cloud detection using satellite measurements of infrared and visible radiances for ISCCP. *Journal of Climate* **6**, 2391 – 2369.
- ROSSOW, W. B. AND SCHIFFER, R. A. (1991). ISCCP cloud data products. *Bulletin of American Meteorological Society* **79**, 2457–2476.
- ROSSOW, W. B. AND SCHIFFER, R. A. (1999). Advances in understanding clouds from ISCCP. *Bulletin American Meteorological Society* **80**, 2261–2288.
- ROSSOW, W. B., TSELILOUDIS, G., POLAK, A., AND JAKOB, C. (2005). Tropical climate described as a distribution of weather states indicated by distinct mesoscale cloud property mixtures. *Geophysical Research Letters* **32(21)**.
- ROSSOW, W. B., WALKER, A. W., BEUSCHEL, D. E., AND ROITER, M. D. (1996). International Satellite Cloud Climatology Project (ISCCP): Documentation of new cloud datasets. *World Meteorological Organization, Geneva* .
- SALATHE, E. P. AND HARTMANN, D. L. (1997). A trajectory analysis of tropical upper-tropospheric moisture and convection. *Journal of Climate* **10**, 2533 – 2547.
- SALATHE, E. P. AND HARTMANN, D. L. (2000). Subsidence and upper-tropospheric drying along trajectories in a general circulation model. *Journal of Climate* **13**, 257 – 263.
- SATO, T., MIRUA, H., SATOH, M., TAKAYABU, Y. N., AND WANG, Y. (2009). Diurnal Cycle of Precipitation in the Tropics Simulated in a Global Cloud-Resolving Model. *Journal of Climate* **22**, DOI: [10.1175/2009JCLI2890.1](https://doi.org/10.1175/2009JCLI2890.1), 4809 – 4826.

- SCHIFFER, R. A. AND ROSSOW, W. B. (1983). The International Satellite Cloud Climatology Project (ISCCP): The first project of the world climate research programme. *Bulletin of American Meteorological Society* **64**.
- SCHNEIDER, S. (1972). Cloudiness as a global climatic feedback mechanism: The effects on radiation balance and surface temperatures of variations in cloudiness. *Journal of Atmospheric Sciences* **29**, 1413–1422.
- SENIOR, C. A. AND MITCHELL, J. F. B. (1993). Carbon dioxide and climate: The impact of cloud parameterization. *Journal of Climate* **6**, 393–418.
- SHERWOOD, S. C. (1996). Maintenance of the free-tropospheric tropical water vapor distribution. Part I: Clear regime budget. *Journal of Climate* **9**, 2903 – 2918.
- SLINGO, A., WILDERSPIN, R. C., AND BRETNALL, S. J. (1987). Simulations of the diurnal cycle of outgoing longwave radiation with an atmospheric GCM. *Monthly Weather Review* **115**, 1451–1457.
- STEPHENS, G. L. (2005). Cloud Feedbacks in the Climate System: A Critical Review. *Journal of Climate* **18**, 237 – 273.
- STEPHENS, G. L., TSAY, S., STACKHOUSE-JR., P. W., AND FLATAU, P. J. (1990). The relevance of the microphysical and radiative properties of cirrus clouds to climate and climate feedback. *Journal of Atmospheric Sciences* **47**, 1742 – 1753.
- SUNDQVIST, H. (1978). A parameterization scheme for non-convective condensation including prediction of cloud water content. *Quarterly Journal of the Royal Meteorological Society* **104**, 677–690.
- TIAN, B., SODEN, B. J., AND WU, X. (2004). Diurnal cycle of convection, clouds, and water vapor in the tropical upper troposphere: Satellites verses a general circulation model. *Journal of Geophysical Research* **109**, D10101, doi:10.1029/2003JD004117.
- TIEDTKE, M. (1989). A comprehensive mass-flux scheme for cumulus parameterization in large-scale models. *Monthly Weather Review* **117**, 1779–1800.
- TOMPKINS, A. (2002). A prognostic parameterization for the subgrid-scale variability of water vapor and clouds in large-scale models and its use to diagnose cloud cover. *Journal of Atmospheric Sciences* **59**, 1917–1942.
- TOMPKINS, A. M. AND CRAIG, G. C. (1999). Sensitivity of tropical convection to sea surface temperature in the absence of large-scale flow. *Journal of Climate* **12**, 462 – 476.
- TRENBERTH, K. E., FASULLO, J. T., AND KIEHL, J. (2009). Earths global energy budget. *Bulletin of American Meteorological Society* **90**, 311–323.

- WANG, Y., ZHOU, L., AND HAMILTON, K. (2007). Effect of convective entrainment/detrainment on simulation of tropical precipitation diurnal cycle. *Monthly Weather Review* **135**, 567–585.
- WEBB, M. J., SENIOR, C., BONY, S., AND MORCRETTE, J.-J. (2001). Combining ERBE and ISCCP data to assess clouds in the Hadley Centre, ECMWF and LMD atmospheric climate models. *Climate Dynamics* **17**, 905–922.
- WILLIAMS, K. D. AND TSELILOUDIS, G. (2007). GCM intercomparison of global cloud regimes: present-day evaluation and and climate change response. *Climate Dynamics* **29**, 231–250.
- WILLIAMS, K. D. AND WEBB, M. (2009). A quantitative performance assessment of cloud regimes in climate models. *Climate Dynamics* **33**, 141–157.
- YANG, G. Y. AND SLINGO, J. M. (2001). The diurnal cycle in the tropics. *Monthly Weather Review* **129**, 784–801.
- YAO, M.-S. AND GENIO, A. D. D. (1999). Effects of cloud parameterization on the simulation of climate changes in the GISS GCM. *Journal of Climate* **12**, 761 – 779.

Die gesamten Veröffentlichungen in der Publikationsreihe des MPI-M  
„Berichte zur Erdsystemforschung“,  
„Reports on Earth System Science“,  
ISSN 1614-1199

sind über die Internetseiten des Max-Planck-Instituts für Meteorologie erhältlich:

<http://www.mpimet.mpg.de/wissenschaft/publikationen.html>

